

EUSKAL HERRIKO UNIBERSITEA - UNIVERSIDAD DEL PAÍS VASCO

MATERIALEN FISIKA SAILA - DEPARTAMENTO DE FÍSICA DE  
MATERIALES



Universidad del País Vasco      Euskal Herriko Unibertsitatea

**Infrared spectroscopic near-field microscopy  
of nanoparticles and semiconductor  
nanowires**

Johannes Michael Stiegler

- PhD Thesis -

Thesis supervisor

Rainer Hillenbrand

**2012**



*L'essentiel est invisible pour les yeux*

---

(Antoine de Saint-Exupéry: Le Petit Prince)



# Contents

<b>Summary</b>	<b>1</b>
<b>Resumen</b>	<b>3</b>
<b>1 Introduction</b>	<b>9</b>
<b>2 Scattering-type Scanning Near-field Optical Microscopy (s-SNOM)</b>	<b>13</b>
2.1 Introduction to High Resolution Imaging Methods . . . . .	14
2.2 Experimental s-SNOM Setup . . . . .	18
Atomic Force Microscope (AFM) . . . . .	19
Optical Setup and Tip Illumination . . . . .	20
Interferometric Signal Detection and Background Suppression . . . . .	21
Spectroscopic Near-field Imaging . . . . .	24
2.3 Theory of s-SNOM . . . . .	24
Dipole Model . . . . .	25
Finite Dipole Model . . . . .	27
Extended Finite-Dipole Model . . . . .	28
<b>3 Nanoscale Resolved Free-carrier Profiling in Individual InP Nanowires</b>	<b>31</b>
3.1 Introduction . . . . .	32
3.2 Theoretical Near-field Contrast of Highly Doped Semiconductors . . . . .	32
3.3 Sample Fabrication . . . . .	36
3.4 Near-field Study of InP Nanowires . . . . .	41
3.5 Quantification of the Free-carrier Concentration by IR Near-field Spectroscopy . . . . .	43
3.6 Outlook . . . . .	46
3.7 Conclusion . . . . .	47
<b>4 Correlative Infrared-electron Nanoscopy Applied to Zinc Oxide Nanowires</b>	<b>49</b>
4.1 Introduction . . . . .	50

---

4.2	Sample Fabrication . . . . .	51
4.3	s-SNOM Study of Mechanically Polished ZnO Nanowire Arrays . . . . .	54
4.4	Correlative Infrared-electron Nanoscopy of Single Nanowires . . . . .	57
4.5	Discussion . . . . .	62
	Discussion of the Infrared-electron Nanoscopy Results . . . . .	62
	Discussion of the Possible Influence of Polishing on the IR Near-field Contrast . . . . .	64
	Discussion of Polishing Residues on the IR Near-field Contrast . . . . .	65
4.6	Conclusion . . . . .	66
<b>5</b>	<b>Infrared Absorption Spectroscopy of Individual SiN Nanoparticles</b>	<b>67</b>
5.1	Introduction . . . . .	68
5.2	Size Dependence of the IR Near-field Contrast of Si <sub>3</sub> N <sub>4</sub> Nanoislands . . . . .	69
5.3	Relation between Near-field Phase and Far-field Absorption . . . . .	73
5.4	Spectral Near-field Amplitude and Phase Contrast for Small Particles . . . . .	75
5.5	Conclusions . . . . .	78
	<b>List of Publications</b>	<b>79</b>
	<b>Acknowledgments</b>	<b>81</b>
	<b>Bibliography</b>	<b>83</b>





# Summary

Scattering-type scanning near-field optical microscopy (s-SNOM) is an emerging optical imaging technique, which has shown great potential to study the chemical composition, the dielectric properties and the structure of materials with a nanometer resolution. In this thesis, s-SNOM is applied to study the free-carrier concentration in semiconductor nanowires, and it is demonstrated that s-SNOM allows for the chemical identification of particles smaller than 10 nm.

s-SNOM is typically based on atomic force microscopy (AFM), where the tip is illuminated with a focused laser-beam. The tip-scattered light is recorded interferometrically, simultaneously to topography, yielding nanoscale resolved optical amplitude and phase images. Using metallic tips, the strong optical near-field interaction between tip and sample modifies the scattered light, depending on the local dielectric properties of the sample. Particularly, infrared (IR) near-field imaging can be thus used to generate maps of chemical composition or free-carrier concentration with nanoscale resolution.

In this thesis IR s-SNOM is applied for the first time to map the free-carrier concentration  $n$  in different semiconductor nanowires, such as InP and ZnO. By recording optical amplitude and phase images of the sample at different IR frequencies, we obtained local IR near-field spectra. Fitting the experimental spectra with model calculations, we determined  $n$  quantitatively and with a spatial resolution of about 20 nm. Furthermore, we successfully applied s-SNOM to directly map the radial free-carrier profile in ZnO nanowire cross-sections.

To obtain a deeper and more comprehensive understanding of the material properties on the nanometer-scale, we introduce correlative infrared-electron nanoscopy as a novel imaging method. Yielding s-SNOM and transmission electron microscopy (TEM) images of *one and the same* nanostructure, this method allows to correlate maps of chemical composition and conductivity obtained by s-SNOM with atomically re-

solved TEM images that provide structural information of the sample. To demonstrate the intriguing capabilities of this method, it is applied to study ZnO nanowire cross-sections, where an inverse correlation between the radial free-carrier profile and the crystal defect density is found. In the future, we envision correlative infrared-electron nanoscopy to provide interesting and novel insights into other important materials such as graphene, topological insulators, phase change materials, or biological and organic nanostructures.

Investigating a silicon nitride ( $\text{Si}_3\text{N}_4$ ) nanoparticle sample, the sensitivity of s-SNOM was studied. It can be shown that IR s-SNOM allows for the chemical identification of particles as small as 5 nm, by mapping the characteristic Si-N stretching mode. The results furthermore show theoretically that the measured near-field phase spectra correlate well with the far-field absorption spectra of  $\text{Si}_3\text{N}_4$  nanoparticles. This can be understood by the fact that the dielectric value of a sample is a complex quantity, where the imaginary part describes the material specific absorption properties, giving rise to a phase shift between the light illuminating the sample and the backscattered light, which is detected in interferometric s-SNOM. These results are essential for the understanding of the spectral near-field contrast of small particles and open the door to nanoscale chemical mapping based on the IR near-field spectroscopy.

# Resumen

La nanotecnología es un campo emergente y relativamente nuevo de la investigación, que ha ganado un gran interés en los últimos años. El término nano es un prefijo derivado de la palabra griega  $\nu\alpha\lambda\omicron\varsigma$  (nános) y significa "diminuto, enano". La nanotecnología y las nanociencias relativas a ésta destacan por su carácter multidisciplinario y representan el enfoque combinado de diferentes materias como la biología, la química, la física y la ciencia de materiales, para diseñar y manipular estructuras, materiales y sus propiedades a escala nanométrica (hablamos de dimensiones menores a 100 nm). El origen de la nanotecnología se le atribuye a Richard Feynman, que pronosticó la exploración y la manipulación del nanomundo en 1959 en su famoso discurso "There's Plenty of Room at the Bottom" (Hay mucho sitio al fondo). El término nanotecnología, sin embargo, fue utilizado por primera vez en 1974 por Taniguchi, y popularizado por Drexler en 1986 con su libro "Engines of Creation: The Coming Era of Nanotechnology" (La próxima era de la nanotecnología). Hoy en día, medio siglo más tarde, la nanotecnología ya se ha convertido en parte de nuestra vida cotidiana. Su aplicación varía desde la industria de semiconductores hasta la medicina y farmacia.

La industria de semiconductores es probablemente uno de los mejores ejemplos de cómo la nanotecnología se aplica en la industria a gran escala. Los dispositivos modernos tales como ordenadores portátiles, teléfonos inteligentes, y muchos más no serían posibles sin los beneficios de la nanotecnología. Por ejemplo, el actual estado del arte de los dispositivos CMOS ("complementary metal oxide semiconductor") se basan en el denominado "nodo de tecnología 22 nanómetros", lo que significa que la distancia media entre dos transistores es de 22 nm. De acuerdo con la Ley de Moore, el número de transistores por pulgada cuadrada se duplica cada dos años. Esta tendencia tiene dos implicaciones: (i) En primer lugar, los dispositivos se vuelven más y más pequeños, y (ii) desde el punto de vista técnico, éstos se hacen más y más difíciles de fabricar y mejorar.

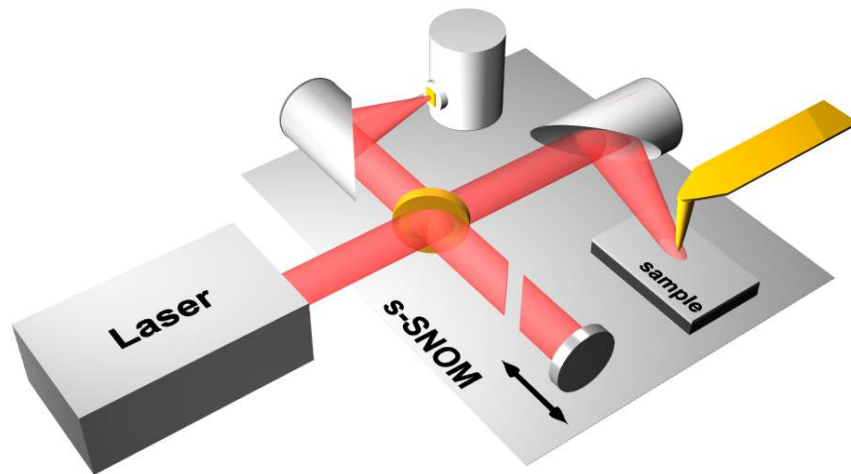
Con el fin de mantener al día esta tendencia de la miniaturización, se requieren nuevos

caminos para fabricar dispositivos. Aquí, los nanohilos semiconductores han mostrado un gran potencial como posibles componentes básicos para un dispositivo nano(opto)electrónico en una futura "post CMOS". A diferencia de las tecnologías de litografía actuales, que siguen una estrategia de fabricación "Top-down", los nanohilos semiconductores permiten la estrategia de fabricación "Bottom-up", donde las propiedades del dispositivo se pueden modificar y controlar durante el crecimiento con una precisión a escala nanométrica. Esta estrategia es similar a la de la naturaleza en la vida, donde las entidades más complejas, como los organismos vivos, así como otras estructuras grandes (como los árboles) empiezan a pequeña escala con unas pocas moléculas nanométricas como componentes básicos primarios.

En una exitosa aplicación de la nanotecnología en general, y de estos nanohilos en particular, será crítico sin embargo el control y la verificación experimental de las propiedades de los materiales locales, que aún hoy es una tarea muy difícil. Una cierta variedad de métodos ha mostrado un gran potencial para la caracterización de muestras con resolución local nanométrica. La técnica de Microscopía de Sonda Atómica por Láser Pulsado (APM en sus siglas inglesas), por ejemplo visualiza la distribución espacial de los átomos, lo que permite a su vez determinar la distribución espacial de los agentes de dopado de impurezas. Sin embargo, la APM es un método destructivo y mide la impureza más que la concentración de portadores libres activos. La Microscopía de Sonda de Barrido (SPM) es otra técnica de imagen que permite la caracterización de materiales en la nanoescala. Proporciona información sobre la topografía de una muestra, y en el caso de otras subtécnicas derivadas de ésta como la Microscopía de Sonda Kelvin (KPM), la Microscopía por Escaneo de Resistencia (SSRM) o la Microscopía por Escaneo de Capacidad (SCM) se obtiene información adicional cualitativa sobre la concentración de portadores libres. Estas técnicas, sin embargo, requieren el contacto eléctrico de la muestra, y ofrecen una sensibilidad pobre.

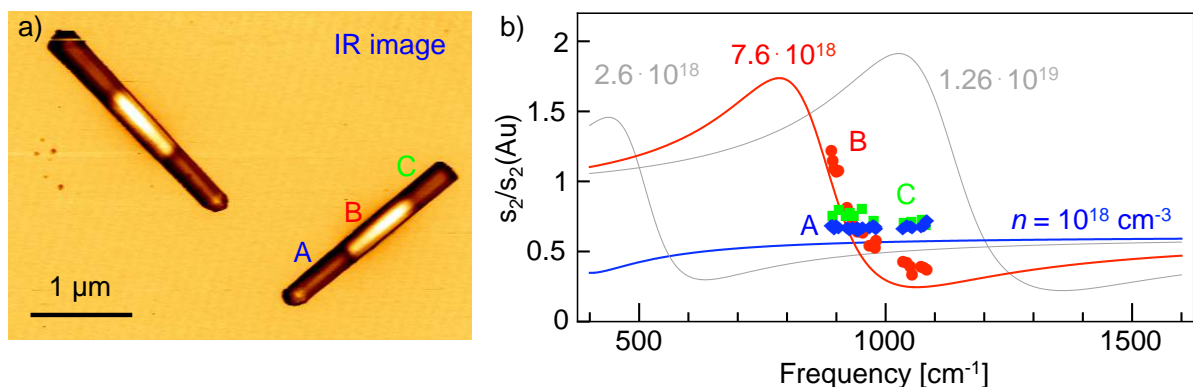
Otra técnica basada en SPM es la microscopía óptica de campo cercano de barrido de tipo dispersivo (s-SNOM), una nueva técnica de microscopía óptica que en los últimos años ha mostrado un gran potencial para correlacionar la composición química local con la conductividad. La técnica s-SNOM se basa típicamente en un Microscopio de Fuerza Atómica (AFM), donde se ilumina la punta metálica afilada por un rayo láser muy enfocado. La punta funciona como una antena que convierte la radiación de la iluminación en un campo electromagnético fuertemente confinado y de gran intensidad en el ápice de la punta. Debido a la interacción de este campo cercano entre la punta y la muestra, la luz elásticamente dispersada desde la punta se modifica, tanto en amplitud como en fase, dependiendo de las propiedades dieléctricas locales de la

muestra. La detección interferométrica de la luz dispersada produce por lo tanto imágenes nanométricas resueltas en amplitud y fase, revelando los valores complejos de las propiedades dieléctricas locales de la muestra. En esta tesis, se aplica por la primera vez la técnica infrarroja (IR) s-SNOM para mapear los portadores libres en nanohilos semiconductores, la cual ofrece varias ventajas sobre otras técnicas utilizadas para el estudio de portadores libres a escala nanométrica: s-SNOM permite mediciones cuantitativas, es no invasivo y no requiere contacto eléctrico ninguno con la muestra.



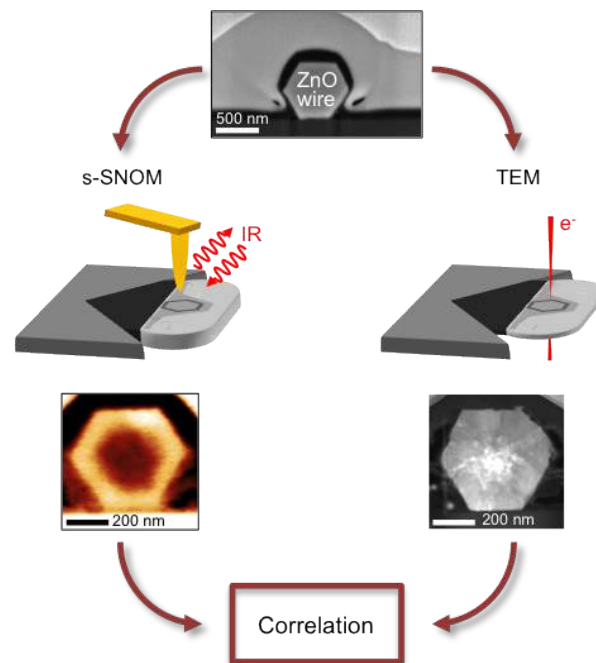
Presentación esquemática del experimental s-SNOM configuración.

En el capítulo 2 se presentará el s-SNOM junto con la base teórica para entender los contrastes de campo cercano. Después de una descripción de la configuración experimental utilizada en esta tesis, se analizará la detección de la señal y la inevitable supresión de las señales de fondo.



**IR s-SNOM imagen de modulación de dopado nanohilos InP.** (a) Imagen de amplitud registrada a una frecuencia de láser de  $893 \text{ cm}^{-1}$ . (b) Experimental (símbolos) y calculada (líneas continuas) IR de campo cercano mostrando espectros de amplitud en las posiciones de A-C.

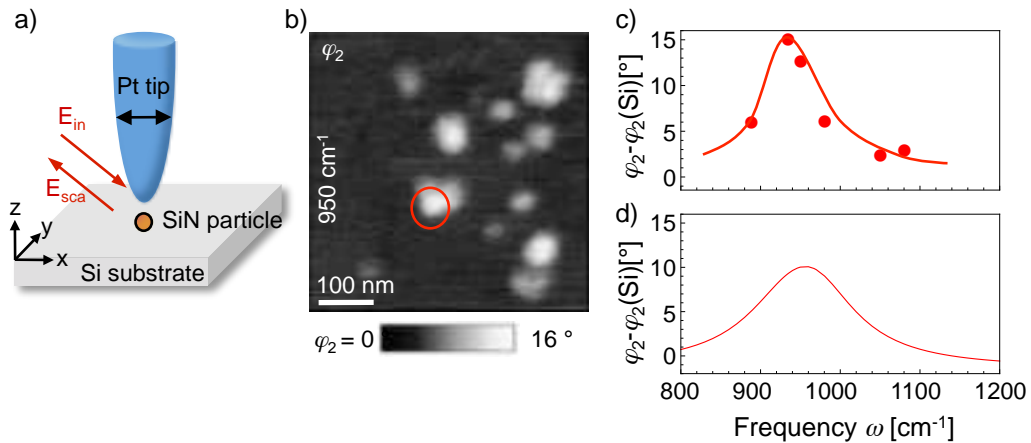
Los primeros resultados experimentales se mostrarán en el capítulo 3, donde se aplicará la técnica s-SNOM con luz infrarroja (IR s-SNOM) para mapear la concentración y la movilidad de portadoras libres en nanohilos semiconductores de dopado modulado. Para ello, se eligieron nanohilos InP con dos segmentos sin dopar y un segmento altamente dopado como muestra. Aquí, se aprovecha el hecho de que los campos cercanos altamente concentrados en el ápice de la punta pueden inducir una resonancia de plasmón local en la muestra por debajo de la punta. Como la resonancia de plasmón depende fuertemente de la concentración y la movilidad de los portadores libres, un estudio espectroscópico por s-SNOM permite la cuantificación de la concentración de portadoras libres y su movilidad en el segmento de nanohilos altamente dopado. Así, se demostrará la alta sensibilidad del s-SNOM a los portadores libres en los nanohilos mediante la visualización incluso de pequeñas variaciones en la concentración de portadoras libres dentro del segmento altamente dopado.



**Esquema de la Nanoscopia Infrarroja-Electrónica.**

Después de haber demostrado que s-SNOM puede visualizar la concentración de portadores libres en los nanohilos semiconductores, en el capítulo 4 estudiaremos la relación entre las propiedades dieléctricas locales y la estructura, con el fin de obtener una comprensión más profunda y más amplia de las propiedades locales de los materiales. Para ello, se introducirá la nanoscopia infrarroja-electrónica, un método de formación de imágenes novedoso que combina el s-SNOM y la Microscopia Electrónica de Transmisión (TEM), y que permite estudiar la misma nanoestructura con ambas técnicas. Mientras que la TEM es una técnica de imagen bien establecida en la ciencia

de materiales, que proporciona información estructural con resolución atómica, el s-SNOM proporciona mapas de la conductividad con una resolución espacial de menos de 20 nm. Como ejemplo de aplicación, con una alta relevancia tecnológica, nanoscopía infrarroja-electronica se puede usar para estudiar la relación entre los defectos cristalinos y de la conductividad local en secciones transversales de nanohilos de ZnO, las cuales son un candidato prometedor para dispositivos de bajo coste de células solares.



**Espectroscopia IR por s-SNOM de una nanopartícula de  $\text{Si}_3\text{N}_4$  de tamaño inferior a 10 nm.** a) Montaje experimental. b) Imagen experimental IR que muestra la fase  $\varphi_2$  tomada a  $950 \text{ cm}^{-1}$ . c) Espectro medido y d) calculado de la fase  $\varphi_2$  del campo cercano de la partícula rodeada con un círculo en b). La línea sólida en c) sirve de guía.

Finalmente, en el capítulo 5 se presenta un estudio sistemático de cómo los contrastes de campo cercano en amplitud y fase dependerá del tamaño de las partículas pequeñas. Para este estudio, se eligieron nanoislas de  $\text{Si}_3\text{N}_4$  con alturas por debajo de 10 nm, depositadas sobre un sustrato de Si como modelo experimental. Hemos tenido éxito en la espectroscopía de campo cercano para obtener imágenes de la resonancia vibratoria de la extensión del enlace Si-N en partículas tan pequeñas como 5 nm. Hemos podido demostrar que los espectros de fase de campo cercano de las nanoislas de  $\text{Si}_3\text{N}_4$  escalan con sus espectros de absorción de campo lejano, lo que demuestra claramente la capacidad de IR s-SNOM para la identificación química de nanopartículas tan pequeñas como 5 nm. Además, nuestros estudios revelan que la amplitud y fase de campo cercano escala linealmente con el diámetro de las partículas, más que con el volumen, lo que podría explicarse por la interacción de campo cercano entre la punta y el sustrato.



# 1

## Introduction

Nanotechnology is a relatively new and emerging field of research that has gained a great interest in recent years. The word nano is a prefix derived from the greek word νάνος (nános) and means "dwarf". Nanotechnology and the related nanosciences are characterised by a high degree of multidisciplinary and represent the combined approach of different sciences such as biology, chemistry, physics, and materials science, to design and manipulate structures, materials, and their properties on the nanometer scale (at least one dimension sized below 100 nm). The origin of nanotechnology is attributed to Richard Feynman, who has foreseen exploration and manipulation of the nanoworld in 1959 in his now famous speech "There's Plenty of Room at the Bottom" [1]. The term nanotechnology, however, was used for the first time in 1974 by Taniguchi [2] and popularised by Drexler in 1986 with his book "Engines of Creation: The Coming Era of nanotechnology" [3]. Today, half a decade later, nanotechnology already has become part of our everyday life. Its application ranges from semiconductor industry to medicine and pharmacy.

The semiconductor industry is probably one of the best known industrial sectors where nanotechnology is applied on a large industrial scale. Modern devices such as laptops, smartphones and many more would not be possible without the benefits of nanotechnology. Current state-of-the-art CMOS (complementary metal oxide semiconductor)

devices are based on the so-called "22 nanometer technology node", which means that the half distance between two features accounts for 22 nm. According to Moore's Law, the number of transistors per square inch is doubling every two years. This trend has two implications: (i) First, devices become smaller, and (ii) from the technical standpoint, it becomes more and more challenging to manufacture and improve the devices.

In order to keep up with this trend of miniaturisation, new pathways to fabricate devices are required. Here, semiconductor nanowires have shown great potential as possible building blocks for future nano(opto-)electronic devices [4, 5, 6, 7, 8, 9] in a post CMOS era. In contrast to the current lithography technologies, which can be seen as a *top-down* approach, semiconductor nanowires allow for a *bottom-up* approach, where the device properties can be modified and controlled during growth with a precision on the nanometer scale. This approach is similar to nature's approach in life, where the most complex entities, such as living organisms (as well as huge structures such as trees) start on a small scale with single nano-scaled molecules as primary building blocks.

The successful application of nanotechnology in general and nanowires in particular, however, will critically rely on the control and experimental verification of the local material properties, which is still a challenging task. A variety of methods have shown great potential for a local sample characterisation with nanoscale resolution. Laser-pulsed Atom Probe Microscopy (APM) [10], for example, visualises the spatial distribution of atoms, which allows for the determination of the spatial distribution of impurity dopants. However, APM is a destructive method and measures the impurity rather than the active free-carrier concentration. Scanning Probe Microscopy (SPM) [11] is another imaging technique allowing for nanoscale material characterisation. It provides information about the topography of a sample, and in the case of Kelvin Probe Microscopy (KPM) [12], Scanning Spreading Resistance Microscopy (SSRM) [13] or Scanning Capacitance Microscopy (SCM) [14, 15] additional, qualitative information about the free-carrier concentration. These techniques, however, require electrical contacting of the sample, and offer a poor material sensitivity.

Another SPM technique is Scattering-type Scanning Near-field Optical Microscopy (s-SNOM) [16, 17, 18, 19], an emerging optical microscopy technique, which in recent years has shown great potential to map the local chemical composition [20, 21, 22, 23, 24] and conductivity [25, 26, 27, 28, 29, 30, 31]. s-SNOM is typically based on an Atomic Force Microscope (AFM), where the sharp metallic tip is illuminated by a focused laser beam. The tip functions as an antenna converting the illuminating radiation into a

---

highly localised and enhanced near-field at the tip apex [31, 32, 33]. Due to a near-field interaction between tip and sample, the light elastically scattered from the tip is modified in both, its amplitude and its phase, depending on the local dielectric properties of the sample [19]. Interferometric detection of the backscattered light thus yields nanoscale-resolved amplitude and phase images, revealing the local, complex-valued, dielectric sample properties. In this thesis, infrared (IR) s-SNOM is for the first time applied to map free-carriers in semiconductor nanowires. s-SNOM offers in this regard several advantages over other techniques used to study free-carriers on the nanometer scale: s-SNOM allows for quantitative measurements, it is non-invasive and requires no contacting of the sample.

In chapter 2 s-SNOM will be introduced and the theoretical background to understand the near-field contrasts will be provided. After a description of the experimental setup used in this thesis, the signal detection and the suppression of unavoidable background signals will be discussed.

The first experimental results are shown in chapter 3, where we demonstrate the application of IR s-SNOM to map the free-carrier concentration and mobility in modulation doped semiconductor nanowires. As a sample system indium phosphide (InP) nanowires comprising two undoped and one highly doped segment were chosen. We hereby exploit the fact that highly concentrated near-fields at the tip apex can induce a local plasmon resonance in the sample below the tip. As the plasmon resonance strongly depends on the concentration and the mobility of the active free-carriers, a spectroscopic s-SNOM study allows for the quantification of the free-carrier concentration and their mobility in the highly doped nanowire segment. We demonstrate the high sensitivity of s-SNOM to free-carriers in the nanowires by visualising even small variations of the free-carrier concentration within the highly doped segment.

After having demonstrated that s-SNOM can visualise the free-carrier concentration in semiconductor nanowires, in chapter 4 we study the relation between the local dielectric properties and the structure in order to obtain a deeper and more comprehensive understanding of the local material properties. We therefore introduce infrared-electron nanoscopy, a novel imaging method combining s-SNOM and Transmission Electron Microscopy (TEM), allowing for the study of *one and the same* nanostructure with both techniques. While TEM is a well established imaging technique in materials science providing structural information with atomic resolution, s-SNOM yields maps of the conductivity with a spatial resolution of less than 20 nm. As an application example with a high technological relevancy we apply infrared-electron nanoscopy to

study the relationship between crystal defects and local conductivity in cross-sections of zinc oxide (ZnO) nanowires, which serve as a promising candidate for low cost solar cell devices.

Finally, in chapter 5 we present a systematic study of how the near-field amplitude and phase contrasts depend on the size of small particles. For this study silicon nitride ( $\text{Si}_3\text{N}_4$ ) nanoislands with heights below 10 nm, deposited onto a Si wafer, have been chosen as an experimental model system. We succeeded in the spectroscopic near-field imaging of the vibrational resonance of the Si-N stretching bond in particles as small as 5 nm. We could show that the near-field phase spectra of the  $\text{Si}_3\text{N}_4$  nanoislands scale like their far-field absorption spectra, clearly demonstrating the capability of IR *s*-SNOM for the chemical identification of nanoparticles as small as 5 nm. Furthermore, our studies reveal that the near-field amplitude and phase scale linearly with the diameter of the particles rather than with the volume, which could be explained by the near-field interaction between tip and substrate.

# 2

## **Scattering-type Scanning Near-field Optical Microscopy (s-SNOM)**

*In this chapter a short introduction to scattering-type Scanning Near-field Optical Microscopy (s-SNOM) will be provided. After giving a motivation for high-resolution imaging, various methods allowing for nanoscaled imaging are briefly discussed to put s-SNOM into context. The experimental s-SNOM setup, as used in this thesis, will be outlined as well as analytical models to describe and understand the measured near-field contrasts will be introduced.*

## 2.1 Introduction to High Resolution Imaging Methods

Optical characterisation methods play an important role in many different sciences ranging from biology, physics to material sciences. With an ever shrinking structure and sample size, higher magnifications are needed to resolve the features. However, the resolution in classical optical microscopy is limited by diffraction to a resolution of about half the wavelength of the incident light  $\lambda/2 \approx 300$  nm (see Fig. 2.1a [34, 35]). To study samples smaller than this classical resolution limit various methods have been developed to either break or circumvent the diffraction limit in classical optical microscopy. In the following, an overview over widespread techniques that allow for a nanometer resolution in different fields of research is given.

To study biological samples fluorescence microscopy has become an important tool [36, 37, 38] due to the wide availability of biocompatible fluorophores. Using 4Pi microscopy [39] the resolution of fluorescence microscopy in z-direction has been improved to  $\sim 100$  nm. In the xy-plane STimulated Emission Depletion (STED) microscopy has enabled a possible spatial resolution of 25 nm. Thus, both methods practically break the classic diffraction limit. The combination of the availability of a broad range of fluorescent labels with the high resolution has enabled the study of the internal structure of cells [40] and even dynamic processes on a cellular level [41]. The versatility of fluorescent labels and the importance for biology gave rise to many more methods such as: Photo-Activated Localization Microscopy (PALM) [42], Stochastic Optical Reconstruction Microscopy (STORM) [43], Fluorescence Recovery After Photobleaching (FRAP) [44, 45], and Förster Resonance Energy Transfer (FRET) [46]. The disadvantages of fluorescence microscopy are the need for fluorescent labels, as well as the limited photostability of the labels, which is limited by blinking and bleaching effects [47].

A different approach to obtain nanometer-scale resolved images is the use of smaller wavelengths. Experimentally this can be achieved by employing electrons instead of photons in order to generate the image. According to the *de Broglie* relation the wavelength  $\lambda$  of an electron is  $\lambda = h/p$  (where  $h$  is Planck's constant and  $p$  the momentum of the electron), which results in a resolution of  $\sim 1$  Å for electrons with an energy of 1 keV. This advantageous effect is used in Transmission Electron Microscopy (TEM), where electrons are shot onto a sample and the transmitted electrons are detected [48]. TEM has shown a broad application potential in materials sciences, but also for biological samples. However, due to the high energy of the electrons the sample might be destroyed due to the imaging process and a sophisticated sample preparation is re-

quired in order to obtain samples with electron transparency [49]. The latter issue is addressed by Scanning Electron Microscopy (SEM) [50, 51, 52], where electrons backscattered from the sample, or secondary electrons ejected from the sample are detected. The resolution in SEM, however, is an order of magnitude lower than that of TEM, and in order to obtain the highest spatial resolution the sample has to be conductive.

Another technique offering nanoscale spatial resolution is Scanning Probe Microscopy (SPM) [11]. In SPM a sharp tip is raster-scanned in close proximity across the sample surface, while the interaction between tip and sample is recorded with nanometer resolution in the  $xy$ -plane. The first experimental SPM technique was Scanning Tunnelling Microscopy (STM), introduced in 1982 by Binnig and Rohrer [53, 54, 55] measuring the local tunnelling current between the sharp probe tip and the sample surface as function of the position of the tip. Although delivering a spatial resolution of less than 1 nm [11], STM is restricted to conductive samples. With the development of Atomic Force Microscopy (AFM) [56] this issue could be overcome by measuring the mechanical interaction between probing tip and sample surface [11] instead of the tunnelling current.

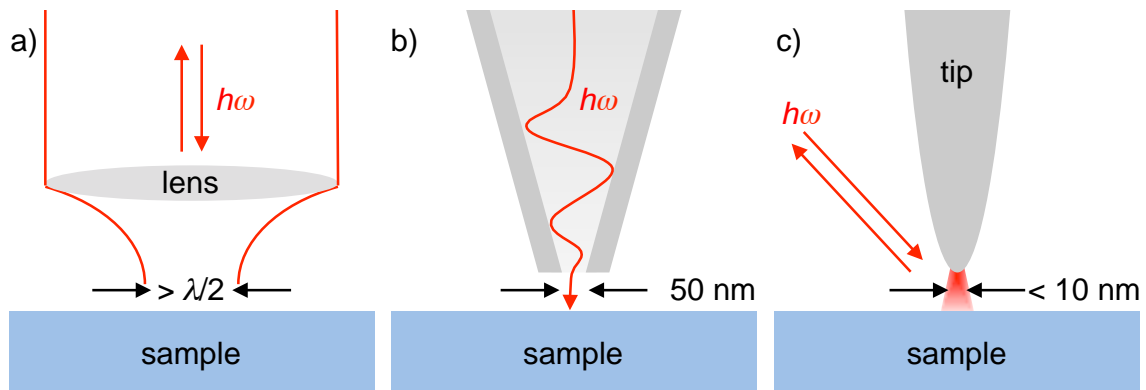


**Figure 2.1: Overview of different microscopy techniques and their resolution limit.** a) Conventional light microscopy, with a diffraction limited resolution of about  $\lambda/2$ . b) a-SNOM, with a resolution limited by the diameter of the aperture to about 50 nm. c) s-SNOM, with a resolution limited by the diameter of the tip to  $< 10$  nm.

Scanning probe microscopy also allows for optical imaging by employing the scanning probe for near-field mapping. Near-fields are electro-magnetic fields that are bound to the object and do not radiate. Thus they are not affected by diffraction. Since they contain information about the smallest features of a sample, accessing them allows for nanoscale resolved imaging of the sample. Several methods have been developed employing optical near-fields in order to obtain nanometer scale resolution, among them aperture SNOM and scattering-type SNOM (a-SNOM and s-SNOM, respectively). In a-

SNOM an aperture with a diameter much smaller than the wavelength is brought close to the sample and used as a tiny light source, while in s-SNOM the optical near-field interaction between a scanning probe tip and the sample is used to obtain nanoscale resolved information about the sample. In the following, both techniques will be explained briefly.

Historically, the first implementation of a microscope using the optical near-fields for imaging has been an aperture SNOM (see Fig. 2.1b). The basic idea though, can be dated back to 1928 [57], when E.H. Synge proposed to use a tiny aperture brought into close proximity of the sample as a minute light source and use far-field methods to detect the light scattered by the sample. Yet, the idea was forgotten, as it could not have been realised experimentally in Synge's lifetime. The first experiments using an aperture to obtain sub-diffraction limited resolution were performed in 1972 by Ash and Nicholls in the microwave regime [58]. It took another 12 years, until 1984, when D. Pohl [59] and A. Lewis [60] independently achieved sub-wavelength resolution at optical frequencies using an aperture a-SNOM. Today's experimental setups are based on an SPM using a metal coated, tapered dielectric fibre with a circular aperture at the end as a near-field probe, like introduced by Betzig *et al.* [61] (see Fig. 2.1b). As typical for SPM, the probe is scanned over the sample and the optical image is generated as a function of the position of the probe above the sample, while the resolution is determined by the diameter of the aperture. Thus, decreasing the diameter of the aperture increases the spatial resolution. However, because of the low transmission of the probes, the resolution in a-SNOM is practically limited to  $\lambda/10 \sim 50$  nm in the visible and to  $1 - 2 \mu\text{m}$  in the infrared spectral range [19, 62].

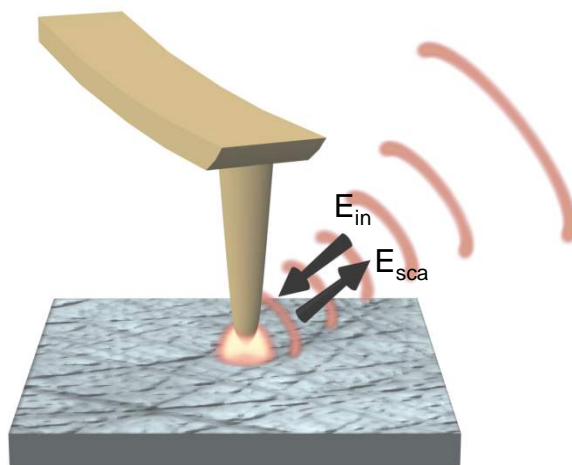


**Figure 2.2:** Illustration of a tip illuminated by a focus laser beam. Image courtesy of Dr. Nenad Ocelic.

An alternative route to employ optical near-fields is taken by s-SNOM (see Fig. 2.1c). J. Wessel suggested in 1985 to use a metal particle as near-field probe [63]. In 1989, H.K. Wickramasinghe filed a patent pursuing Wessel's idea, but replacing the metal sphere by a SPM probe (see Fig. 2.1c) [64]. It took another five years until in 1994 the first experimental results based on the apertureless near-field microscopy approach have been published by the groups of H.K. Wickramasinghe [65], S. Kawata [16], and A.C. Boccara [17]. All groups used either a sharp metal [17] or Si tip [65], which was illuminated by a focused laser beam and the elastically backscattered light was detected (see Fig. 2.2). The tip functions as an optical antenna converting the illuminating radiation into a highly localised and enhanced near-field at the tip apex (see Fig. 2.3) [31, 32, 33, 66]. Due to the optical near-field interaction between tip and sample, the tip-scattered radiation is modified in both its amplitude and its phase, depending on the local dielectric properties of the sample [19]. Importantly, the backscattered light contains not only the near-field signal containing the information about the sample, but it is masked by a much stronger background signal. This background signal stems from light scattered by the sample, by the tip shaft and by the cantilever itself [16, 67]. In order to suppress this detrimental background signal and to obtain the pure near-field signal, sophisticated background suppression methods have been developed. As the near-field interaction between tip and sample strongly depends on the tip-sample distance, operating the AFM in tapping mode causes a modulation of the near-field signal, which in combination with a higher harmonic demodulation and a pseudoheterodyne interferometric detection scheme allows for efficient suppression of the background signal [27, 67, 68, 69]. A more detailed description can be found in the experimental section 2.2.

Interferometric detection of the backscattered light yields nanoscale-resolved amplitude and phase images, revealing the local, complex-valued dielectric properties of the sample. The spatial resolution that can be achieved in s-SNOM hereby only depends on the diameter of the tip, and is wavelength-independent (see Fig. 2.1c) [19, 70]. In fact, s-SNOM has been successfully applied in a broad spectral range, from visible to terahertz frequencies, with a resolution of about 10 nm to 20 nm [21, 23, 31, 33, 71].

Throughout this thesis, near-field imaging and spectroscopy in the IR spectral regime is performed to study the material properties of various nanoscale sample systems. The use of the IR spectral range around 3  $\mu\text{m}$  to 15  $\mu\text{m}$  - also referred to mid-IR - is motivated by the fact that with this wavelength range it is possible to excite different resonant processes, such as vibrational modes in molecules (see chapter 5 and ref. [72]), or phonons and plasmons in semiconductors (see chapters 3,4 and refs. [73, 74]). Be-

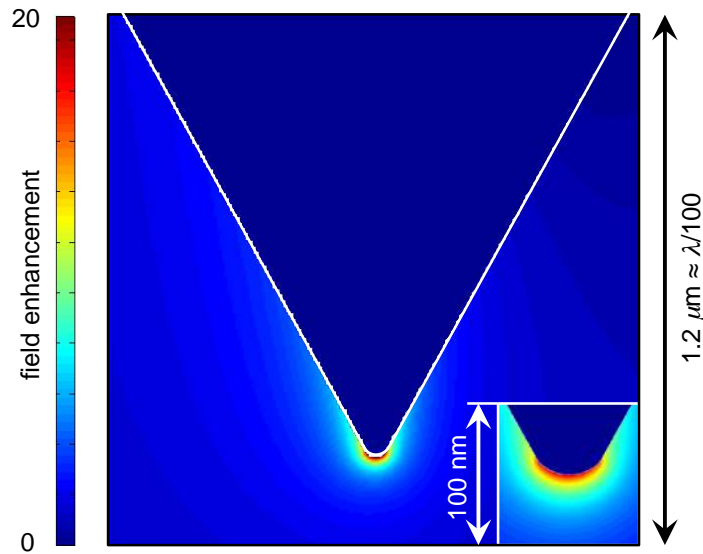


**Figure 2.3:** Calculated field enhancement at the apex of a metallised tip with length  $l = 1 \mu\text{m}$  illuminated with light at a wavelength of  $\lambda = 118 \mu\text{m}$ . Image taken from ref. [31]

cause these resonances are very characteristic for each material system, IR s-SNOM allows for the mapping of local structural properties [75, 76], material composition [23, 31, 77, 78, 79, 80] and the free-carrier concentration [26, 28, 31, 73].

## 2.2 Experimental s-SNOM Setup

In this work two different s-SNOM setups were used. The measurements of the InP nanowires (chapter 3) and the measurements of the SiN nanoparticles (chapter 5) were carried out using a home built s-SNOM setup [81, 82]. The s-SNOM measurements on the ZnO nanowires was performed using a commercial s-SNOM by Neaspec GmbH (<http://www.neaspec.com>). Both microscopes are based on an AFM with a sample scanner, where an additional optical setup for the near-field measurements is added. The working principle for both microscopes is the following. The AFM tip is illuminated by a focused IR laser beam with frequencies between IR 900 and  $1100 \text{ cm}^{-1}$ . The light backscattered from the tip is then recorded interferometrically, simultaneous to the topography.

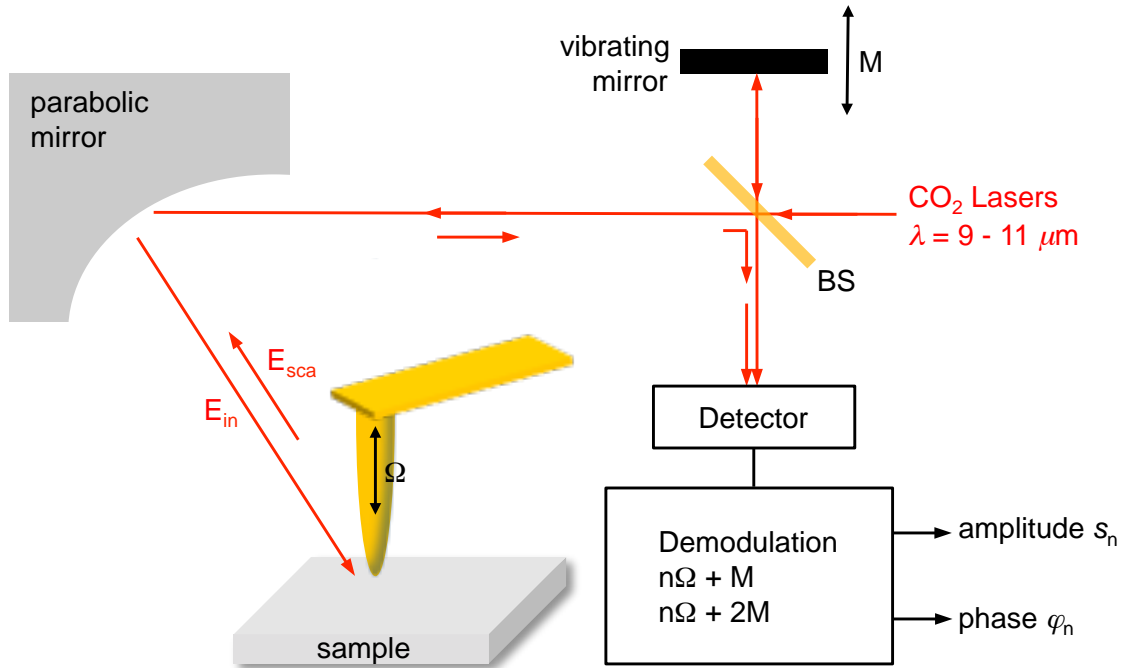


**Figure 2.4:** Experimental setup. A Michelson interferometer is used for detecting the light scattered by the tip. BS labels the beam-splitter of the interferometer. Pseudoheterodyne detection is performed by oscillating the reference mirror with frequency  $M$ . By demodulating the detected signal at  $n\Omega + M$  and at  $n\Omega + 2M$  amplitude  $s_n$  and phase  $\varphi_n$  can be calculated.

## Atomic Force Microscope (AFM)

In AFM a sharp tip at the very end of a cantilever is used to probe the topography and the mechanical interaction between the tip and the sample. For all experiments in this thesis, commercial, metallised Si cantilevers (Nanosensors<sup>TM</sup> PPP-NCHPt and Arrow<sup>TM</sup> NCPt) were used (shown on the left hand side in Fig. 2.4). As is typical for a scanning probe technique, images are generated by translating the sample stage relative to the probing tip in the  $x$ - $y$  plane and scanning the sample line by line. The probe and the sample translation is achieved using piezoelectric actuators, which allow for a nanometer precision in the  $x$ -,  $y$ -directions and even Ångström precision in the  $z$ -direction (height or topography). The AFM is operated in the so-called tapping mode, where the tip is oscillating vertically ( $z$ -direction) just below the cantilever's resonance frequency  $\Omega$  ( $\sim 300$  KHz for both Nanosensors<sup>TM</sup> as well as for Arrow<sup>TM</sup> tips). The tapping amplitudes have been chosen typically between  $A = 20 - 80$  nm. The tapping amplitude is measured by illuminating the backside of the cantilever with a visible laser and measuring the deflection of the reflected laser-spot. As in s-SNOM the measured near-fields critically depend on the tip-sample distance, it is important to control the tip-sample distance and keep it constant throughout the measurement,

*i.e.* the tip needs to follow the topography. Note, that in the tapping mode the tip is oscillating around this constant tip-sample distance. To achieve this distance control, a feedback mechanism is used to keep the tapping amplitude of the cantilever at a constant value, the so-called set point. In case the tapping amplitude decreases below the set point, the feedback mechanism increases the tip-sample distance until the set point is reached again. On the other hand, the feedback mechanism reduces the tip-sample distance in case the tapping amplitude increases above the set point. From the information of this feedback mechanism, the topography of the sample surface can be derived.

## Optical Setup and Tip Illumination

In order to obtain background-free IR amplitude and phase information about a sample we used an interferometric setup with a pseudoheterodyne detection scheme. It is basically an Michelson interferometer, where a beamsplitter splits the incoming IR laser beam  $E_{\text{in}}$  into two paths: (i) The transmitted light illuminates the AFM tip, and is therefore called probe arm. (ii) The reflected light is directed to a reference mirror. This path is called reference arm. In the probe arm, a parabolic mirror (with a NA  $\sim 0.5$ ) is used to focus the incoming laser light onto the AFM tip. The illuminated metallic tip functions as an IR antenna converting the illumination radiation into a highly concentrated and enhanced near-field at the very apex of the tip [31, 32, 33, 66], similar to Raman spectroscopy [83, 84, 85, 86]. Owing to the optical near-field interaction between tip and sample, the light scattered by the tip is modified in both its amplitude  $s$  and phase  $\varphi$ , depending on the local dielectric properties of the sample [19]. We can express the backscattered light originating from the tip-sample near-field interaction by

$$E_{\text{nf}} = \sigma_{\text{nf}} E_{\text{in}}, \quad (2.1)$$

with

$$\sigma_{\text{nf}} = s e^{i\varphi}, \quad (2.2)$$

where  $\sigma_{\text{nf}}$  denotes the near-field scattering coefficient of the tip-sample system [81, 87]. As the focus of the incoming laser beam is diffraction limited, it is several microns in diameter in the mid IR range. Thus, not only the tip is illuminated and scatters light, but also the sample, the shaft of the tip and the cantilever. This detrimental scattered

light contributes a background signal, which can be expressed as

$$E_{bg} = \sigma_{bg} E_{in}, \quad (2.3)$$

with

$$\sigma_{bg} = s_{bg} e^{i\varphi_{bg}}, \quad (2.4)$$

where  $\sigma_{bg}$  denotes the scattering coefficient of the background scattering. The parabolic mirror is used to collect both contributions,  $E_{in}$  and  $E_{bg}$ , of the backscattered light, and the total backscattered field is given by

$$E_{sca} = E_{nf} + E_{bg} = \sigma_{sca} E_{in}, \quad (2.5)$$

with

$$\sigma_{sca} = \sigma_{nf} + \sigma_{bg}. \quad (2.6)$$

Note, that in order to keep the tip always in the focus of the laser spot during scanning the tip is fixed. During the measurement the sample is scanned below the fixed tip, using a piezo driven sample scanner.

## Interferometric Signal Detection and Background Suppression

In the reference arm, the incident light  $E_{in}$  is reflected at a reference mirror, which oscillates at frequency  $M$  causing a modulation of the phase of the reference beam  $E_{ref}$ , which can be written as (see [69, 81])

$$E_{ref} = e^{i\gamma \sin(Mt)} E_{in}, \quad (2.7)$$

with  $\gamma$  being the amplitude of the modulation. Part of that reflected beam  $E_{ref}$  is transmitted through the beam splitter towards the detector, while another part is reflected at the beamsplitter. Finally, at the detector the interference of  $E_{sca}$  and  $E_{ref}$  is detected using a Mercury Cadmium Telluride (MCT) detector.

To obtain an efficient suppression of unwanted background signals and to obtain the amplitude and phase information of the light backscattered from the sample, the combination of pseudoheterodyne interferometric detection and higher harmonic demodulation of the measured signals is necessary. In the following, it will be described how the near-field contribution can be extracted from the light backscattered from the AFM tip.

At the detector the superposition of the light collected by the parabolic mirror  $E_{\text{sca}} = E_{\text{nf}} + E_{\text{bg}}$  and the reference beam  $E_{\text{ref}}$  are detected. The measured electric signal  $U$  at the detector is proportional to the intensity  $I_{\text{det}}$  of the light at the detector, and is given by

$$U \propto I_{\text{det}} = |E_{\text{det}}|^2 = E_{\text{det}} E_{\text{det}}^* = (E_{\text{nf}} + E_{\text{bg}} + E_{\text{ref}}) (E_{\text{nf}} + E_{\text{bg}} + E_{\text{ref}})^*. \quad (2.8)$$

In the experiment, the AFM is operated in the tapping mode, *i.e.* the tip oscillates at a frequency  $\Omega$ . both the background  $E_{\text{bg}}$  signal and the field backscattered from the tip  $E_{\text{nf}}$  depend nonlinearly on the tip-sample distance as shown in the model calculations (eqs. (2.23) and (2.26)) in chapter 2.3. Because of the modulation of the tip-sample distance at frequency  $\Omega$  and the nonlinear distance dependency of  $E_{\text{nf}}$  and  $E_{\text{bg}}$ , their contributions to  $U$  yield higher harmonics at  $n\Omega$ , with  $n \geq 1$ . The interference of both  $E_{\text{nf}}$  and  $E_{\text{bg}}$  with the phase modulated reference beam  $E_{\text{ref}}$  at the detector thus generates sidebands at frequencies  $f = n\Omega \pm mM$  with  $n, m$  being integer numbers. Therefore, the electric signal  $U$  generated by the detector yields a frequency spectrum as shown in Fig. 2.5, where the centre frequencies  $n\Omega$  are depicted in black, while the side bands  $n\Omega + mM$  are coloured in red.

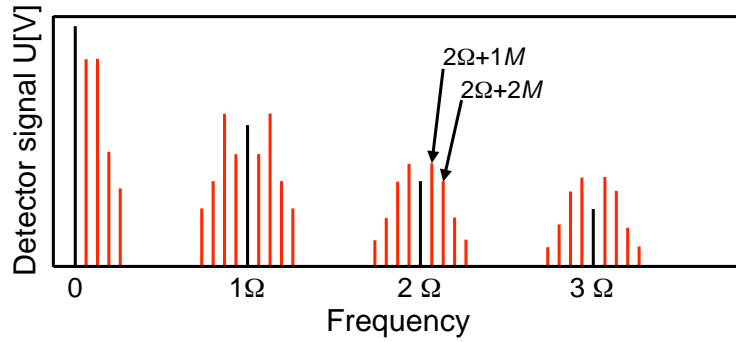


**Figure 2.5:** Schematic representation of the frequency spectrum at the detector when a pseudoheterodyne interferometric detection is used.  $\Omega$  denominates the tip vibration frequency and  $M$  the vibration frequency of the reference mirror. Figure adopted from [81].

In order to obtain amplitude and phase of the near-field contribution, the detector signal is demodulated. This demodulation process can be described mathematically by a Fourier analysis of the detected signals as shown in [69] and we can write for  $E_{\text{nf}}$  and  $E_{\text{bg}}$

$$E_{\text{nf}} = \sum_{n=0}^{\infty} \sigma_{\text{nf},n} \cos(n\Omega t) E_{\text{in}}, \quad (2.9)$$

and

$$E_{\text{bg}} = \sum_{n=0}^{\infty} \sigma_{\text{bg},n} \cos(n\Omega t) E_{\text{in}}, \quad (2.10)$$

with

$$\sigma_{\text{nf},n} = s_n e^{i\varphi_n}, \quad (2.11)$$

and

$$\sigma_{\text{bg},n} = s_{\text{bg},n} e^{i\varphi_{\text{bg},n}}. \quad (2.12)$$

$\sigma_{\text{nf},n}$  and  $\sigma_{\text{bg},n}$  hereby denote the complex-valued Fourier coefficients of the scattering coefficients  $\sigma_{\text{nf}}$  and  $\sigma_{\text{bg}}$ , as defined in equations (2.1) and (2.3).

In earlier works [81, 82, 88] it has been shown that the  $n$  – th Fourier coefficient of the tip-scattered light  $\sigma_{\text{sca},n} = \sigma_{\text{nf},n} + \sigma_{\text{bg},n}$  can be derived from the first and the second sideband,  $U_{n,1}$  and  $U_{n,2}$ , respectively (marked for  $n = 2$  in Fig. 2.5). It can be shown [81] that by setting the amplitude  $\gamma$  of the phase modulation in eq. (2.7) to  $\gamma = 2.63$  the higher harmonics of the tip-scattered light are obtained according to

$$\sigma_{\text{sca},n} = \sigma_{\text{nf},n} + \sigma_{\text{bg},n} = 2.16k (U_{n,2} + iU_{n,1}), \quad (2.13)$$

with  $k$  being a complex-valued constant that is related to the alignment of the Michelson interferometer.

The detrimental background in eq. (2.13) can be efficiently suppressed by choosing high ( $n \geq 2$ ) demodulation orders. Because the tip-sample near-field interaction depends strongly on the tip-sample distance, the oscillation of this distance causes a strong modulation of the near-field scattering  $E_{\text{nf}}$ . This modulation contributes significantly even to higher harmonics of  $\sigma_{\text{nf},n}$ , while in the background scattering  $\sigma_{\text{bg},n}$  most of the energy is found in the low harmonics of  $\sigma_{\text{bg},n}$ , as can be seen from ref. [69]. Thus, for high harmonics, we can neglect the background scattering, obtaining  $\sigma_{\text{sca},n} \approx \sigma_{\text{nf},n}$ . The  $n$  – th order near-field amplitude  $s_n$  and phase  $\varphi_n$  then are given as

$$s_n = 2.16k \sqrt{U_{n,1}^2 + U_{n,2}^2}, \quad (2.14)$$

and

$$\varphi_n = \arctan \left( 2.16k \frac{U_{n,2}}{U_{n,1}} \right), \quad (2.15)$$

respectively. Hence, by measuring the first two sidebands  $U_{n,1}$  and  $U_{n,2}$  of the  $n$  – th harmonic, it is possible to obtain the  $n$  – th order amplitude and phase,  $s_n$  and  $\varphi_n$ , respectively.

## Spectroscopic Near-field Imaging

In chapters 3 and 5 spectroscopic near-field imaging is employed in order to study the dielectric properties of the samples as a function of the frequency of the incident light. In the following, we will outline how spectroscopic imaging in s-SNOM has been performed experimentally.

As a first step, near-field imaging of the desired sample region is performed at a fixed frequency  $\omega$ , and the near-field amplitude and phase signal are recorded. After this, the laser is manually detuned to a new frequency, which is subsequently controlled by coupling the laser beam into a spectrometer. With the new frequency, another near-image of the same sample region is recorded. Hereby, it is important to minimise the lateral drift between two measurements and try to record exactly the same sample region. This process of detuning the laser, controlling the laser frequency and recording the same sample region is repeated for as many frequencies as desired. In order to obtain near-field amplitude and phase spectra, we extract from the different near-field images amplitude and phase values at a particular sample position and plot them as a function of the illumination wavelength.

## 2.3 Theory of s-SNOM

Several models have been proposed to calculate the field scattered by the AFM tip, which is modified due to the near-field interaction between the tip and the sample (see Fig. 2.6). The aim of these models in the first step is to describe the experimentally measured near-field amplitude and phase signals  $s_n$  and  $\varphi_n$  (see eqs. (2.14) and (2.15)). As a more advanced goal, these models should also be able to extract information about the local dielectric properties, *i.e.* the dielectric function  $\epsilon_s$  of the sample.

The most common models are the dipole model (see Fig. 2.6a) and the finite-dipole model (see Fig. 2.6b). In both models the tip is described by a dipole. While in the former the tip is approximated by a point dipole, in the latter a finite-dipole is used to describe the tip. The sample in both models is described by a semi-infinite half space, characterised by its dielectric function  $\epsilon_s$ . Both models calculate the near-field interaction between the tip with the sample when the tip is in close proximity to the sample. Due to the near-field interaction between tip and sample, the sample acts back on the tip dipole. The tip is accordingly described by an effective dipole. In case the sample is smaller than the tip, the geometry of the sample has to be taken into

account. This can be done in the framework of the extended finite-dipole model, which describes the near-field interaction between tip, particle and substrate for the situation where a small sphere is located on top of the substrate (see Fig. 2.6c).

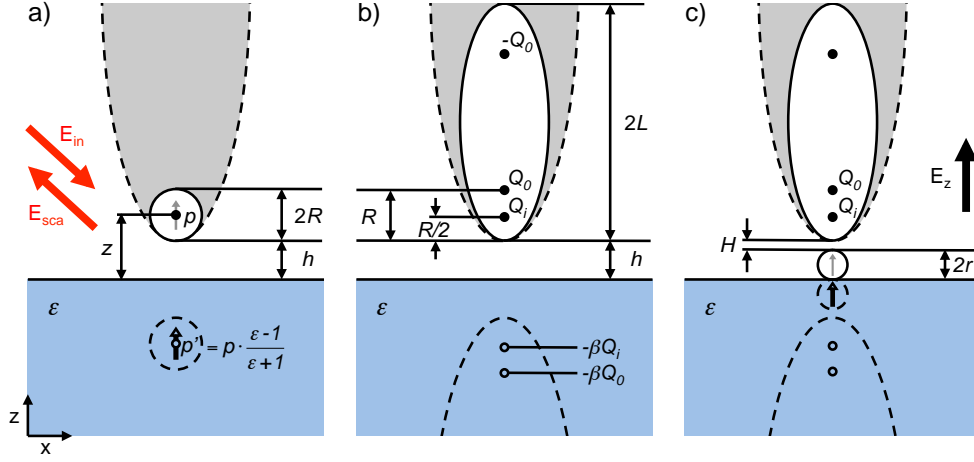


**Figure 2.6:** Comparison of the three analytical models used in the framework of this thesis, in order to calculate the optical near-field contrasts. (a) Dipole model, where the tip is reduced to a point dipole [27, 89]. (b) Finite-dipole model, where the tip is described by a spheroid, and (c) the extended finite dipole model, where taking into account the finite size of the sample.

## Dipole Model

In the dipole model [27, 89], the AFM tip is approximated by a small metal sphere, with radius  $R$ , inscribed into the apex of the tip as depicted in Fig. 2.6a. When the tip is illuminated, the incident light, described by the electric field  $E_{in}$ , polarises that sphere. The polarisation of the metal sphere can be described by that of a point dipole located in the centre of the sphere and which is given by

$$p = \alpha E_{in}, \quad (2.16)$$

where  $\alpha$  describes the polarisability of the sphere as [90]

$$\alpha = 4\pi R^3 \frac{\epsilon - 1}{\epsilon + 2} \quad (\text{in air}). \quad (2.17)$$

The dielectric value of the sphere's material hereby is given by  $\epsilon$  [90].

It is assumed that the dipole is polarised vertically (along the  $z$ -axis), because of the elongated shape of the tip. This polarisation scheme is referred to as  $p$ -polarisation.

The interaction of the tip dipole and the sample can be described by the interaction of the dipole  $p$  with its mirror dipole  $p'$ , which is induced in the sample when the tip comes close. This mirror dipole can be written as

$$p' = \beta p, \quad (2.18)$$

where  $\beta$  is the so-called surface response function, which depends on the local dielectric properties of the sample as follows:

$$\beta = \frac{\varepsilon_s - 1}{\varepsilon_s + 1}, \quad (2.19)$$

$\varepsilon_s$  is the local dielectric function of the sample.

The local electric field at the tip dipole then is a sum of the incoming field  $E_{\text{in}}$  and  $E'$ , the field that the mirror dipole generates at the position of the tip dipole. In the electrostatic approximation,  $E'$  is given by

$$E' = \frac{p'}{2\pi(2z)^3}, \quad (2.20)$$

with  $z = R + h$  being the distance between the tip and the sample as shown in Fig. 2.6a. For the dipole moment of the tip dipole then follows

$$p = \alpha (E_{\text{in}} + E') = \alpha \left( E_{\text{in}} + \frac{p'}{2\pi(2z)^3} \right). \quad (2.21)$$

Inserting equation (2.18) into equation (2.21), we obtain a self-consistent solution for  $p$ :

$$p = \frac{\alpha}{1 - \frac{\alpha\beta}{2\pi(2z)^3}} E_{\text{in}} = \frac{\alpha}{1 - \frac{\alpha\beta}{16\pi(R+h)^3}} E_{\text{in}}. \quad (2.22)$$

$p$  is referred to as effective polarisability of the tip. In order to describe the response of the tip-sample system to the incident field  $E_{\text{in}}$ , we define an effective polarisability, which is given by

$$\alpha_{\text{eff}} = \frac{p}{E_{\text{in}}} = \frac{\alpha}{1 - \frac{\alpha\beta}{16\pi(R+h)^3}}. \quad (2.23)$$

The dipole model allows generally for a qualitative understanding of the near-field interaction between a probing tip and a sample and describes well s-SNOM experiments with polymer samples [22, 23, 24]. However, it cannot correctly reproduce the spectral position, the width and the magnitude of polariton-resonant tip-sample near-field interactions [21, 27, 91].

In order to obtain an experimentally measurable quantity, we use the relation  $E_{\text{nf}} = \sigma_{\text{nf}} E_{\text{in}}$  between the light backscattered from the tip  $E_{\text{nf}}$  and the incoming light  $E_{\text{in}}$  as introduced in eq. (2.1). Because the near-field scattering coefficient  $\sigma_{\text{nf}}$  is proportional to the dipole moment  $p$  of the coupled tip-sample system and thus to the effective polarisability of the tip, we obtain the following relation  $\alpha_{\text{eff}} \propto \sigma_{\text{nf}} = se^{i\varphi}$ . To take into account the tip-oscillation and the higher-order signal demodulation, we calculate the time course of  $\alpha_{\text{eff}} = \alpha_{\text{eff}}[h(t)]$  with  $h = A(1 + \cos(\Omega t))$ . Performing a Fourier analysis of  $\alpha_{\text{eff}}[h(t)]$  we obtain the Fourier coefficients  $\alpha_{\text{eff},n}$ , where  $\alpha_{\text{eff},n}$  is the  $n$ -th Fourier coefficient, corresponding to the  $n$ -th demodulation order. From  $\alpha_{\text{eff},n}$  we obtain the amplitude and phase of the  $n$ -th demodulation order as

$$s_n \propto |\alpha_{\text{eff},n}|, \quad (2.24)$$

and

$$\varphi_n = \arg(\alpha_{\text{eff},n}). \quad (2.25)$$

## Finite Dipole Model

In order to overcome the constraints of the dipole model, the so-called finite-dipole model has been developed [81, 92]. Instead of describing the tip by a sphere, it is described by a spheroid with length  $2L$  in order to take into account that the tip in the experiment is an elongated structure (see Fig. 2.6b). Calculations have shown that the field in the proximity of such a spheroid can be described by an extended or finite dipole, rather than a point-dipole [81, 92]. At large distances from the tip, the electric field of the spheroid converges to that of a point-dipole again.

The incident field induces two charges  $Q_0$  and  $-Q_0$ , each with a distance  $R$  from the respective tip apex. From these two charges only  $Q_0$  (positioned closer to the sample surface) participates in the near-field interaction [81, 92]. The dipole moment of the spheroid then can be noted down as  $p_0 = 2LQ_0$ . When the tip comes close to a sample surface, an image charge  $Q'_0 = -\beta Q_0$  is induced in the sample. The image charge  $Q'_0$  acts back on the spheroid, where it induces an additional point charge  $Q_i$  close to the tip apex at a distance of  $R/2$  from the tip apex, whereas the opposite charge  $-Q_i$  is distributed along the spheroid. The charge  $Q_i$  in turn induces an image point charge  $Q'_i$  in the sample, which again can be described using the surface response function  $\beta$  as  $Q'_i = -\beta Q_i$ . Note that in the finite dipole model  $Q_0$  is determined by the incident field and the geometry of the spheroid only, whereas  $Q_i$  and  $Q'_i$  are determined by the

dielectric properties of the sample.

Similar to the dipole model, we can define an effective dipole moment in the finite-dipole model for the spheroid as  $p_{\text{eff}} = p_0 + p_i$ , where  $p_0$  is the dipole moment caused by the external field, while  $p_i$  reflects the dipole moment evoked by the tip-sample near-field interaction. The latter is given by  $p_i = \eta Q_i L$ , where  $\eta$  is the so-called "near-field contrast factor". It is a dimensionless number for the strength of the (optical) near-field interaction between the spheroid and the sample [81]. We then can calculate the tip scattered light, which is given as  $E_{\text{sca}} \propto p_{\text{eff}} = \alpha_{\text{eff}} E_{\text{in}}$ , with  $\alpha_{\text{eff}}$  being the effective polarisability of the tip. According to refs. [81] and [92], the effective polarisability can be expressed as

$$\alpha_{\text{eff}} = R^2 L \frac{\frac{2L}{R} + \ln\left(\frac{R}{4eL}\right)}{\ln\left(\frac{4L}{e^2}\right)} \left( 2 + \frac{\beta\left(g - \frac{R+h}{L}\right) \ln\left(\frac{4L}{4h+3R}\right)}{\ln\left(\frac{4L}{R}\right) - \beta\left(g - \frac{3R+4h}{4L}\right) \ln\left(\frac{2L}{2h+R}\right)} \right). \quad (2.26)$$

This solution for  $\alpha_{\text{eff}}$  requires five parameters:

- $h$ , the tip-sample distance. This value can be determined experimentally.
- $\beta$ , the surface response function of the sample, which can be determined using the dielectric function  $\varepsilon(\omega)$  of the sample.
- $R$ , the tip radius. This value is set to a value between 20 nm to 40 nm as specified by the manufacturer of the tip.
- $L$ , the effective length of the spheroid.
- $g$ , a complex factor describing the total charge induced in the spheroid.

In the limit of the electrostatic approximation it is required that  $2L$  is much smaller than the wavelength of the incident light. The last two parameters,  $L$  and  $g$ , are determined by searching for the best agreement between experimental and calculated data. The best values found are  $L = 300$  nm [82, 88], and  $g = 0.7e^{0.06i}$  [88]. While  $g$  is kept fixed throughout this complete thesis, for  $L$  a value of 300 nm is used in the case of the InP (see chapter 3) and  $\text{Si}_3\text{N}_4$  (see chapter 5), and a value of 600 nm for the ZnO nanowire samples in chapter 4 in accordance with a recent study of the effective dipole length by Amarie and Keilmann [93].

## Extended Finite-Dipole Model

The extended finite-dipole mode was developed by A. Cvitkovic [88] to calculate amplitude and phase signals for a small sphere (representing a molecule or a nanoparticle)

on a substrate. Hereby, it is assumed, that the radius of the sphere  $r$  is smaller than the tip radius ( $R$ ). The model is based on the finite-dipole model, where the sample is treated as semi-infinite half-space. To model the near-field signals of a sample smaller than the tip apex we assume that we can describe the sample as a sphere with radius  $r$ , located in between the substrate and the tip. The polarisability of a sphere can be described by  $\alpha_{\text{sphere}} = 4\pi r^3(\epsilon(\omega) - 1)/(\epsilon(\omega) + 2)$  [90]. In contrast to the finite-dipole model not only the tip-substrate coupling needs to be considered, but rather the coupling between the convoluted system of tip (described as spheroid), sample (described as sphere) and substrate (described as semi-infinite half-space). From the extended finite-dipole model then again  $\sigma = se^{i\varphi}$  is calculated numerically. Taking into account the tip-sample distance modulation, we obtain  $n$  -  $th$  harmonics of the near-field amplitude  $s_n(r)$  and phase  $\varphi_n(r)$  signals as a function of the sample-sphere radius  $r$ .



# 3

## **Nanoscale Resolved Free-carrier Profiling in Individual InP Nanowires**

*In this chapter we demonstrate quantitative, noninvasive and nanoscale-resolved mapping of the free-carrier distribution in indium phosphide (InP) nanowires with doping modulation along the axial and radial directions by employing infrared (IR) near-field nanoscopy. Owing to the technique's capability of subsurface probing, we provide direct experimental evidence that dopants in interior nanowire shells effectively contribute to the local free-carrier concentration. The high sensitivity of s-SNOM also allows us to directly visualise nanoscale variations in the free-carrier concentration of wires as thin as 20 nm, which we attribute to localised growth defects. Our results open interesting avenues for studying the local conductivity in complex nanowire heterostructures, which could be further enhanced by near-field IR nanotomography.*

### 3.1 Introduction

Semiconductor nanowires bear an enormous potential for future electronic and optoelectronic devices [4, 5, 6, 7, 8, 9]. A widely used method for the bottom-up fabrication of semiconductor nanowires is the vapor-liquid-solid (VLS) growth mode, which will be explained in more detail in this chapter (see 3.3 on page 36). It allows to grow nanowires with diameters ranging from  $\sim 5$  to 100 nm and up to several micrometer in length resulting in aspects ratios of 1000 and more. More importantly VLS growth allows to influence and modify the local chemical composition [94], as well as the doping concentration [95] within the nanowires during the growth process. This possibility to control the physical properties on an atomic level may open the door to completely new electronic structures and devices [96]. The successful application of nanowires in technology, however, will rely critically on the control and the experimental verification of the local free-carrier concentration [9, 10, 97, 98], which creates the need for novel imaging techniques. In this chapter we show nanoscale mapping of free carriers in axially and radially modulation-doped InP nanowires (see Figure 3.1) by s-SNOM.

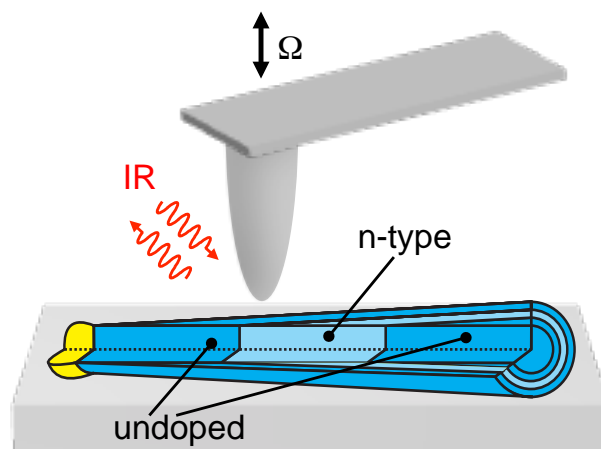


**Figure 3.1:** Schematic illustration of free-carrier profiling of modulation-doped semiconductor nanowires by IR s-SNOM.

### 3.2 Theoretical Near-field Contrast of Highly Doped Semiconductors

Before we begin studying the free-carriers in highly doped InP nanowires experimentally, we introduce and discuss the theoretical background that allows to determine the

free-carrier concentration in semiconductors using IR light.

Light can be used to excite collective vibrations of the free carriers (Plasmon Polaritons) in a doped semiconductor. The oscillation frequency of the free carriers is called plasma frequency  $\omega_P$  and depends on the free-carrier concentration  $n$  and the effective mass  $m_{\text{eff}}$  of the free carriers according to refs. [99] and [100] as

$$\omega_P^2 = \frac{ne^2}{\epsilon_0 \epsilon_\infty m_{\text{eff}}}, \quad (3.1)$$

with  $e$  being the electronic charge and  $\epsilon_\infty$  describing the polarisation at higher frequencies.

To describe the dielectric properties of a doped semiconductor we use a Drude-term in the dielectric function to take account of the free-carriers. The dielectric function for a doped semiconductor depending on the frequency  $\omega$ , then is given by [101, 102, 103]

$$\epsilon(\omega) = \epsilon_\infty \cdot \left(1 - \frac{\omega_P^2}{\omega^2 + i\omega\gamma}\right), \quad (3.2)$$

where  $\gamma$  denotes the damping, which scales inversely with the concentration-dependent carrier mobility  $\mu(n)$  as  $\gamma \propto 1/\mu$ . Inserting literature data for bulk InP ( $\epsilon_{\infty, \text{InP}} = 9.61$ ,  $m_{\text{eff, InP}} = 0.075m_0$  (with the electron rest mass  $m_0$ ) and  $\mu_{\text{InP}}(n)$  as a function of the free-carrier concentration  $n$ , all taken from [104, 105]) into eq. (3.2) we obtain the dielectric function  $\epsilon_{\text{InP}}$  for InP. Fig. 3.2a shows the real part  $\text{Re}[\epsilon_{\text{InP}}]$  of  $\epsilon_{\text{InP}}$  for four different free-carrier concentrations ( $n = 10^{16}$ ,  $10^{17}$ ,  $10^{18}$ , and  $10^{19} \text{ cm}^{-3}$ ). For all free-carrier concentrations we find that  $\text{Re}[\epsilon_{\text{InP}}]$  is negative for small frequencies and increases for larger frequencies. At the plasma frequency  $\omega_P$  the function  $\text{Re}[\epsilon_{\text{InP}}]$  changes the sign and is characteristic for each free-carrier concentration. As seen in eq. (3.1)  $\omega_P$  shifts to higher frequencies with higher free-carrier concentrations.

Far-field optical spectroscopy, especially in the IR and terahertz (THz) regime, allows to visualise, and more importantly to determine the free carrier-concentration, using the fact that the Fresnel reflectivity  $R$  depends on the local dielectric function  $\epsilon$ , as follows:

$$R = \left| \frac{\sqrt{\epsilon} - 1}{\sqrt{\epsilon} + 1} \right|^2. \quad (3.3)$$

In Fig. 3.2b the Fresnel reflectivity  $R$  for the free-carrier concentrations  $n = 10^{16}$ ,  $10^{17}$ ,  $10^{18}$ , and  $10^{19} \text{ cm}^{-3}$  is shown. For all free-carrier concentrations we find that below the plasma frequency  $\omega_P$  InP shows a high value close to 1, resembling a high reflectivity. For frequencies larger than  $\omega_P$  we find a low reflectivity. As the transition from high

to low reflectivity occurs at  $\omega_p$  it is called Plasma-edge. Due to the frequency dependency of the Plasma-edge a measurement of the Fresnel-reflectivity as a function of  $\omega$  allows to determine the free-carrier concentration  $n$  using optical far field techniques [106]. It can also be seen that for the technologically interesting high free-carrier concentrations ( $\sim 10^{19} \text{ cm}^{-3}$ ) the Plasma edge can be found at mid-IR frequencies around  $1000 \text{ cm}^{-1}$ . Because of the diffraction limit, however, far-field reflection spectroscopy cannot be applied to determine the free-carrier concentration in nanoscale samples, such as nanowires.

To illustrate how s-SNOM can be employed to map free-carriers in doped semiconductor nanowires, we calculate the amplitude  $s_2$  (Fig. 3.2c) and phase  $\varphi_2$  (Fig. 3.2d) of the tip-scattered radiation as a function of the illumination frequency  $\omega$  and normalise both spectra to the value obtained for a Au sample. For this calculations we use the finite-dipole model as described in chapter 2.3). In the near-field amplitude spectra (Fig. 3.2c) we observe a distinct resonance, represented by a peak which is followed by a dip in the calculated spectra, which is accompanied by a bell-shaped resonance peak in the phase spectra (Fig. 3.2c). The spectral position of both the amplitude and the phase maxima, shifts to higher frequencies with higher doping concentrations. At the same time, the resonance becomes stronger with an increase of the free-carrier concentration. This resonance in the near-field amplitude and phase spectra can be explained by a plasmon-resonant near-field interaction [30, 31] between the tip and the doped InP surface, which typically occurs near the Plasma frequency  $\omega_p$ . It occurs close to  $\text{Re}[\varepsilon_s] = -1$  (indicated by the vertical dashed lines in Fig. 3.2a), because according to eq. 2.19 the denominator of the surface response function  $\beta = (\varepsilon_s - 1)/(\varepsilon_s + 1)$  becomes zero. We can use this characteristic near-field amplitude and phase behaviour for determining the free-carrier concentration  $n$  from experimentally recorded near-field spectra (see chapter 3.5).

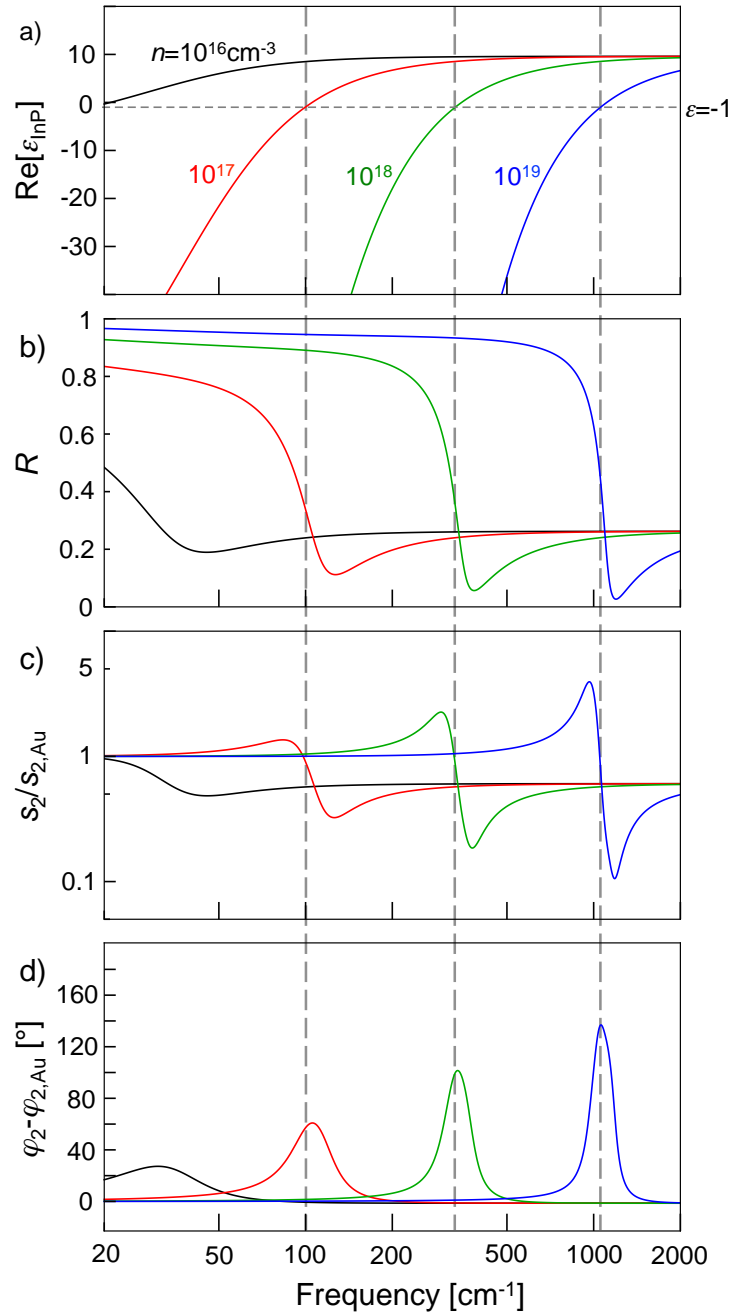


**Figure 3.2: Illustration of the relation between dielectric function and optical properties of bulk InP for different free-carrier concentrations  $n$  ranging from  $10^{16}$  to  $10^{19}$ .** (a) Real part of the dielectric function  $\epsilon(n)$ . (b) Fresnel reflectivity  $R$  showing the transition from high to low reflectivity as a function of the frequency. (c, d) Calculated near-field amplitude  $s_2$  and phase  $\varphi_2$  spectra. The calculations were carried out employing the finite-dipole model 2.3 and normalised to the s-SNOM signal obtained for an Si sample. We note that for illustrating the plasmonic s-SNOM response in Figure 3.8 we neglect the contribution of optical phonons in InP at around  $350\text{ cm}^{-1}$ .

### 3.3 Sample Fabrication

In order to demonstrate the capability of s-SNOM to map free-carriers in semiconductor nanowires we choose modulation doped InP nanowires as a sample system. On the other hand, InP is a direct bandgap semiconductor, with a bandgap energy of 1.344 eV which makes it a highly interesting material system with a large application potential for electronic and optoelectronic devices [107].

#### Vapor-Liquid-Solid (VLS) Growth of InP Nanowires

The InP nanowires were grown by the vapor-liquid-solid (VLS) growth mechanism. This growth mechanism was first introduced by Wagner and Ellis in 1964 to describe the growth of semiconductor nanowires in general [108]. In 2000, Duan and Lieber [109] demonstrated its usability for the growth of InP nanowires. VLS growth offers various advantages to the grower. The most important ones are its applicability to a wide range of different semiconductor material systems such as Si [110, 111], Ge [111], InP [109, 112], GaP [109, 113, 114], GaAs [115, 116], GaN [117, 118], and ZnO [4, 119]. Furthermore it offers the possibility to grow the nanowires on a different substrate than the nanowire material itself. And finally, it is possible to grow radial as well as axial hetero-structures by controlling the growth conditions during the nanowire growth process.

In VLS growth a metal particle is used to catalyze a directional, axial growth resulting in a nanowire with a thickness determined by the diameter of the seeding metal catalyst. Fig. 3.3 schematically outlines the VLS growth at the example of InP nanowires. The growth process can be described by three main phases:

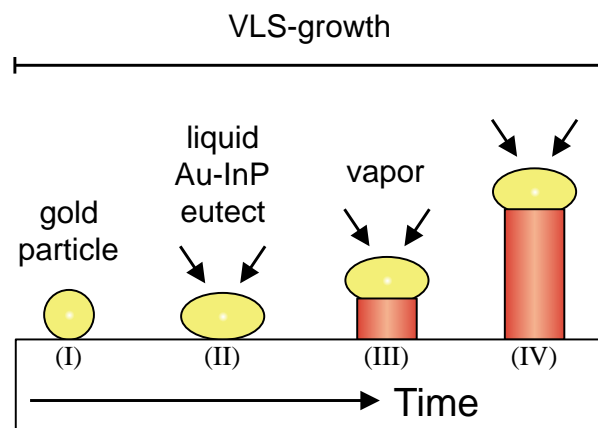
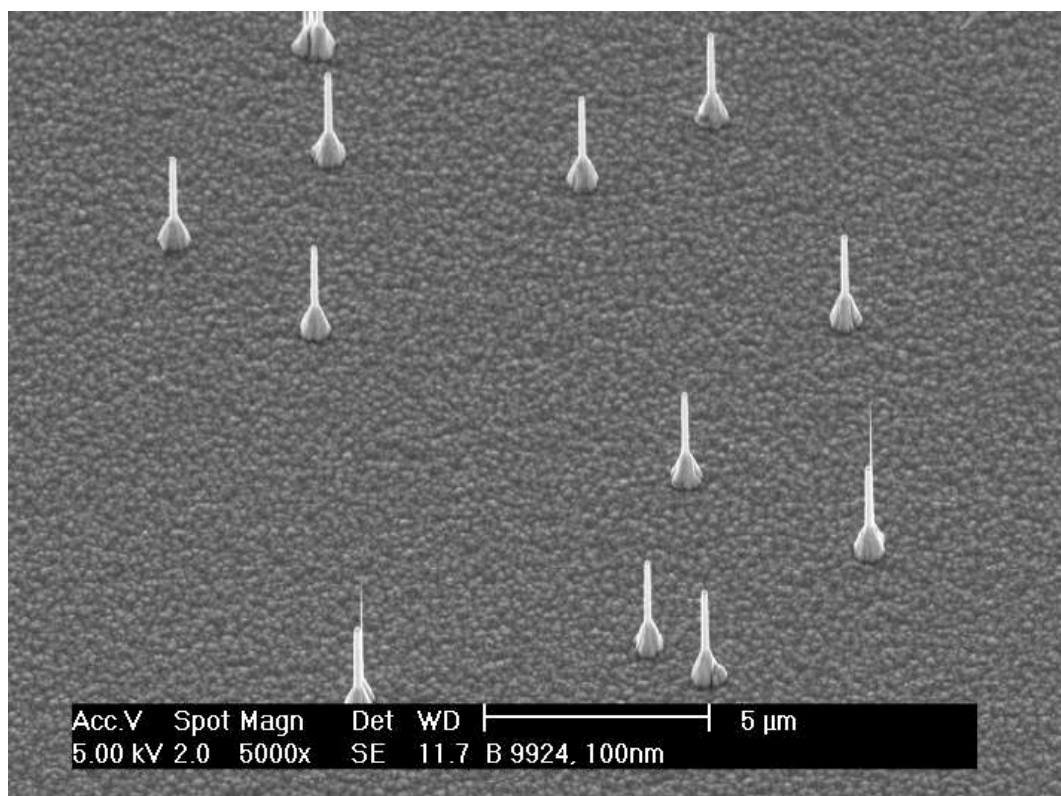


Figure 3.3: VLS Growth of InP nanowires. Adapted from [120]

- (i) First, a target substrate, in this case an InP wafer decorated with Au particles serving as catalyst, is brought into a growth reactor. The sample is then heated to a temperature higher than the Au-InP eutectic point. At this point the Au melts and forms small liquid Au-InP alloy droplets (see Fig. 3.3 (I)).
- (ii) In a second step, precursor gases for the InP nanowire growth are added to the reaction chamber. Indium and phosphor from the precursor gases absorb at the surface of the Au-InP alloy droplet and diffuse into the droplet (see Fig. 3.3 (II)).
- (iii) Finally, when the Au-InP alloy is over-saturated with the semiconductor material, growth is seeded at the interface to the substrate. The growth only takes place at the interface between the liquid droplet and the substrate. Thereby the catalyst particle always stays on top of the growth zone, inducing a highly localised and directional growth of the semiconductor material resulting in the formation of a nanowire (see Fig. 3.3 (III)-(IV)). In Fig. 3.4 an SEM overview of InP nanowires on an InP wafer after the final VLS growth phase is shown.



**Figure 3.4:** SEM image of InP nanowires with a diameter of 100 nm taken directly after the VLS growth. Image courtesy of J. Gomez Rivas, Amolf/Philip Research Laboratories (The Netherlands).

Compared to other growth techniques from the gas phase, the VLS growth mode is characterised by its higher growth speed. This is due to the catalytic effect of the metal

particle. However, uncatylased vapor-solid growth also takes place simultaneously, although at a much slower growth rate. As a result, nanowires grown by the VLS growth mode might be tapered. By optimising the growth parameters (*e.g.* the temperature during growth), the tapering effect can be minimised. On the other hand, the intentional change of the growth parameter during the growth process, which results in an overgrowth of existing segments with a thin shell determined by the changed growth conditions, can be used to produce radial heterostructures [121, 122, 123, 124].

### Growth Parameters

For our experiments InP nanowire samples were grown, prepared and precharacterised by S.L. Diedenhofen, J. Gomez Rivas, R.E. Algra, E.P.A.M. Bakkers at the Philips Research Laboratories in Eindhoven and the FOM Institute AMOLF in Amsterdam (The Netherlands). InP nanowires comprising three different segments were synthesised in a low pressure (50 mbar) Aixtron 200 MOVPE reactor on InP (111)B substrates. Au colloids with a diameter of 100 nm were used to catalyse the growth. In order to minimise the lateral growth of the nanowire the growth temperature was set to 420 °C. The precursors trimethylindium (TMIn) and phosphine (PH<sub>3</sub>) were used for the intrinsic segments, at partial pressures of  $1.19 \times 10^{-3}$  and  $4.17 \times 10^{-1}$  mbar, respectively, in a total flow of 6 L/min hydrogen (H<sub>2</sub>) carrier gas. Additionally, hydrogen sulphide (H<sub>2</sub>S), at a partial pressure of  $4.17 \times 10^{-3}$  mbar was used as *n*-dopant for the doped segments. Before growth, an annealing step was carried out under PH<sub>3</sub>/H<sub>2</sub> atmosphere to desorb any surface oxide and to alloy the Au colloids with the InP substrate to ensure epitaxial growth. As initial segment (labeled C in Fig. 3.7) intrinsic InP was grown followed by an *n*-type segment (labeled B in Fig. 3.7) and another intrinsic segment (labeled A in Fig. 3.7). Due to the non-negligible lateral growth a thin *n*-doped shell and an intrinsic shell around the first intrinsic segment is found.

### Sample Preparation for s-SNOM Measurements

After synthesis, the nanowires are mechanically transferred onto an intrinsically doped Si substrate ( $\rho = 700 - 1300 \Omega\text{cm}$ ). For this, the wafer with InP nanowires grown on top is pressed against a Si substrate, and slid parallel to the interface, as illustrated schematically in Fig. 3.5. This way, the nanowires break almost at their base and stick to the Si substrate. In order to facilitate locating of a single and isolated InP nanowire with the s-SNOM, the Si wafer was patterned with an array of Au markers previous to

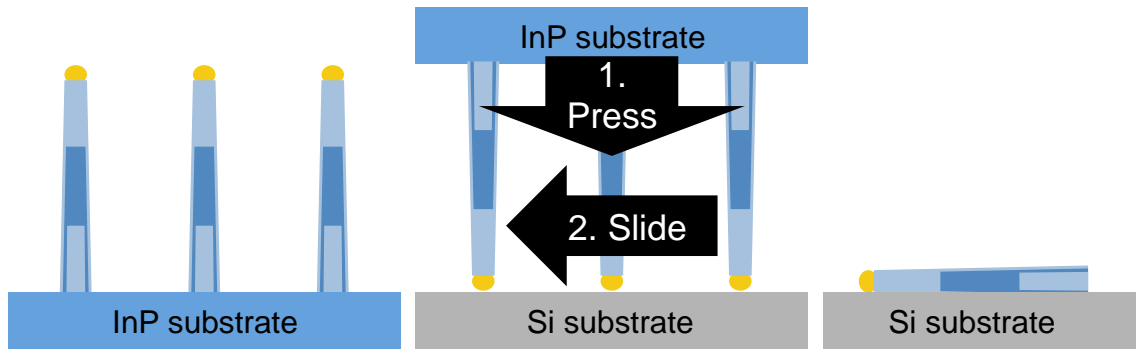


**Figure 3.5:** Schematics of transfer of InP nanowires from InP substrate to a Si wafer after VLS growth.

the nanowire transfer. The Au markers are prepared using a standard lift-off procedure at Philips Research Laboratories, Eindhoven (The Netherlands). Hereby, the Si wafer is first cleaned with fumed nitric acid. In a second step it is coated with a photo-resist, and using electron beam lithography (EBL) the photo-resist is exposed and developed. Next, a titanium adhesion layer is vapor-deposited, subsequently followed by a Au layer. In the final step, the remaining photo-resist is cleaned away using nitric acid. For our experiments nine arrays of Au markers with a spacing of  $20\ \mu\text{m}$  in between the markers were fabricated. To differentiate the different Au markers, they comprise a different and unique shape, allowing for an unambiguous identification. Each array, in turn, is made up by a square of  $11 \times 11$  markers (see Fig. 3.6a) and is labeled with unique number.

The pre-characterisation of the patterned Si wafer containing the InP nanowires using scanning electron microscopy (SEM) (see Fig. 3.6a-c) allows to scan large areas in order to find single nanowires. The high resolution of SEM hereby allows to find single wires, which is difficult by optical microscopy because the nanowires are partially smaller than  $100\ \text{nm}$  in thickness. After finding a single, isolated nanowire in SEM, the combination of the unique array number and the shape of the Au markers allows to directly locate this sample position in our s-SNOM using the built in optical microscopy (Fig. 3.6c).

Note, from our IR s-SNOM measurements of many different InP nanowires, we found that highly resolved ( $> 2000\times$  magnification) SEM imaging of the nanowires during the pre-characterisation might change the local conductive properties, due to the high electron beam energies and due to the deposition of a carbon contamination layer. Thus, for the SEM pre-characterisation a magnification lower than  $2000\times$  is optimal to find single nanowires without modifying the nanowires' optical properties. In case high-resolution images of a nanowire are needed in addition to the s-SNOM images,

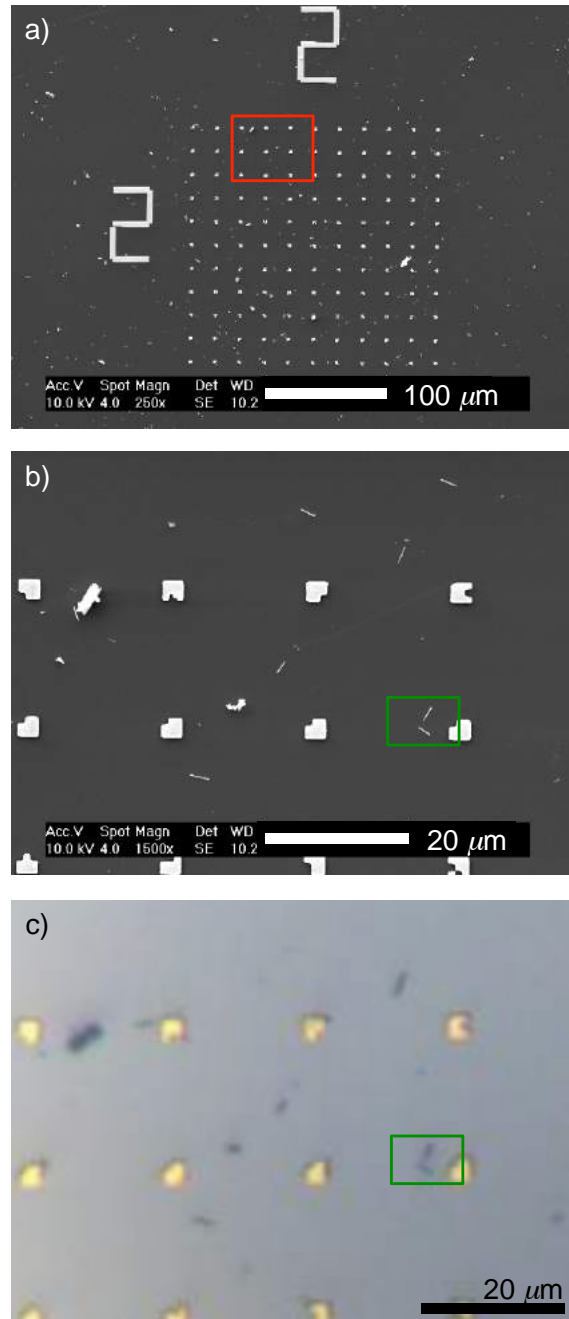


**Figure 3.6: SEM images of a Si wafer with Au markers.** (a) Overview image of one of the arrays on the Si wafer labeled by the numbers 2 - 2. Au markers for the orientation and the location of single InP nanowires can be seen. (b) Zoom-in into the region marked by the red square in Fig. 3.6a. Four individual Au markers can be seen, and between the two left markers an individual InP nanowire is visible. (c) Optical microscope image of the same sample region as shown in (b), taken with the optical microscope built into the NeaSNOM microscope.

SEM imaging has to be performed after the s-SNOM imaging.

### 3.4 Near-field Study of InP Nanowires

We begin our study of the free-carrier concentration in semiconductor nanowires by imaging two representative InP nanowires lying on a silicon (Si) wafer (see Fig. 3.7). For the IR s-SNOM imaging we employ conventional Pt-coated tips (apex radii  $\approx 20$  nm), which are illuminated by a focused laser CO<sub>2</sub> beam at a frequency of  $\omega = 893$  cm<sup>-1</sup>. For all experiments the tapping amplitude was set to 20 nm to 30 nm at a tapping frequency of  $\Omega \approx 300$  kHz. Second harmonic demodulation ( $n = 2$ ) was employed, yielding amplitude  $s_2$  (Fig. 3.7b) and phase  $\varphi_2$  images (Fig. 3.7c), simultaneously to topography (Fig. 3.7a).

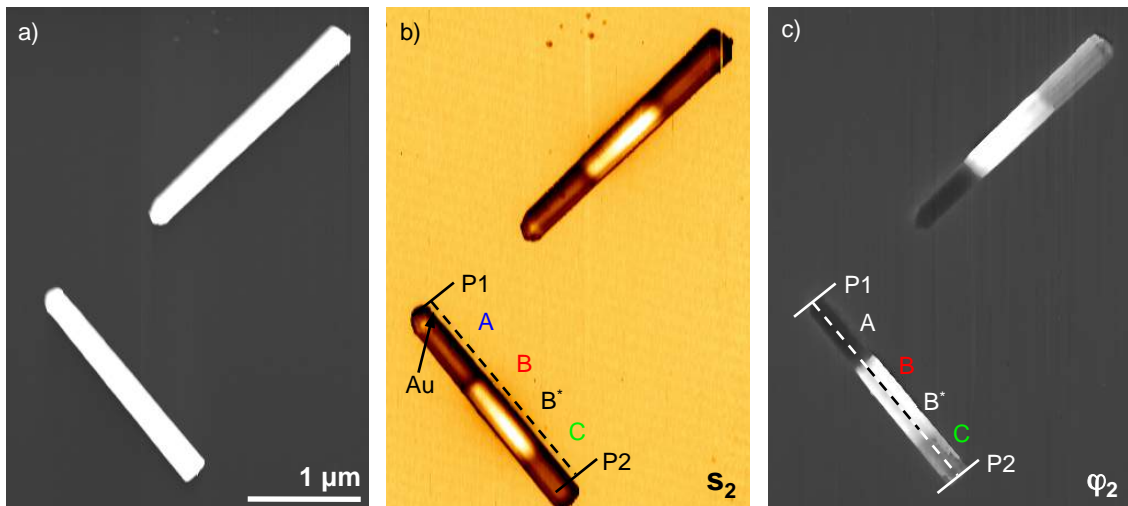


**Figure 3.7: Infrared near-field mapping of modulation doped InP nanowires.** Topography (a) and IR amplitude  $s_2$  (b) and phase  $\varphi_2$  (c) images of two representative InP nanowires recorded at an IR laser frequency of  $893$  cm<sup>-1</sup> ( $11.2$   $\mu$ m wavelength). For s-SNOM measurements the InP nanowires are adsorbed on a flat silicon surface.

Fig. 3.7a shows the topography of two InP wires and the simultaneously recorded IR amplitude  $s_2$  (Fig. 3.7b) and phase  $\varphi_2$  images (Fig. 3.7c) at a laser frequency of  $\omega = 893$  cm<sup>-1</sup>. While the topography image shows the uniform surface of the wires, the IR images clearly reveal the three different segments. Obviously, the IR amplitude and phase contrasts allow for distinguishing between the doped and undoped segments. Linescans (Figure 3.8a) showing the IR amplitude and phase along the axis of the right wire also reveal a clear material contrast between the Au particle and the undoped InP segment. In agreement with former s-SNOM studies, the metal exhibits

higher IR amplitudes than the undoped semiconductor material [30, 31]. From the sharp change of the amplitude signal at the Au/InP interface wire we can estimate a spatial resolution of about 25 nm.

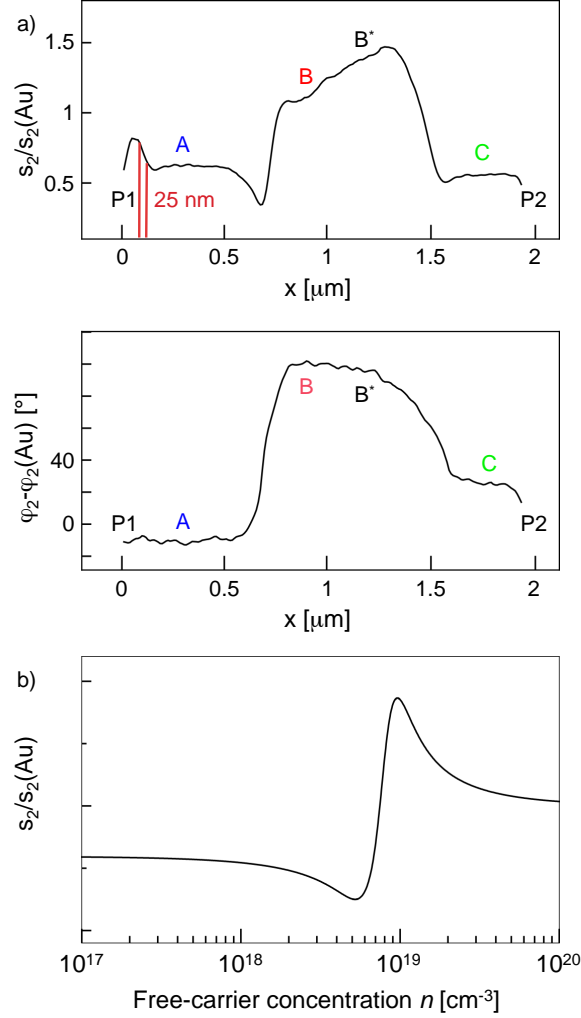


**Figure 3.8:** (a) IR amplitude  $s_2$  and phase  $\varphi_2$  along the axis of the right nanowire in Figure 3.7b, extracted between the two positions marked P1 and P2. The letters A-C mark the positions of the IR near-field spectra shown in Figures 3.9 and 3.10. (b) Calculated s-SNOM amplitude  $s_2$  of an InP sample with an increasing free-carrier concentration from  $10^{17}$  to  $10^{20}$  carriers/ $\text{cm}^{-3}$  at the fixed IR frequency of  $893 \text{ cm}^{-1}$  (corresponding to  $11.19 \mu\text{m}$  wavelength). The calculation was carried out employing the finite-dipole model [81, 92] and normalised to the s-SNOM signal of an Au sample.

To explain the experimentally measured near-field amplitude contrast in Fig. 3.7 and the line profile in Fig. 3.8a, we use the finite-dipole model (see chap. 2.3) to calculate the IR amplitude  $s_2$  as a function of the free-carrier concentration  $n$ . The calculation was performed for a fixed frequency of  $\omega = 893 \text{ cm}^{-1}$ , which was employed for recording the images shown in Figure 3.7. Figure 3.8b shows that with increasing  $n$  the calculated amplitude first exhibits a minimum at around  $n \approx 5 \times 10^{18} \text{ cm}^{-3}$ , followed by

### 3.5 Quantification of the Free-carrier Concentration by IR Near-field Spectroscopy 43

a maximum at about  $n \approx 10^{19} \text{ cm}^{-3}$ . As described in chapter 3.2, this resonance behaviour [30] arises from the near-field interaction between the probing tip and the free carriers (plasmons) in a highly doped semiconductor sample [26, 30]. Like for any resonance, the amplitude maximum is accompanied by a strong phase change. Indeed, this resonance behaviour is clearly seen in the experimental line-plot shown in Figure 3.8a. The significant amplitude minimum (around  $x = 0.7 \mu\text{m}$ ) directly reveals the existence of a free-carrier gradient between the undoped (A) and doped (B) segments, extending more than 200 nm along the nanowire axis, as we can estimate by comparing Figures 3.8a and b.

Intriguingly, in Figure 3.7c and Figure 3.8a we also observe a phase contrast between the undoped top segment (A) and the bottom segment (C), the latter consisting of an undoped core, but with an interior doped shell. The thickness of the doped shell can be estimated to be about 10 nm and is covered by an approximately 10 nm thick undoped shell (both thicknesses can be determined from the topography of the wire, showing a linear increase of the diameter from 100 nm to 140 nm). The successful detection of the doped subsurface shell has two important implications. It demonstrates that IR near-field microscopy enables noninvasive and nanoscale resolved free-carrier mapping inside a single nanowire heterostructure. Further, it provides direct experimental evidence that doping introduced during radial nanowire growth yields a large free-carrier concentration, *i.e.* local conductivity, which has important consequences for future device designs.

## 3.5 Quantification of the Free-carrier Concentration by IR Near-field Spectroscopy

To quantify the free-carrier concentration in the doped InP nanowire segment, we perform near-field spectroscopic mapping (as described in chap. 2.2) of the right nanowire in Figure 3.7 in the spectral range  $\omega = 890 - 1100 \text{ cm}^{-1}$ . Local amplitude and phase spectra taken at the top (A), middle (B) and bottom (C) segments are shown in Figure 3.9a. The spectra of the undoped top segment (position A in Figure 3.7, blue symbols) do not exhibit any spectral signature in both amplitude and phase. The doped core (position B in Figure 3.7, red symbols), in contrast, reveals a significant spectral signature. With increasing frequency we find a strong signal decrease in both the amplitude and phase. Applying the finite-dipole model (see chap. 2.3 and [92]), we can fit the experimental data. The free-carrier concentration  $n$  and free-carrier mobility

$\mu$  are used as fit parameters. Because of the flat spectral characteristics for the undoped segment (A) we can only estimate an upper limit for the doping concentration in this segment. We find a good agreement between experiment and calculation for  $n < 10^{18} \text{ cm}^{-3}$  (solid blue line). For the doped segment at position B, we obtain good agreement in both amplitude and phase for  $n = 7.6 \times 10^{18} \text{ cm}^{-3}$  and a mobility which is reduced by a factor of 0.45 with respect to the literature value for bulk InP (solid red line) [104, 105]. Possible reasons for the reduced mobility could be the wire geometry or the high-frequency (IR) measurement. For different bulk semiconductors [125] it has been reported that the mobility at IR frequencies can be significantly reduced compared to the direct-current (DC) mobility. Furthermore, radial variations in the free-carrier contribution - often observed in doped semiconductor nanowires [10, 98] - could broaden the near-field resonance. Thus, fitting the resonance would yield an averaged free-carrier concentration of the local volume probed by the near-field of the tip and a reduced mobility. A promising pathway to tackle this issue in the future could be the development of near-field tomography, which could allow for depth-resolved near-field mapping of local material properties [126, 127]. Nevertheless, the already demonstrated capability to retrieve free-carrier concentration and mobility with nanoscale spatial resolution promises s-SNOM to become a highly interesting tool not only for nanowire research.

We next study the IR near-field spectrum of the doped interior shell of the nanowires' bottom segment (Figure 3.9a, spectrum C displayed by green symbols). Interestingly, we find a clear signature in the phase spectrum. While both the spectral amplitude and phase contrasts are significantly reduced, the spectral feature appears in the same frequency range as for the doped core (middle segment, position B). We illustrate this finding by multiplying the phase spectrum B of the doped core with a factor of 0.3. The good agreement with the experimental phase spectrum C confirms the absence of a pronounced spectral shift between spectra B (doped core) and C (doped shell). Because the spectral position of the phase slope is determined by the free-carrier concentration  $n$  (see Figure 3.8 and grey curves in Figure 3.9a), we can conclude that the effective free-carrier concentration is similarly high as in the doped core. Considering that the dopant concentration in the shell can be expected to be higher than inside the core [10], this is an interesting observation. We explain this by the fact that the doped shell is clamped between the undoped core and the undoped outer shell. Because of the strong difference in concentration, free carriers diffuse towards the undoped regions. Therefore, the observed free-carrier concentration is lower than the chemically built-in dopant concentration. We note that the weaker spectral contrast in both amplitude

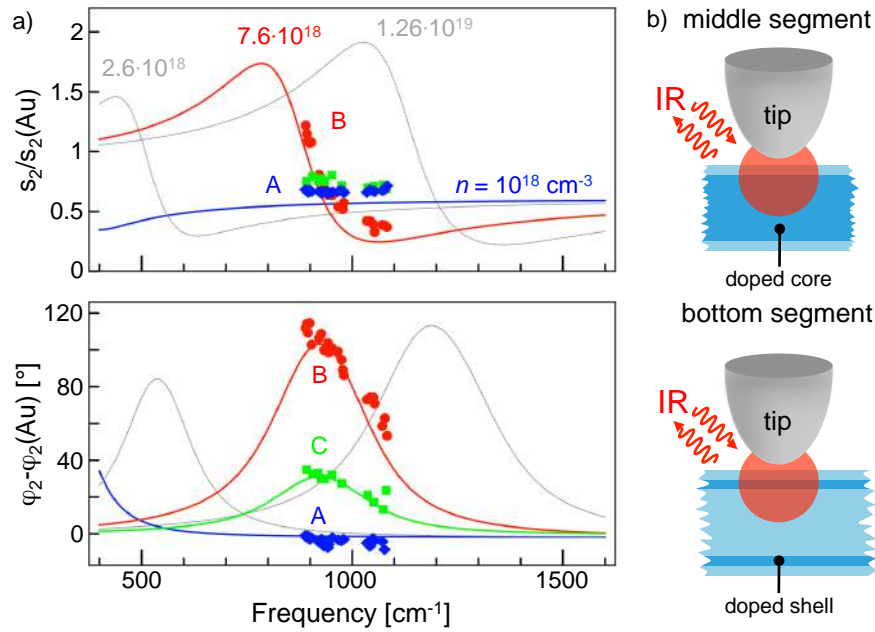


**Figure 3.9: Local IR near-field spectra of a single InP nanowire.** (a) The red and blue curves show amplitude and phase spectra taken at positions A (undoped InP) and B (doped InP core) marked in Figure 3.7a. The green curve C was taken at the centre of the bottom segment (doped InP shell) of an InP nanowire of the same nanowire sample. Both experimental (symbols) and theoretical (solid lines) amplitude  $s_2$  and phase  $\varphi_2$  spectra were normalised to the signal obtained on the Au particle. Numbers indicate the free-carrier concentration  $n$  used for the calculations. The grey curves show calculated spectra with increased and decreased free-carrier concentration ( $5 \cdot 10^{18} \text{ cm}^{-3}$ ) illustrating that changes in the range of 50% would yield large spectral shifts of several  $100 \text{ cm}^{-1}$ . (b) Schematic drawing of the s-SNOM probing the highly doped middle segment and the highly doped subsurface shell, respectively.

and phase can be explained by the reduced amount of doped material that is probed by the IR near-field at the tip apex (Figure 3.9b). The reduced spectral contrast is a typical observation when the near-field contrast of a thin layer is compared with a bulk sample of the same material [128].

We now study in more detail the amplitude signal  $s_2$  on the central segment, which clearly increases along the axial direction (Figure 3.8). Comparing the spectra taken at position B and B\* (Figure 3.10a), we find a slight shift of spectrum B\* towards higher frequencies. This corresponds to an increase of the free-carrier concentration of about  $\Delta n = 0.5 \cdot 10^{18} \text{ cm}^{-3}$  (6.6%). Evaluating local near-field spectra along the nanowire axis, we find a linearly increasing free-carrier concentration (Figure 3.10b). At first, this data evaluation highlights the powerful combination of high sensitivity and nanoscale spatial resolution provided by IR spectroscopic s-SNOM. Furthermore, it indicates that the local free-carrier concentration on the doped segment slightly increases with in-

creasing shell thickness. This could be explained by the higher dopant concentration in the shell compared to the core [10], yielding a higher number of dopants with increasing shell thickness.

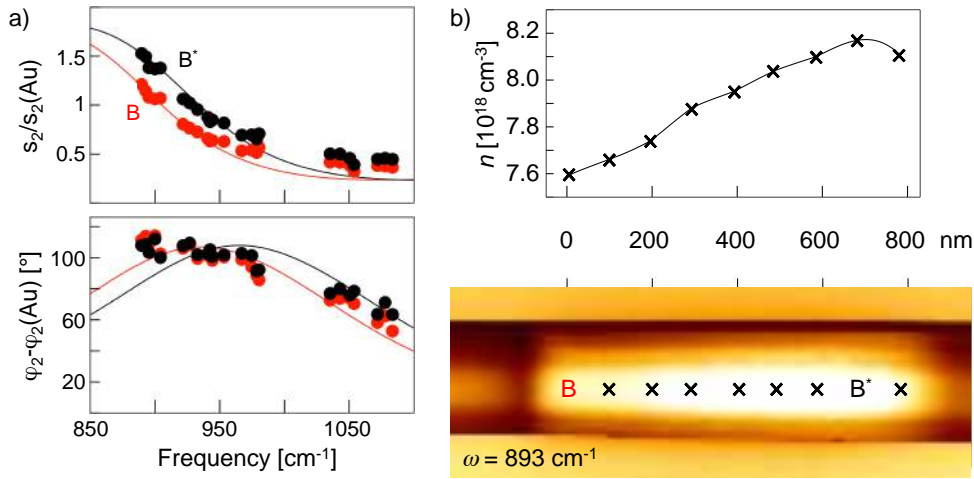


**Figure 3.10: Sensitivity of s-SNOM demonstrated on the highly doped middle segment.** (a) Near-field spectra of the central segment at positions B and B\*, revealing a slight difference in free-carrier concentration amounting to about  $\Delta n \approx 0.5 \cdot 10^{18} \text{ cm}^{-3}$ . (b) Measured free-carrier concentration along the central nanowire segment, shown together with a high-resolution IR image at  $893 \text{ cm}^{-1}$ . The data-points in Figure 3.10 have been calculated by finding the best agreement for amplitude and phase between the finite-dipole model calculation and the measured near-field spectra at each position.

### 3.6 Outlook

In order to demonstrate the great potential of s-SNOM to map local free-carriers even in thin semiconductor nanowires, we show in Fig. 3.11 s-SNOM images of modulation-doped InP nanowires with diameters as small as 20 nm. The thin nanowires were grown applying the same growth-protocol as the 100 nm wires presented in Figure 3.7, but using Au precursors with a smaller diameter. The IR images clearly reveal the doped segment. In contrast to the 100 nm wires, however, the doped segment is substantially shorter, owing to reduced axial growth speed in thin wires [114]. Furthermore, the doped segment exhibits strong signal variation in both IR amplitude and phase, which indicates a strongly inhomogeneous free-carrier distribution. We assign this finding to an increased defect density in thin wires [112, 129], but further systematic studies are certainly needed for an in-depth understanding of this observation.

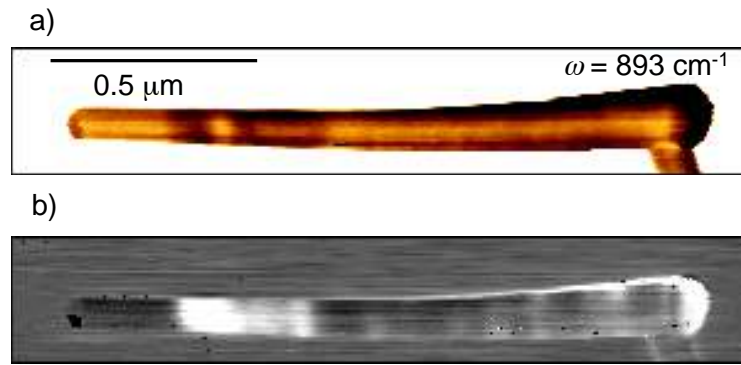


**Figure 3.11: Infrared near-field images of modulation doped InP nanowires with a thickness of 20 nm.** (a) Amplitude and (b) phase images recorded at a frequency of  $895\text{ cm}^{-1}$  ( $11.17\text{ }\mu\text{m}$  wavelength) of a representative nanowire, grown with the same procedure as the 100 nm InP wires.

### 3.7 Conclusion

In conclusion, we demonstrated the application of infrared near-field nanoscopy for highly sensitive and nanoscale resolved mapping of free carriers in doped semiconductor nanowires. We showed that the method allows for the measurement of local carrier concentration and mobility in these nanowires. Sensitivity to lower free-carrier concentrations can be achieved by spectral extension [130] of s-SNOM to terahertz frequencies [31]. In case of three-dimensional free-carrier distributions, *i.e.* both axial and radial variations of the carrier density, future quantitative measurements will require systematic studies and improved modeling of subsurface near-field mapping [131] and depth resolution in s-SNOM. The implementation of near-field optical tomography - recently predicted to provide three-dimensional information about the local dielectric properties [127] - could open the door to non-invasive mapping of the three-dimensional distribution of both the free-carrier concentration and mobility, not only in complex nanowire heterostructures but also in single nanoparticles and nanodevices.



# 4

## **Correlative Infrared-electron Nanoscopy Applied to Zinc Oxide Nanowires**

*In this chapter we introduce correlative infrared-electron nanoscopy, a novel method yielding transmission electron microscope (TEM) and infrared (IR) near-field images of one and the same nanostructure. While TEM provides structural information down to the atomic level, the IR images yield nanoscale maps of chemical composition and conductivity. We demonstrate the application potential of the method by studying the relation between conductivity and crystal structure in cross-sections of chemically grown ZnO nanowires. The unique combination of IR conductivity maps and the local crystal structure reveals a radial free-carrier gradient, which inversely correlates to the density of extended crystalline defects. Our results open new avenues for studying the local interplay between structure, conductivity, and chemical composition in widely different material systems, ranging from correlated and low-dimensional electron systems to biomedical tissue.*

## 4.1 Introduction

In the previous chapter we have seen that IR s-SNOM spectroscopy is a powerful tool to visualise and quantify the free-carrier concentration in semiconductor nanowires. The enormous sensitivity of IR s-SNOM allowed even to visualise variations in the free-carrier concentration of only  $0.5 \times 10^{18} \text{ cm}^{-3}$  (see Fig. 3.10) and inhomogeneities within the 20 nm thick nanowires. Despite the intriguing capabilities of s-SNOM to visualise the free-carrier concentration, the origin of the variations in the free-carrier concentration might be difficult to explain. Hence, for a more comprehensive understanding of functional materials and complex devices, it is necessary to correlate the physical and chemical properties obtained from different imaging techniques.

In materials research and bio-sciences, for example, correlative light-electron microscopy is a well-established and brilliant technique providing unique insights into the relationship between the local structure and the function of semiconductor nanowires [132, 133, 134, 135, 136, 137, 138] and biological matter [139, 140], respectively. In this chapter we introduce a special sample preparation routine, employing a focused ion beam (FIB) to prepare a thin lamella that allows to combine TEM imaging and nanoscale resolved IR s-SNOM imaging of *one and the same* nanoscaled sample. To demonstrate an application example of high technological relevance, we study the widely unexplored relation between local crystal structure and local conductivity (*i.e.* the free-carrier concentration and the mobility) in chemically grown ZnO nanowires.

ZnO nanowire arrays have a high application potential in different technological domains such as (opto-)electronics, solar cells and piezoelectrics, and have thus attracted great interest among emerging nanoscale materials [141, 142, 143]. This interest stems from their unique combination of a peculiar morphology and (opto-)electronic properties. Apart from costly and technologically complicated vapor growth processes, arrays of ZnO single-crystal nanowires can be grown by low-temperature and cost-effective techniques such as hydrothermal [144, 145] and electrochemical [146] deposition. Therefore, low-temperature grown ZnO nanowires arrays are an ideal candidate for large-scale production allowing the nanowire integration into devices using low-cost thin-film technology. These nanowires, however, exhibit a high density of defects, and experiments have shown that annealing can improve the performance of the nanowires in several applications. While previous TEM studies have revealed a significant amount of defects in ZnO nanowires [141, 144, 147], information about their influence on the local conductivity has remained elusive. Notwithstanding, it is this very information that is of utmost importance for the optimisation of the growth

process, and consequently, for the performance of the nanowires. Electrochemically grown ZnO nanowires thus can serve as an interesting application example for demonstrating infrared-electron correlation nanoscopy.

## 4.2 Sample Fabrication

For this study different ZnO nanowire samples comprising as-deposited and annealed nanowires have been prepared by R. Tena Zaera at Cidetec, San Sebastian (Spain). We use both arrays of nanowires in a application like devices, as well as single isolated nanowires. The former allows us to obtain some statistical information by looking at a larger number of nanowires by s-SNOM only, whereas the latter were used to correlate s-SNOM and TEM images. In this paragraph the most important steps of the sample preparation will be briefly explained.

### Electrodeposition of ZnO Nanowire Arrays

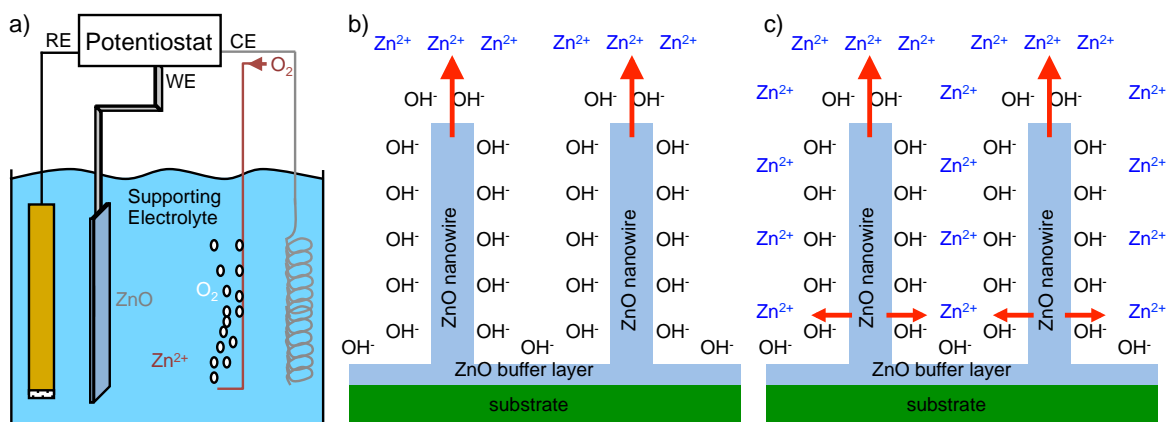


**Figure 4.1: Schematics of the electrochemical growth of ZnO nanowires.** (a) Three-electrode electrochemical setup. CE labels the counter electrode, WE is the working electrode, and RE the reference electrode. (b) Illustration of longitudinal ZnO nanowire growth, which takes place if the  $O_2$  reduction is faster than the  $Zn^{2+}$  diffusion [148]. (c) Illustration of longitudinal and lateral nanowire wire growth, under the condition that the  $O_2$  reduction rate is similar to the  $Zn^{2+}$  diffusion rate [149]. Schematics adopted from R. Tena Zaera, Cidetec (Spain).

ZnO nanowire arrays were electrodeposited from the reduction of dissolved molecular oxygen in zinc chloride aqueous solutions [149, 150]. The electrodeposition experiment was performed in a three-electrode electrochemical setup (see Fig. 4.1a) employing a VMP3 BioLogic-Science Multichannel Workstation. The cathode was a commercial

conducting glass/SnO<sub>2</sub>:F (TEC15, Hartford Glass Co) substrate. A Pt spiral wire was used as the anode and a Saturated Calomel Electrode (SCE) as the reference electrode. The electrolyte was a  $5 \times 10^{-4}$  M ZnCl<sub>2</sub> (>98.0 %), 3.4 M KCl (>99.5 %) ultrapure aqueous solution, saturated with bubbling oxygen. The electrodeposition was performed at 80 °C under constant potential ( $V \sim -1.0$  V vs. Saturated Calomel Electrode). By controlling the ratio between O<sub>2</sub> reduction rate Zn<sup>2+</sup> diffusion rate the thickness of the nanowires can be controlled, as outlined in Fig. 4.1b and c. Under growth conditions where the O<sub>2</sub> reduction rate is faster than the Zn<sup>2+</sup> diffusion only longitudinal nanowire growth takes place [148]. When the O<sub>2</sub> reduction rate is similar to the Zn<sup>2+</sup> diffusion, additional lateral growth takes place resulting in thicker nanowires. Fig. 4.2 shows a SEM image of a cross-section obtained by cleaving of a typical nanowire sample.

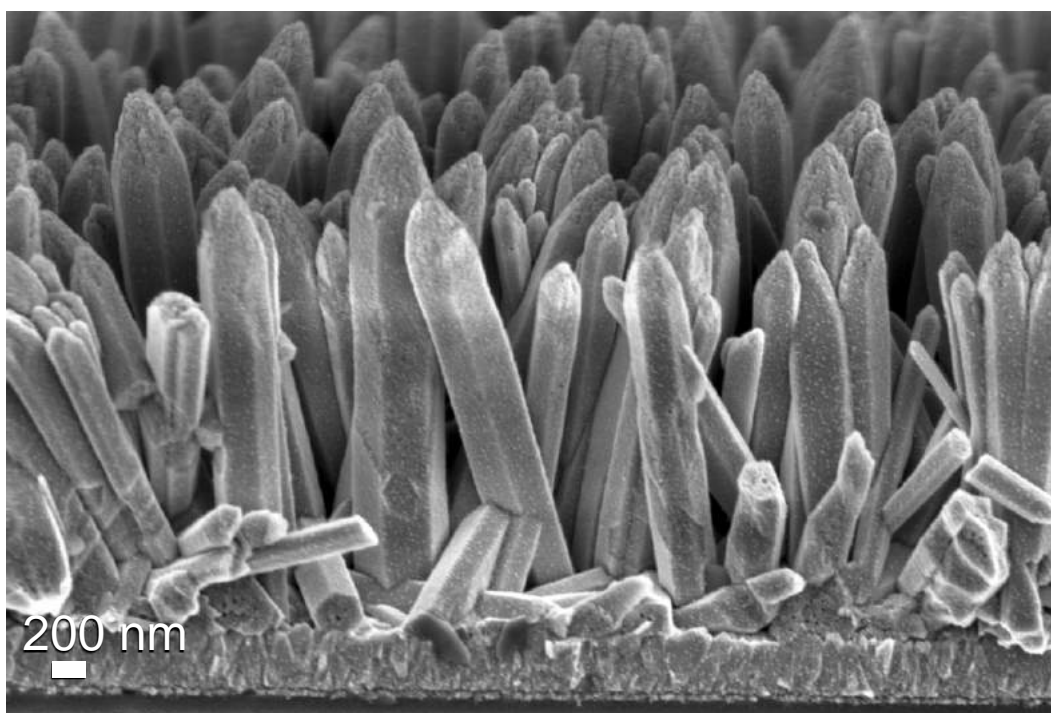


**Figure 4.2:** Scanning electron microscope (SEM) image of a cross-section of annealed ZnO nanowires grown on a glass substrate obtained by cleaving. Image courtesy of R. Tena Zaera, Cidetec (Spain).

### Annealing of ZnO Nanowires

To study the influence of annealing onto the crystal structure and the conductive properties of the ZnO nanowires, part of the nanowires were annealed after growth in an open horizontal tubular furnace. The ZnO nanowires arrays were air annealed at 450 °C during 1 hour.

### Embedding of ZnO Nanowires into a CuSCN Matrix

The above mentioned electrochemical growth results in arrays of free-standing ZnO nanowires. As we want to study cross-sections of the ZnO nanowires, which will be prepared by mechanically polishing the nanowires from the top end, it is necessary to fill up the free space in between the nanowires previous to polishing procedure. Therefore, we embedded as-deposited and annealed nanowires into a copper thiocyanate (CuSCN) matrix - a typical configuration in light emitting diode (LED) applications [142, 151]. The CuSCN matrix was deposited from a saturated solution of CuSCN in propyl sulphide [152] onto the ZnO nanowire array sample, which where preheated to  $\sim 80^\circ\text{C}$ . In Fig. 4.3 a SEM top view image of a ZnO nanowire array sample after CuSCN deposition is shown.

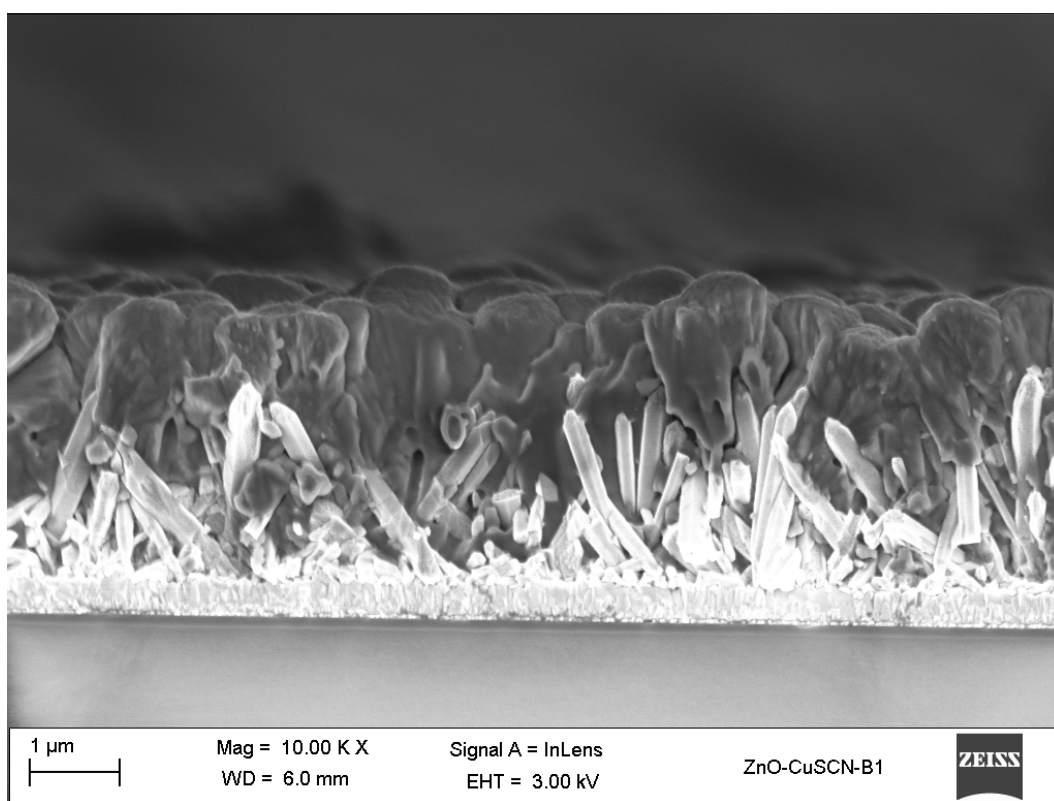


**Figure 4.3:** Scanning electron microscope (SEM) top view image of ZnO nanowires embedded into a CuSCN matrix. Image courtesy of R. Tena Zaera, Cidetec (Spain).

### Mechanical Polishing of ZnO Nanowires Embedded into a CuSCN Matrix

Cross-sections of as-deposited as well as annealed nanowire arrays embedded into the CuSCN matrix were prepared by mechanical polishing following a standard TEM wedge preparation procedure. Using a MultiPrep<sup>TM</sup> precision polishing system from

Allied High Tech Products, Inc. the nanowire samples were polished in a three step process. In a first step, a 1  $\mu\text{m}$  diamond film was used for a rough polishing with a wedge angle of about  $2^\circ$  to  $4^\circ$ . In a second step, fine polishing at a lower angle of about  $1^\circ$  to  $2^\circ$  was carried out. For the final polishing a Red Final C (Allied High Tech Products, Inc.) polishing cloth was used together with 0.05  $\mu\text{m}$  non-crystallising colloidal silica solution. The resulting samples show a surface roughness in the order of 40 nm as can be seen from AFM topography images. Fig. 4.4 shows a schematic illustration of mechanically polished ZnO nanowires embedded into a CuSCN matrix.

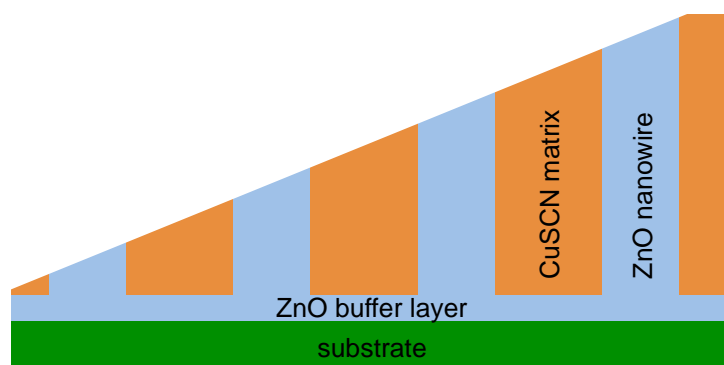


**Figure 4.4:** Schematics explaining the idea of the mechanical polishing of ZnO nanowire arrays embedded into a CuSCN matrix.

### 4.3 s-SNOM Study of Mechanically Polished ZnO Nanowire Arrays

As a first step in our study of the conductive properties of ZnO nanowires, we first pre-characterise the nanowires by s-SNOM. To that end we prepared mechanically polished cross-sections of electrochemically grown as-deposited (Figs. 4.5a) and annealed (Figs. 4.5b) ZnO nanowires as described in chapter 4.2. IR near-field imaging was performed with a commercial s-SNOM (NeaSNOM from Neaspec GmbH (<http://www.neaspec.com>), described in chapter 2.2) employing a metalized AFM tip for simultaneous topography and near-field mapping. The topography images (Fig. 4.5, upper row) clearly reveal the hexagonal shape of the nanowires, which were polished less than the surrounding CuSCN matrix owing to their different mechanical hardness, and giving rise to above mentioned surface roughness of a couple a few tenths of nanometers. For IR near-field imaging the tip is illuminated with the focused beam of a CO<sub>2</sub> laser (wavelength  $\lambda = 10.74 \mu\text{m}$ ). By interferometric detection of the scattered light we obtain nanoscale resolved IR amplitude and phase images. In both of them,

the as-deposited nanowires exhibit a bright ring (Fig. 4.5a), which vanishes completely after annealing (Fig. 4.5b) at 450 °C. From previous s-SNOM studies [22, 24, 153] it is well known that a simultaneous amplitude and phase contrast reveals a resonant near-field excitation in the sample. In doped semiconductors it typically stems from the resonant excitation of collective free-carrier oscillations (plasmons), which at mid-IR frequencies requires a free-carrier concentration in the order of  $10^{19}$  carriers/cm<sup>3</sup>. We thus conclude that the bright ring reveals a rather high free-carrier concentration, which significantly is reduced by annealing.

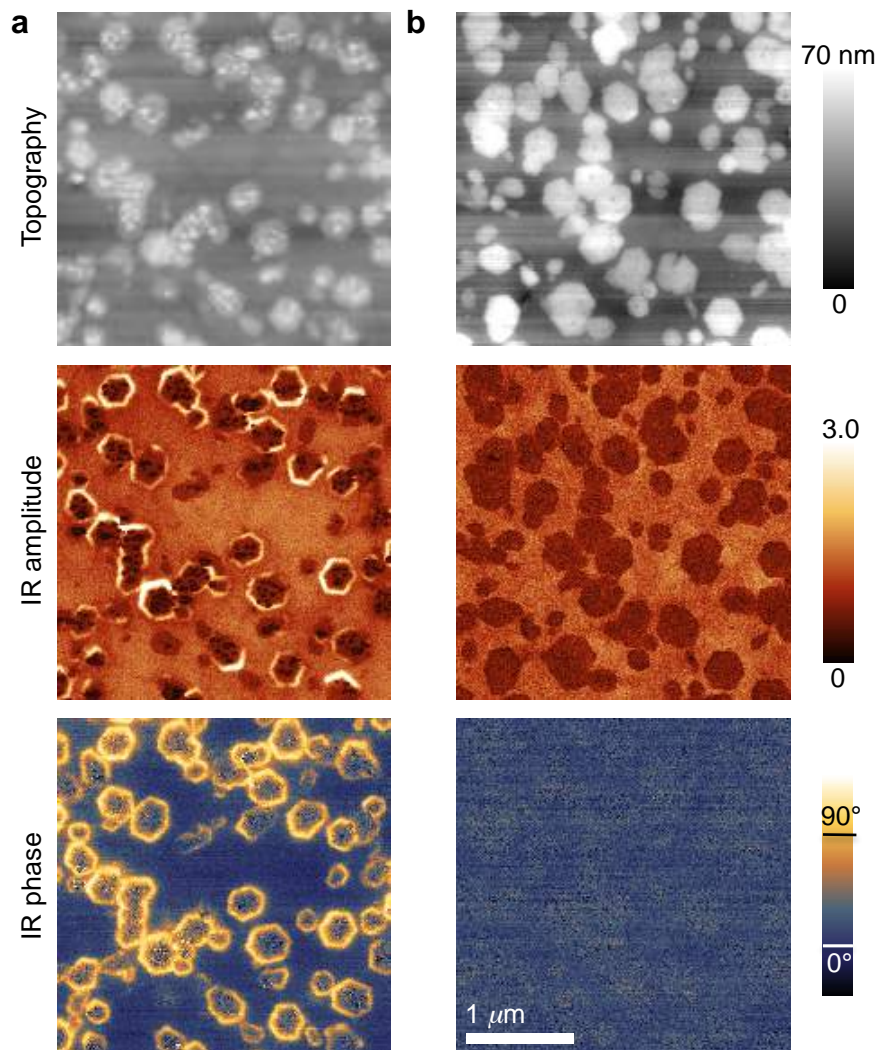


**Figure 4.5: s-SNOM images of mechanically polished ZnO nanowire samples.** Topography, IR amplitude and phase images of as-deposited (a) and annealed (b) ZnO nanowires embedded into a CuSCN-matrix.

In order to corroborate our conclusion and to quantify the local conductivity, we employed the finite-dipole model of s-SNOM (as described in chapter 2.3 on page 27) for calculating the IR near-field amplitude and phase contrast of ZnO as a function

of the free-carrier concentration  $n$  and mobility  $\mu$ , analogous to our previous studies of InP nanowires (see chapter 3). The finite-dipole model derives the amplitude and phase of the scattered IR light from the near-field interaction between the tip and the sample, the latter being described by its dielectric function found in literature [154]. The free-carriers are taken into account by adding a Drude-term characterised by  $n$ ,  $\mu$  and the effective carrier (*i.e.* electron) mass. Comparing the experimental amplitude and phase images with the calculations, we find for the bright outer ring of the as-deposited nanowires a free-carrier concentration of  $n \approx 4.3 \times 10^{19}$  carriers/cm<sup>3</sup> and an IR mobility of  $7.6 \text{ cm}^2\text{V}^{-1}\text{s}^{-1}$ .

For illustration of the concentration-dependent IR contrasts of ZnO we show the calculated IR near-field amplitude (solid red line in Fig. 4.6a) and phase (solid blue line in Fig. 4.6b) as a function of the free-carrier concentration  $n$  for the fixed illumination wavelength of  $\lambda = 10.74 \mu\text{m}$  and the mobility  $\mu = 7.6 \text{ cm}^2\text{V}^{-1}\text{s}^{-1}$  normalised to the near-field amplitude and phase values obtained for the CuSCN matrix. We see that with increasing  $n$  both the IR near-field amplitude and phase increase. The phase exhibits a characteristic maximum at about  $10^{19}$  carriers/cm<sup>3</sup>, indicating the near-field induced plasmon resonance. From the intersection of the calculated graphs and the experimental values (horizontal dashed lines) the free-carrier concentration is determined. In the core of the as-deposited nanowire, the low IR amplitude and the absence of an IR phase contrast between the core and the matrix can be explained either by a free-carrier concentration lower than  $n = 10^{18}$  carriers/cm<sup>3</sup> or by a dramatically reduced electron mobility. The latter can be seen from calculations where the free-carrier mobility was reduced by factors of 2 and 20, respectively (see grey curves in Figs. 4.6a,b). While our values confirm previous free-carrier concentration estimates from electrochemical measurements [155], the images visualise directly, and for the first time, the dramatically inhomogeneous, radial conductivity profile ( $\sim n \cdot \mu$ ) in single-step grown and unintentionally doped ZnO nanowires. This observation thus reveals a significant difference to the commonly assumed homogeneous and direct electrical pathway in single-crystalline ZnO nanowires.

The calculations of Figs. 4.6a and b also help to understand the IR contrast of the nanowires after annealing. The considerably decreased amplitude signal on the shell together with the vanishing phase contrast between the nanowire shell and the matrix can be either explained by a decreasing free-carrier concentration (lower than  $10^{18}$  carriers/cm<sup>3</sup>) or by a dramatic reduction of the free-carrier mobility (see grey curves in Figs. 4.6a,b). Because the free-carrier mobility in semiconductors typically increases upon annealing, we can conclude that the free-carrier concentration in the

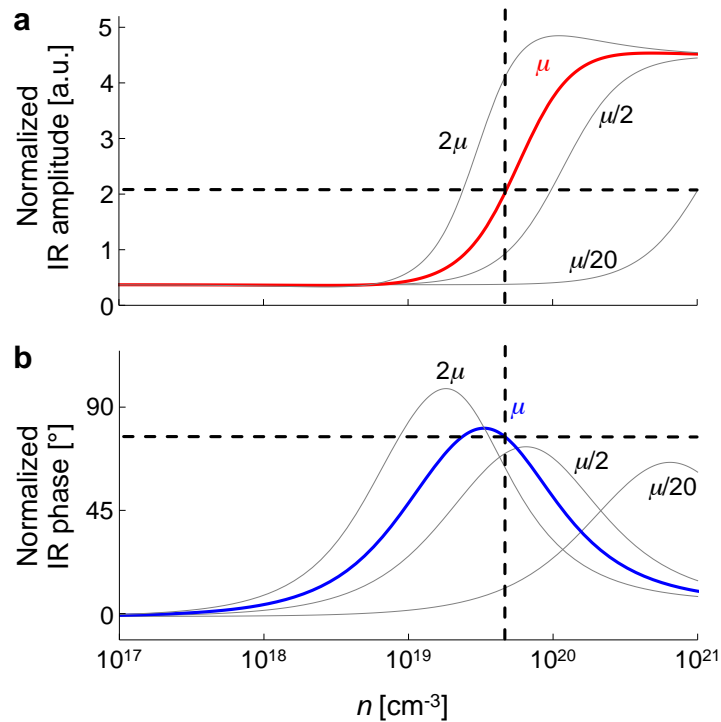


**Figure 4.6:** Calculations of s-SNOM amplitude (a) and phase (b) signal for a mobility of  $7.6 \text{ cm}^2\text{V}^{-1}\text{s}^{-1}$  and a fixed wavelength of  $10.74 \mu\text{m}$  are shown as a function of the free-carrier concentration  $n$ . Experimental values are depicted by horizontal dashed lines. The calculations were carried out using the finite-dipole model. Both experimental and theoretical values are normalised to CuSCN matrix. The grey lines show calculations where the mobility was enhanced by factor of 2, respectively reduced by factors of 2 and 20.

nanowire shell has decreased.

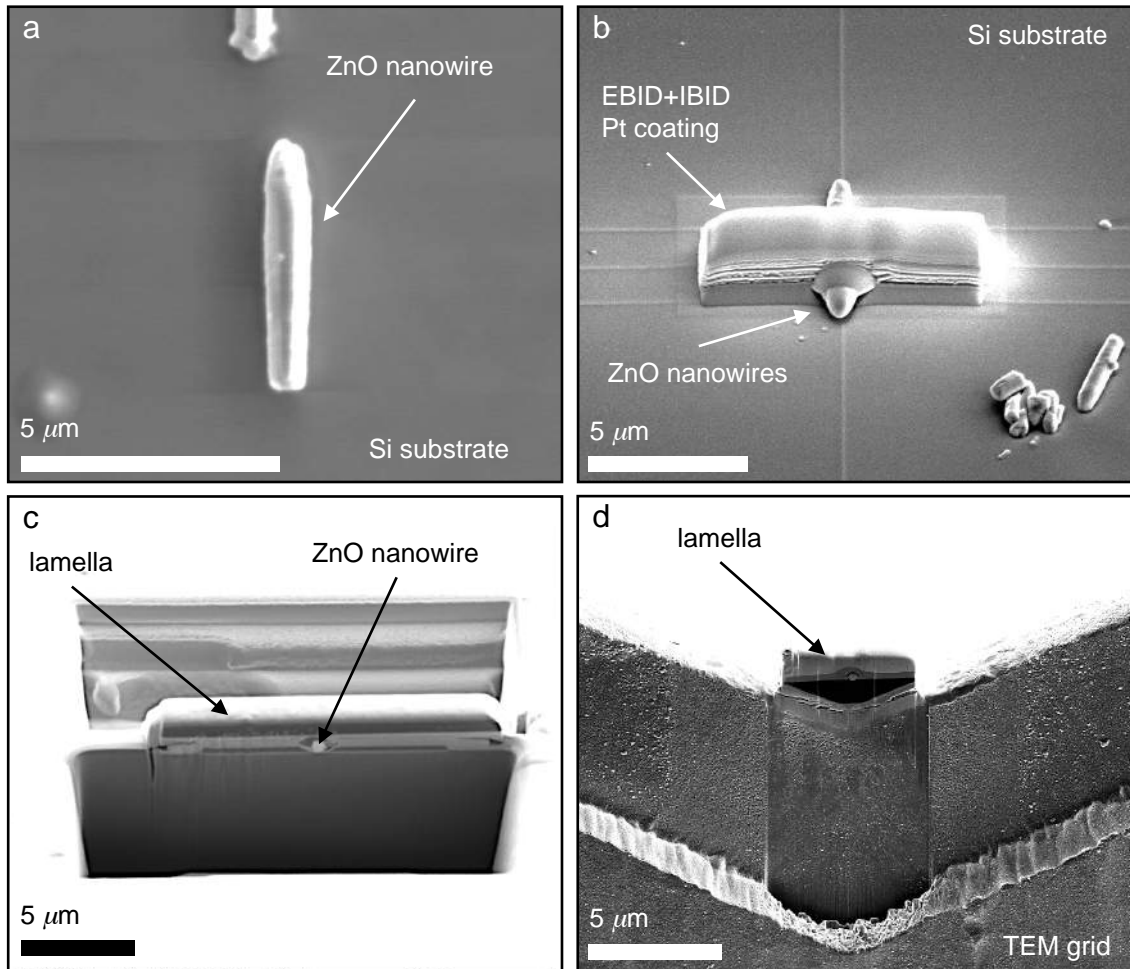
## 4.4 Correlative Infrared-electron Nanoscopy of Single Nanowires

In order to explore the relation between free-carriers density and local crystal structure, we first introduce correlative infrared-electron nanoscopy. This is motivated by the strong IR contrast variation between different nanowires in the mechanically polished sample shown in Fig. 4.5, which requires IR and TEM images of one and the same nanowire cross-section to obtain unambiguous conclusions. A suitable sample can be obtained by using Focused-Ion-Beam (FIB) sample preparation of a nanowire lamella. First, ZnO nanowires are mechanically transferred onto a Si substrate, using the same transfer procedure as described earlier for the InP nanowires (see section

3.3). Subsequently, the ZnO nanowires on top of the Si wafer are sputter-coated by an metal oxide (*e.g.* Al<sub>2</sub>O<sub>3</sub> or MgO) layer in order to protect them from electron and ion-beam induced crystal damage and possible implantation. Following our particular FIB protocol for TEM sample preparation, a thick ( $\sim 2\ \mu\text{m}$ ) lamella containing a cross-section of the ZnO nanowire has been prepared by A. Chuvilin from the Electron Microscopy Laboratory at CIC nanoGUNE, San Sebastian (Spain). As a first step of this protocol the nanowires are sputter-coated with a metal oxide (Al<sub>2</sub>O<sub>3</sub> or MgO) protection layer (done by O. Idigoras at CIC nanoGUNE, San Sebastian (Spain)), as shown in Fig. 4.7a. Then electron and ion beam induced deposition (EBID respectively IBID) of Pt is used to grow a second protection layer on top of a selected nanowire (Fig. 4.7b). The platinum layer increases the area around the nanowire, which facilitates the s-SNOM imaging of the nanowire cross-section after the final lamella fabrication. In the next step, FIB milling is used to prepare a TEM lamella containing the nanowire cross-section (Fig. 4.7c). After this, the lamella is transferred to one of the M-shaped sites of an Omniprobe 3 post TEM grid using an Omniprobe Nanomanipulator. Then the lamella is fixed seamlessly to the grid using IBID-Pt deposition (Fig. 4.7d). The seamless attachment of the lamella increases the area for approaching the scanning probe tip to the lamella and thus simplifies s-SNOM imaging. After s-SNOM imaging the lamella is thinned by FIB milling to electron transparency from the backside. Then it is fine polished with an ion beam of 5 keV energy from both sides to remove the amorphous surface-layer.

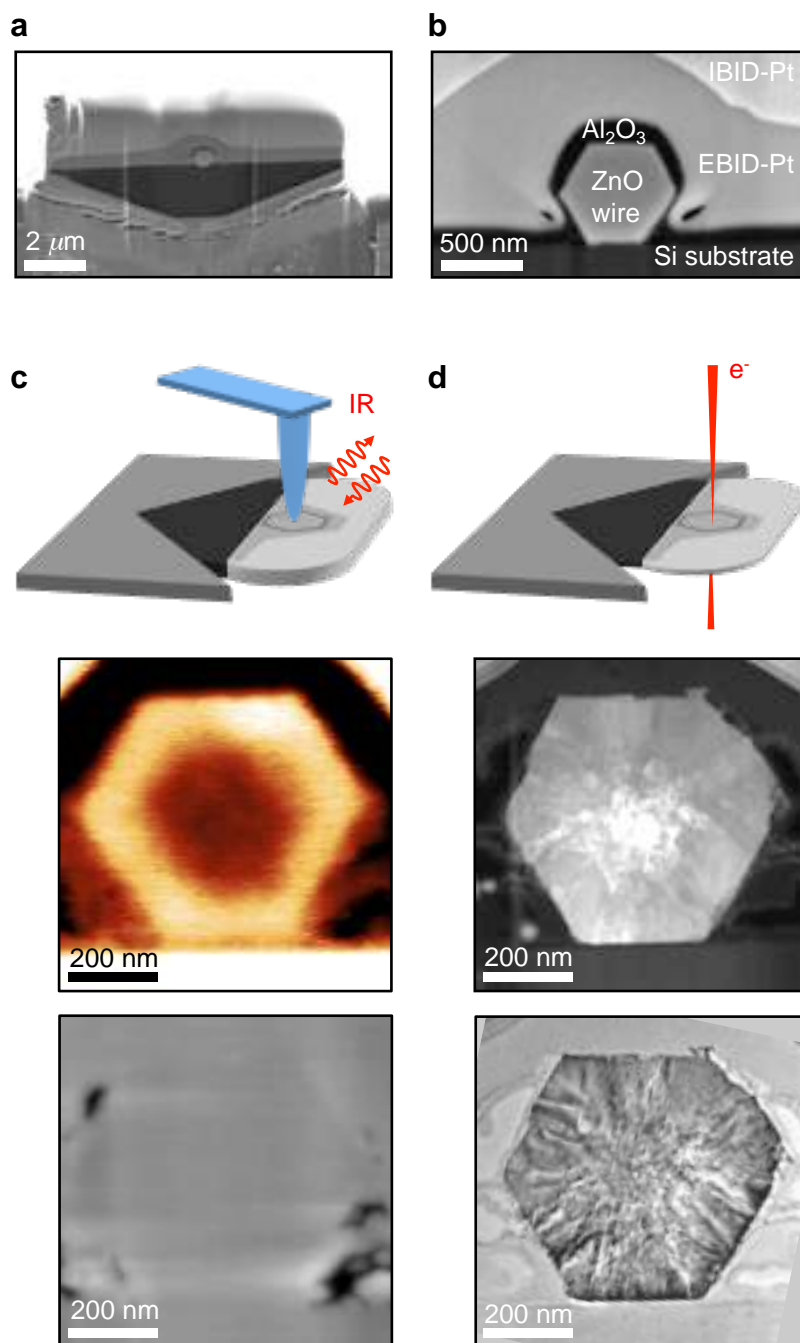
Fig. 4.8a shows a scanning electron microscopy (SEM) image of the lamella attached to a TEM grid. The hexagonal ZnO nanowire cross-section is clearly visible in between the Si substrate and the Al<sub>2</sub>O<sub>3</sub> coating (Fig. 4.8b). The lamella is first imaged with IR s-SNOM (Fig. 4.8c) and then thinned from the backside to 20 nm to 50 nm in order to enable high-resolution TEM and scanning TEM (HRTEM and STEM, respectively) imaging,(Fig. 4.8d). Both (HR)TEM and STEM imaging were performed by A. Chuvilin at CIC nanoGUNE, San Sebastian (Spain).

Fig. 4.8c shows the IR near-field amplitude and topography images, respectively, of a representative cross-section of an as-deposited ZnO nanowire. The topography reveals the smooth surface of the lamella with only a few holes (which were formed during the EBID-Pt deposition), while the IR images exhibit strong material contrasts between the Al<sub>2</sub>O<sub>3</sub> layer, the Pt coating and the Si substrate. Because of the low near-field signal of Al<sub>2</sub>O<sub>3</sub>, we can readily recognise the hexagonal ZnO nanowire. Most importantly, we clearly see that the nanowires exhibit a bright ring surrounding a dark core, resembling the general observations made in Fig.4.5a. This finding val-



**Figure 4.7: Sample preparation for correlative IR-electron nanoscopy.** a) Two nanowires after mechanical transfer to Si substrate and coating with  $\text{Al}_2\text{O}_3$ . b) ZnO nanowire after EBID and IBID Pt-coating. c) Fabrication of a lamella containing a nanowire cross-section. d) TEM lamella attached to a M-shaped copper TEM grid. Note that the images are taken from different nanowires.

indicates that FIB milling does not alter the free-carrier concentration and distribution significantly. Thus, FIB milling is an appropriate method for the preparation of samples for correlative infrared-electron nanoscopy (see 4.5 for a detailed discussion of a possible influence of the sample preparation on the IR image contrast). After s-SNOM, we perform ADF STEM (annual dark field STEM) and TEM (Titan 80-300 G2, FEI, Netherlands) imaging of the same nanowire cross-section (Fig. 4.8d). Interestingly, the ADF STEM image (Fig. 4.8d bottom) exhibits a strong contrast between the core and the outer region of the nanowire, although a detailed analysis (see below) shows that the nanowire is mono-crystalline over the whole cross-section. The ADF STEM contrast arises from a high density of nanopores and grain boundaries (see Fig. 4.9) in the core of the nanowire. This observation together with previous knowledge [147] let us conclude that the fast growth in axial direction is the major cause of defects, while



**Figure 4.8: Correlative infrared-electron nanoscopy of individual ZnO nanowire cross-sections.** (a) SEM image of a FIB prepared lamella that contains a single ZnO nanowire. (b) Zoom-in SEM image of the nanowire cross-section. (c) Top: Illustration of s-SNOM imaging of the lamella. Bottom: IR amplitude and topography image of the nanowire cross-section. (d) Top: Illustration of (S)TEM imaging of the lamella. Bottom: STEM and HRTEM image of the nanowire cross-section.

the relatively slow shell growth in radial direction allows the formation of an almost defect-free outer shell. More importantly, by comparing both IR s-SNOM and (S)TEM

images, we can establish a clear correlation between the local free-carrier concentration and local crystal structure: regions of better crystallinity in as-deposited nanowire exhibit a higher free-carrier concentration.

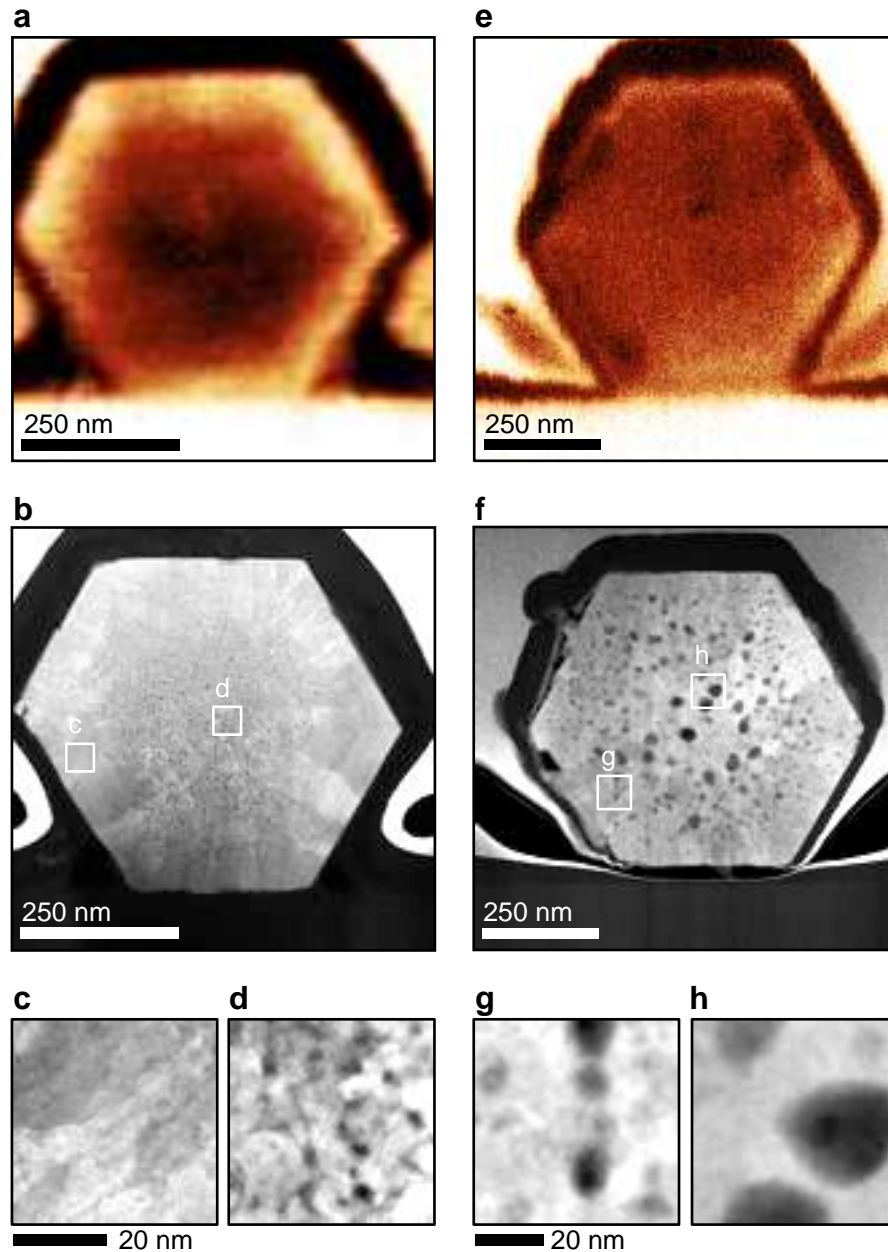


**Figure 4.9: Visualisation of the structure - conductivity relation in ZnO nanowires by infrared-electron nanoscopy.** (a,b) IR near-field amplitude and STEM images of an as-deposited ZnO nanowire. (c,d) High-resolution STEM images of regions marked in b). (e,f) IR near-field amplitude and STEM images of an annealed ZnO nanowire. (g,h) High-resolution STEM images of regions marked in f). The nanowire cross-sections were prepared and imaged as described in Fig. 4.8.

To trace the effect of annealing, we compare cross-sections of as-deposited (Figs. 4.9a-d) and annealed (Figs. 4.9e-h) ZnO nanowires. As before in Fig. 4.5, the radial free carrier

(conductivity) contrast in the s-SNOM images of the as-deposited nanowires (bright ring in Fig. 4.9a) vanishes after annealing (Fig. 4.9e), *i.e.* the s-SNOM signal in the nanowire shell decreases. Inside the core, the s-SNOM contrast relative to the Si substrate remains nearly unchanged upon annealing. HRTEM images of the same cross-sections (shown in Fig. 4.10) confirm the mono-crystalline structure of both nanowires. However, the as-deposited nanowire exhibits nanopores and 5 nm to 20 nm size grains in its core and a few defects in its shell, as seen in the enlarged high-angular ADF STEM (HAADF STEM) images (Figs. 4.9c,d). After annealing, we observe large voids in the HAADF STEM images (Figs. 4.9f-h) with diameters up to 50 nm. The size of the voids decreases in the direction of the nanowire surface. From these HAADF STEM images we conclude that by annealing the large crystal defects (nanopores and grain boundaries) inside the core are transformed into large voids, as seen previously for thin ZnO films [156]. Within the shell region, the crystal structure remains nearly unchanged upon annealing (apart from the void formation) (see HRTEM images in Figs. 4.10a and c).

## 4.5 Discussion

### Discussion of the Infrared-electron Nanoscopy Results

The correlation of both IR and (S)TEM images yields interesting insights into the local structure-conductivity relationship of the nanowires. The bright ring in the s-SNOM images of the as-deposited nanowire (Fig. 4.5a and Fig. 4.9a) reveals a large amount of free-carriers (high conductivity) in the shell region, which due to the nearly perfect crystal structure we can assign to point defects (vacancies, interstitials, and extrinsic dopants such as hydrogen, acting as free-carrier donors, but not seen in (S)TEM). The low conductivity (low IR signal) in the core of the as-deposited nanowire (Fig. 4.5a and Fig. 4.9a) we can explain either by a lower free-carrier concentration due to trapping of free-carrier at the grain boundaries, or by a reduced free-carrier mobility due to scattering at grain boundaries. Upon annealing, the vanishing bright ring in the s-SNOM images (Fig. 4.5b and Fig. 4.9e) reveals that the free-carrier concentration in the shell region is reduced (as discussed before with the help of Fig. 4.6d). Because of the unchanged crystal structure in the shell, we can thus conclude that annealing reduces the point defects (free-carrier donors) in the shell. In the core of the annealed nanowire we find a clearly improved crystallinity (see Fig. 4.10c). The carrier mobility is thus expected to increase, which would come along with an increase of the near-field am-

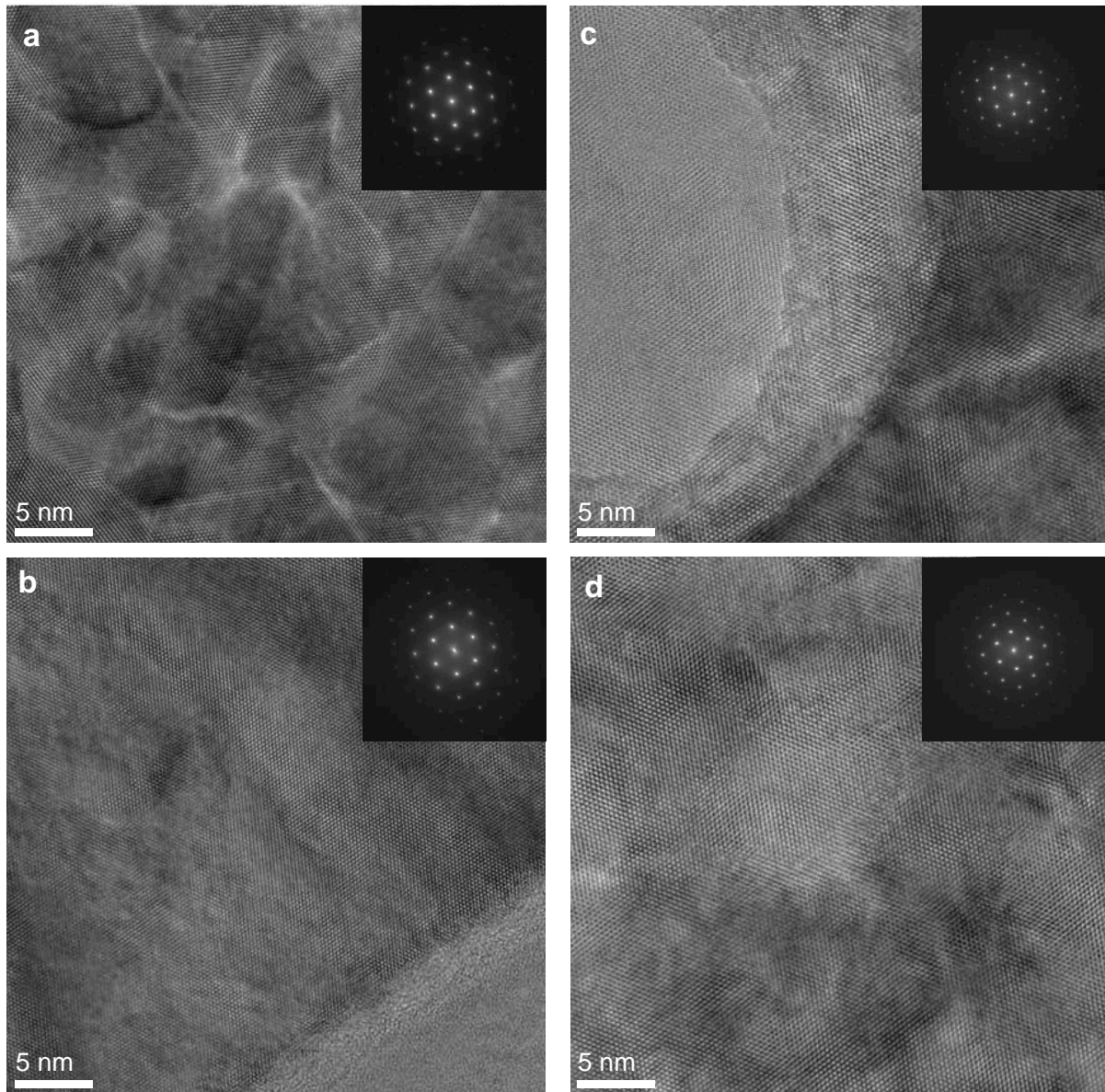


**Figure 4.10: HRTEM images of a ZnO nanowire cross-sections.** (a) Image of the core region of the as-deposited ZnO nanowire. Contrast variations over the field of view indicate the presence of a large number of crystal defects, nanopores, probably small angle grain-boundaries and threading dislocations. The inset shows a Fast Fourier Transform (FFT) of the image showing a set of reflections corresponding to [0001] crystallographic zone of ZnO. The slight azimuthal elongation of reflections in FFT reveals a mutual rotation of parts of the crystal lattice in the core, amounting to a few degrees. (b) Image of the shell region of the as-deposited ZnO nanowire, showing an almost defect-free crystal structure. (c) Image of the core region of the annealed ZnO nanowire, showing that large voids (bright region at the left part of the image) have been formed. The FFT analysis displays a good crystallinity. The absence of a crystal rotation substantiates that grain boundaries vanish after annealing. (d) Image of the shell region of the annealed ZnO nanowire, showing a small number of voids (bright region in the center of view), however, much smaller in size than the voids in the core (Fig. 4.10c). The FFT analysis confirms the good crystallinity, and shows that annealing did not change the crystal structure.

plitude and phase (see Fig. 4.6c). However, the near-field amplitude and phase in the core do not change upon annealing, which lets us conclude that the free-carrier concentration is below  $10^{18}$  carriers/cm<sup>3</sup>, where any change of the mobility is not detectable.

Our observations provide detailed and spatially resolved insights not only into the nanowire growth, but also how annealing affects the free-carrier distribution in unintentionally doped ZnO nanowires. This knowledge will be essential for optimising ZnO nanowires for applications in (opto-)electronic devices. On the other hand, our studies reveal that a large local free-carrier concentration within a nearly perfect crystalline structure can be achieved by lateral nanowire growth. Such nanowires are highly interesting for applications where a high conductivity simultaneously to optical transparency is required (*e.g.* transparent electrodes). Furthermore, our findings explain why etching of as-deposited ZnO nanowires yields tailored ZnO nanotubes [157, 158, 159]: because of its high defect density, the core is strongly and selectively etched, leaving an almost defect-free outer shell.

## **Discussion of the Possible Influence of Polishing on the IR Near-field Contrast**

The preparation of a cross-section creates an artificial surface and the properties of this surface might be different from bulk properties, particularly in semiconductors due to carrier depletion, for example. Such depletion layers are typically in the range of a few nanometers [160]. For a surface sensitive technique such as scanning tunnelling microscopy (STM) this might be indeed an issue, as STM is very dependent on the electronic state of the surface. s-SNOM, however, is quite different in this regard. s-SNOM probes a volume near the surface (and thus a substantial amount of interior material) rather than just the surface. The probing depth is typically around 30 nm [131, 161]. A depletion layer of a few nanometer thickness will thus not significantly modify the s-SNOM signal.

Another aspect of the sample preparation is that polishing and ion-beam milling will create crystal damage and eventually a thin amorphous surface layer. Yet, both procedures will yield a different amount and type of damage, which might affect the depletion layer and image contrast. By comparing mechanically and FIB polished cross sections, we do not see a significant difference in the s-SNOM contrast. In both cases we observe a bright ring in the as-deposited nanowires, which vanishes after annealing. This is another clear indication that the damaged/depleted surface layer has only

minor influence on the image contrast.

In summary: As a volume rather than the surface states are probed, and because the s-SNOM signal is independent of the polishing procedure, we can conclude that the effect of surface polishing is minor regarding the qualitative image contrast. The exact values obtained for the local carrier density on the other hand might be modified due to the surface polishing.

We furthermore emphasise: The contrast ring vanishes after annealing but both as-deposited and annealed nanowires were polished the same way. Within one image of the as-deposited nanowires (*e.g.* Fig. 1a) the contrast ring varies for the individual nanowires (some as-deposited nanowires even do not even exhibit a contrast ring), although the polishing is exactly the same for the nanowires seen in one image. Obviously, we observe an intrinsic nanowire property in the near-field images.

## Discussion of Polishing Residues on the IR Near-field Contrast

In Fig. 4.5a we show near-field images of as-deposited ZnO nanowires, where polishing left small particles on the nanowire cross-sections. To demonstrate that the near-field contrast (bright ring) of the as-deposited nanowires is not related to the presence of the polishing remainders, we performed near-field microscopy of a similar sample without the polishing remainders. The topography and near-field images of this sample are shown in Fig. 4.11, revealing a smooth topography and the typical ring-like contrast in the infrared amplitude and phase images. We thus can exclude that the polishing remainders are the cause of the ring-like infrared contrast seen in the near-field images of Fig. 4.5a.

This sample is not directly comparable with Fig. 4.5b as it was grown within another experiment (using the same growth conditions as for the previously shown nanowires). Note that all previously shown nanowires were grown within the same process and then either directly prepared for the s-SNOM and TEM experiments, or annealed previous to the sample preparation. This way we can exclude variations in the growth process as origin for the measured results.

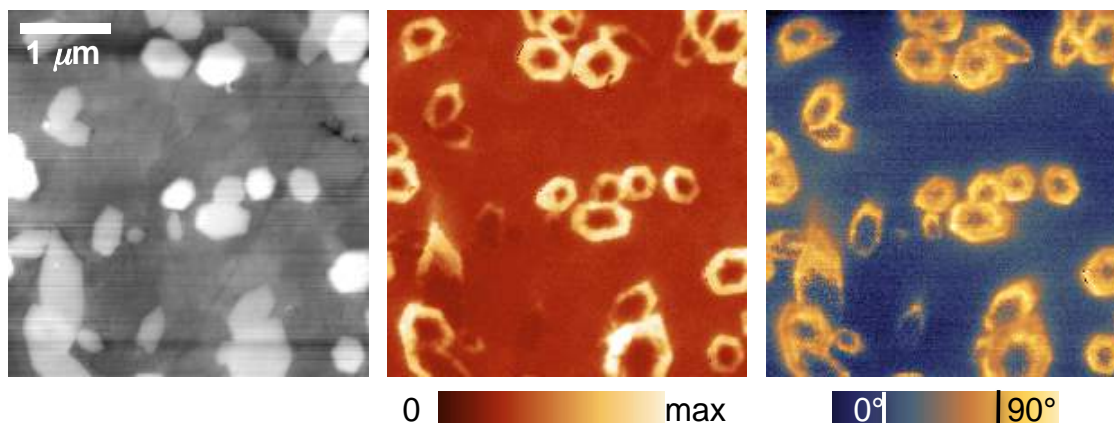


**Figure 4.11: s-SNOM images of mechanically polished ZnO nanowire sample.** Topography (left), IR amplitude (middle) and phase (right) images of as-deposited ZnO nanowires embedded into a CuSCN-matrix.

## 4.6 Conclusion

In conclusion, we have demonstrated correlative infrared-electron nanoscopy, a novel analytical imaging tool providing nanoscale resolved IR images and atomically resolved TEM images of *one and the same* nanostructures. Applying it to ZnO nanowires, we obtained nanoscale resolved real-space maps of radial free-carrier distributions exhibiting a clear correlation to structural defects seen by TEM. We point out that correlative infrared-electron nanoscopy has a wide application potential far beyond nanowire research. We envision highly interesting and novel insights into exotic conductors such as graphene or topological insulators, where the interplay between local conductivity and local crystal structure is a widely unexplored terrain. Because of the high chemical sensitivity of IR light, correlative infrared-electron nanoscopy could be also applied for combined nanoscale chemical and structural mapping of organic and biological matter.

# 5

## Infrared Absorption Spectroscopy of Individual SiN Nanoparticles

*In this chapter we study how the near-field contrast scales with the size of the investigated sample, i.e the sensitivity of s-SNOM. Using  $\text{Si}_3\text{N}_4$  nanoislands as an experimental test system, we demonstrate that s-SNOM can chemically identify particles as small as 5 nm by IR near-field fingerprint spectroscopy of the Si-N stretching bond. Employing the extended finite-dipole model we show that the near-field phase spectra of small particles correlate well with their far-field absorption spectra. On the other hand, the spectral near-field contrast does not scale with the volume of the particles. We find a nearly linear scaling law, which we can attribute to the near-field coupling between the near-field probe and the substrate. Our results provide fundamental insights into the spectral near-field contrast of nanoparticles and clearly demonstrate the capability of s-SNOM for nanoscale chemical mapping based on local infrared absorption.*

## 5.1 Introduction

In the previous two chapters we used IR s-SNOM's capability for free-carrier profiling in order to solve application relevant and technologically-important questions. We demonstrated how s-SNOM can be used to quantify the free-carrier concentration and mobility as well as s-SNOM's ability to visualise the free-carrier distribution in semiconductor nanowires. But IR s-SNOM also offers an unprecedented chemical sensitivity even to small sample volumes. IR s-SNOM spectroscopy, for example, has successfully been applied to protein spectra of a Tobacco Mosaic Virus (TMV) with only 18 nm in diameter. However, if the sample volume decreases, the near-field signal decreases too due to a reduced near-field interaction between tip and the smaller particle, and in turn cannot be separated from the intrinsic noise anymore [33, 78]. In this chapter, we will focus on the question how the spectral near-field amplitude and phase contrasts scale with the diameter of a small particle. We will investigate, what is the smallest particle that s-SNOM can chemically identify, in other words, what is the sensitivity of s-SNOM.

In general, the sensitivity of s-SNOM can be improved by placing the sample of interest (*e.g.* nanoparticles or thin films) on substrates with a high refractive index (*e.g.* Si) or with polaritonic properties (*e.g.* SiC) [33, 128]. This sensitivity improvement can be explained by near-field coupling between tip and substrate, which enhances the field strength at the tip apex [33, 128, 162, 163, 164]. The tip-substrate configuration in s-SNOM - acting like a ground-plane antenna [33] and referred as to *substrate-enhanced s-SNOM* [33, 128] - has enabled the imaging of gold particles with sizes below 10 nm, [33, 78] the spectral signature of thin polymer-films [128] and the secondary structure of amyloid fibrils [165] supported by a gold substrate. However, the interpretation of the IR near-field spectra is still a challenging task, owing to the lack of an appropriate theoretical description of the tip-sample-substrate near-field interaction. Most current s-SNOM models such as the dipole model [26] (described in chapter 2.3) or the finite-dipole model [81, 92] (described in chapter 2.3) used in the previous two chapters do not take into account the finite size of the sample and therefore cannot explain size-dependent spectral near-field contrasts [153].

In this chapter we demonstrate that substrate-enhanced s-SNOM with interferometric detection allows for IR amplitude and phase resolved spectroscopy of the vibrational fingerprint of 5 nm high nanoislands (see schematic illustration in Fig. 5.1). Particularly, we report near-field spectroscopy of the Si-N stretching mode (optical phonon polariton).  $\text{Si}_3\text{N}_4$  is chosen as a model-system because the Si-N stretching mode is

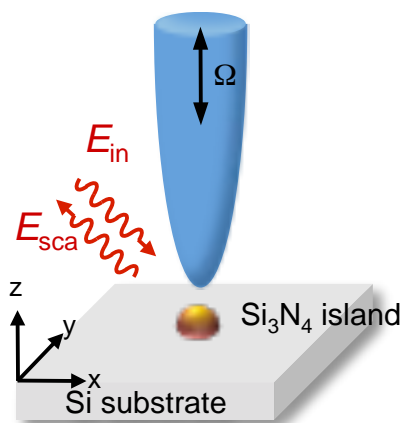


**Figure 5.1:** IR near-field probing of  $\text{Si}_3\text{N}_4$  nanoislands with an IR laser illuminating the scanning-probe tip.

expected at  $830\text{ cm}^{-1}$  [166], which is within the spectral range that is experimentally accessible to our IR laser systems. Using the extended finite-dipole model (described in chapter 2.3), a relatively novel theoretical framework based on the near-field interaction between tip, sample and substrate, we perform a detailed analysis of the near-field amplitude and phase spectra and compare the results with calculated far-field absorption spectra. The extended finite-dipole model has been developed by A. Cvitkovic [88] and has been applied successfully to describe the near-field contrasts of small gold and polystyrene particles [33, 78].

## 5.2 Size Dependence of the IR Near-field Contrast of $\text{Si}_3\text{N}_4$ Nanoislands

For our systematic study how the spectral near-field contrast scales with small sample volumes a sample comprising  $\text{Si}_3\text{N}_4$  nanoislands was prepared by the group of S.R. Leone at the UC Berkeley (USA). The  $\text{Si}_3\text{N}_4$  particles were prepared by first annealing Si(111) wafers in an ultra-high-vacuum chamber with a base pressure of  $1 \cdot 10^{-7}\text{ Pa}$ . A Si wafer was cleaned by three separate sonications in acetone, 2-propanol, and methanol, dried in a nitrogen flow, and transferred into the vacuum chamber. The Si wafer was first heated to  $800\text{ }^\circ\text{C}$  and then flashed three times for 60 s at  $1020\text{ }^\circ\text{C}$ . Under these conditions the surface silicon oxide layer gradually decomposes resulting in self-assembled silicon nanoislands [167]. Next, the sample was exposed to nitrogen plasma generated with a radio frequency plasma source. *In situ* Auger spectroscopy (see Figure 5.2) confirmed the formation of silicon nitride, presumably the  $\text{Si}_3\text{N}_4$  phase,

without the incorporation of impurities such as carbon and oxygen. Finally, the nitrified sample was flash heated again for 10 min at 1020 °C. This procedure yields Si<sub>3</sub>N<sub>4</sub> pyramidal-shaped nanoislands with a base radius between 10 and 20 nm and varying heights below 10 nm at a density of  $5 \cdot 10^8 \text{ cm}^{-2}$ .

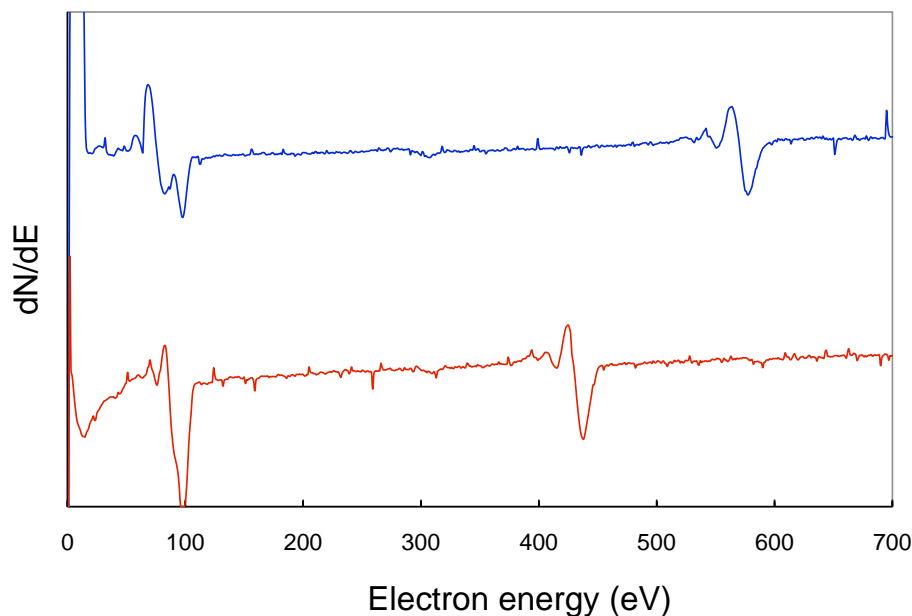


**Figure 5.2: Auger electron spectra of a Si wafer before (blue line) and after (red line) nitridation.** Both samples clearly show the Si LMM peak at around 96 eV. Before nitridation the Si wafer is covered a natural oxide layer, represented in the measurement by the oxygen KLL peak at 570 eV. This oxygen peak vanishes after the nitridation process and gives rise to a N KLL peak at around 420 eV. These results ensure that the sample is only composed of Si and N, other components, such as O, are negligible. Auger measurements courtesy of Dr. Y. Abate.

Near-field imaging of the Si<sub>3</sub>N<sub>4</sub> nanoislands was performed with our home-built s-SNOM (schematics in Fig. 2.4), employing conventional Pt-coated Si-tips (Nanosensors, PPP-NCHPt) with a tip apex radius of  $R \approx 20 \text{ nm}$ . The vertical tip vibration amplitude was set to  $A = 20 - 30 \text{ nm}$  and the vibration frequency to  $\Omega \approx 300 \text{ kHz}$ . For all experiments presented in this chapter second harmonic demodulation ( $n = 2$ ) was employed yielding amplitude  $s_2$  and phase  $\varphi_2$  images simultaneously with topography.

Figure 5.3a shows a typical topography image and Figure 5.3b the simultaneously recorded IR amplitude  $s_2$  and phase  $\varphi_2$  images of the Si<sub>3</sub>N<sub>4</sub> islands with heights ranging from 5–10 nm. The heights of the islands are directly measured from the topography image. Near-field amplitude  $s_2$  and phase  $\varphi_2$  images were recorded on and off the small-particle IR resonance of Si<sub>3</sub>N<sub>4</sub> at  $950 \text{ cm}^{-1}$  and  $1050 \text{ cm}^{-1}$ , respectively. In both amplitude images the Si<sub>3</sub>N<sub>4</sub> nanoislands appear darker than the substrate. Such a negative contrast has been also observed for Au [78] and InGaN [168] nanoparticles

in previous *s*-SNOM studies. Comparing the IR amplitude images at the two different frequencies, no significant change of the contrast between substrate and nanoislands is seen. The near-field phase images, however, exhibit a pronounced spectral contrast variation. In the phase image at  $950\text{ cm}^{-1}$  we observe a clear contrast between the  $\text{Si}_3\text{N}_4$  particles and the substrate, which nearly vanishes at  $1050\text{ cm}^{-1}$ . Typically, a spectral phase contrast in *s*-SNOM reveals an absorption in the sample, for example caused by a vibrational resonance [22, 153]. Thus, the spectral phase contrast of the  $\text{Si}_3\text{N}_4$  nanoislands indicates that we map the vibrational resonance of the Si-N stretching bond.

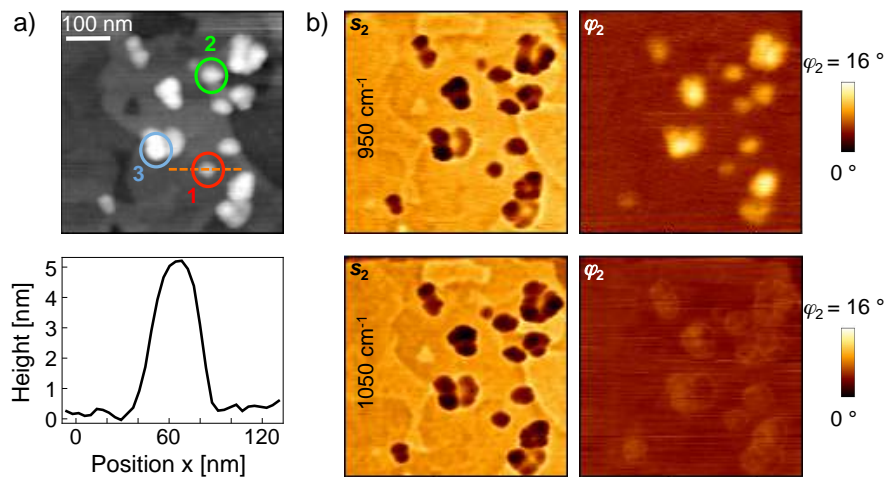


**Figure 5.3: Experimental images of isolated  $\text{Si}_3\text{N}_4$  nanoislands.** (a) Topography, as well as (b) IR near-field amplitude  $s_2$  and phase  $\varphi_2$  at the two frequencies  $950$  and  $1050\text{ cm}^{-1}$ . The line plot shows the height profile along the dashed orange line in the topography image. The numbered circles 1 to 3 mark the particles analysed in Figures 5.5 and 5.6.

To study the frequency-dependent near-field contrast between the  $\text{Si}_3\text{N}_4$  nanoislands and the Si substrate in more detail, we imaged the sample at six different frequencies between  $890\text{--}1100\text{ cm}^{-1}$ . Near-field spectra are obtained by measuring amplitude  $s_2$  and phase  $\varphi_2$  on top of individual  $\text{Si}_3\text{N}_4$  nanoislands at the different frequencies. We evaluated three representative nanoislands with heights of 5 nm, 7 nm and 9 nm (labeled 1 to 3 in Figure 5.3a). Experimental amplitude and phase spectra are shown as symbols in Figures 5.5a and b. For all three nanoislands the amplitude  $s_2$  spectra reveal only a weak signal decrease between  $900\text{--}1000\text{ cm}^{-1}$ , which explains why in the amplitude images of Figure 5.3b the spectral amplitude contrast is barely visible. In the phase  $\varphi_2$  spectra (Figure 5.5b) we find a peak with a maximum at  $930\text{ cm}^{-1}$ . We furthermore find that both the spectral amplitude contrast  $\Delta s_2$  (Figure 5.5a) and the spectral phase contrast  $\Delta \varphi_2$  (Figure 5.5b), decrease with decreasing height of the nanoisland.

We hereby use the following definitions for the spectral amplitude and phase,

$$\Delta s_2 = s_2^{\max} - s_2^{\min}$$

and

$$\Delta \varphi_2 = \varphi_2^{\max} - \varphi_2^{\min}$$

as illustrated in Figure 5.4.

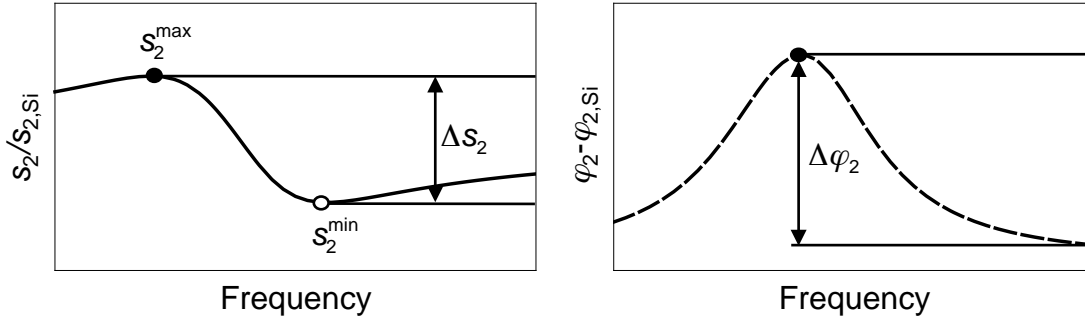


**Figure 5.4:** Definition of spectral amplitude  $\Delta s_2 = s_2^{\max} - s_2^{\min}$  and phase contrast  $\Delta \varphi_2 = \varphi_2^{\max} - \varphi_2^{\min}$ .

To understand the s-SNOM amplitude and phase contrast of the nanoislands we perform model calculations of their expected near-field amplitude  $s_n$  and phase  $\varphi_n$  signals. To this end, we use the extended finite-dipole model (as described in chapter 2.3). Hereby, the  $\text{Si}_3\text{N}_4$  nanoislands are described as spheres with diameter  $2r$  located in between the tip and the substrate.  $2r$  corresponds to the nanoparticles' height  $d$  measured from the topography (see Fig. 5.3a). For the polarisability of the  $\text{Si}_3\text{N}_4$  nanoislands we then can use that of a sphere, which is given by

$$\alpha_{\text{sphere}} = 4\pi \cdot r^3 \frac{\varepsilon(\omega) - 1}{(\varepsilon(\omega) + 2)},$$

where  $\varepsilon(\omega)$  represents the dielectric function of  $\text{Si}_3\text{N}_4$ . Considering the near-field interaction between tip apex, substrate and sample we can calculate the near-field amplitude  $s_2(r)$  and phase  $\varphi_2(r)$  as a function of the particle radius  $r$ .

Using literature data for the dielectric function  $\varepsilon(\omega)$  of  $\text{Si}_3\text{N}_4$  from ref. [169] we calculate near-field amplitude  $s_2$  and phase  $\varphi_2$  spectra for  $\text{Si}_3\text{N}_4$  spheres with diameters of 5 nm, 7 nm and 9 nm. The amplitude spectra (solid lines in Figure 5.5a) are in good agreement with the experimental data and clearly reproduce the amplitude decrease between 900 and 1000  $\text{cm}^{-1}$ . These results reveal the typical s-SNOM amplitude spectra of a vibrational resonance, which has been derived and shown earlier for

a poly(methyl methacrylate) (PMMA) [22] film and a tobacco mosaic virus. [153] The near-field amplitude spectra acquire a dispersive line shape similar to far-field reflectivity spectra. We further find in Figure 5.5a that both the experimental and calculated  $s_2$  signals, increase with decreasing particle size, while the spectral amplitude contrast  $\Delta s_2$  decreases. The increasing signal level is caused by an enhanced tip-substrate near-field coupling, when the tip-substrate distance  $d$  is reduced.[33] The vanishing spectral contrast can be explained by the decreasing particle polarisability  $\alpha_{\text{sphere}}$  when the particle diameter  $2r$  becomes smaller. We also find good agreement between the calculated (Figure 5.5c) and experimental (Figure 5.5b) phase spectra  $\varphi_2$ , showing a significant peak at  $950 \text{ cm}^{-1}$ , which decreases for smaller particle diameters. The small differences between experiment and theory can be explained by two main factors:

- (i) The  $\text{Si}_3\text{N}_4$  islands have pyramidal shape. In the calculation, however, we assume spherical particles with diameters corresponding to the heights measured from the topography image.
- (ii) The dielectric function of  $\text{Si}_3\text{N}_4$  used for the calculations is taken from literature, [169] which may differ from the dielectric function of the  $\text{Si}_3\text{N}_4$  nanoislands.

## 5.3 Relation between Near-field Phase and Far-field Absorption

Interestingly, the near-field phase spectra resemble the absorption spectra of small particles. The correlation between near-field phase and far-field absorption spectra has been already pointed out earlier in the work of Taubner *et al.* [22], where calculated near-field phase and far-field absorption spectra of polymer bulk samples were compared. To establish this important correlation, particularly for nanoparticles, we calculate the far-field absorption cross-section of  $\text{Si}_3\text{N}_4$  particles on a Si substrate. We assume an illumination polarisation normal to the Si surface (*i.e.* grazing incidence). Taking into account the influence of the substrate (coupling between particle dipole and its image dipole in the sample), we find for the  $\text{Si}_3\text{N}_4$  particle a polarisability

$$\alpha_{\text{sphere}}^* = \frac{\alpha_{\text{sphere}}}{1 - \frac{\alpha_{\text{sphere}} \left( \frac{\epsilon - 1}{\epsilon + 1} \right)}{(16\pi r^3)}}$$

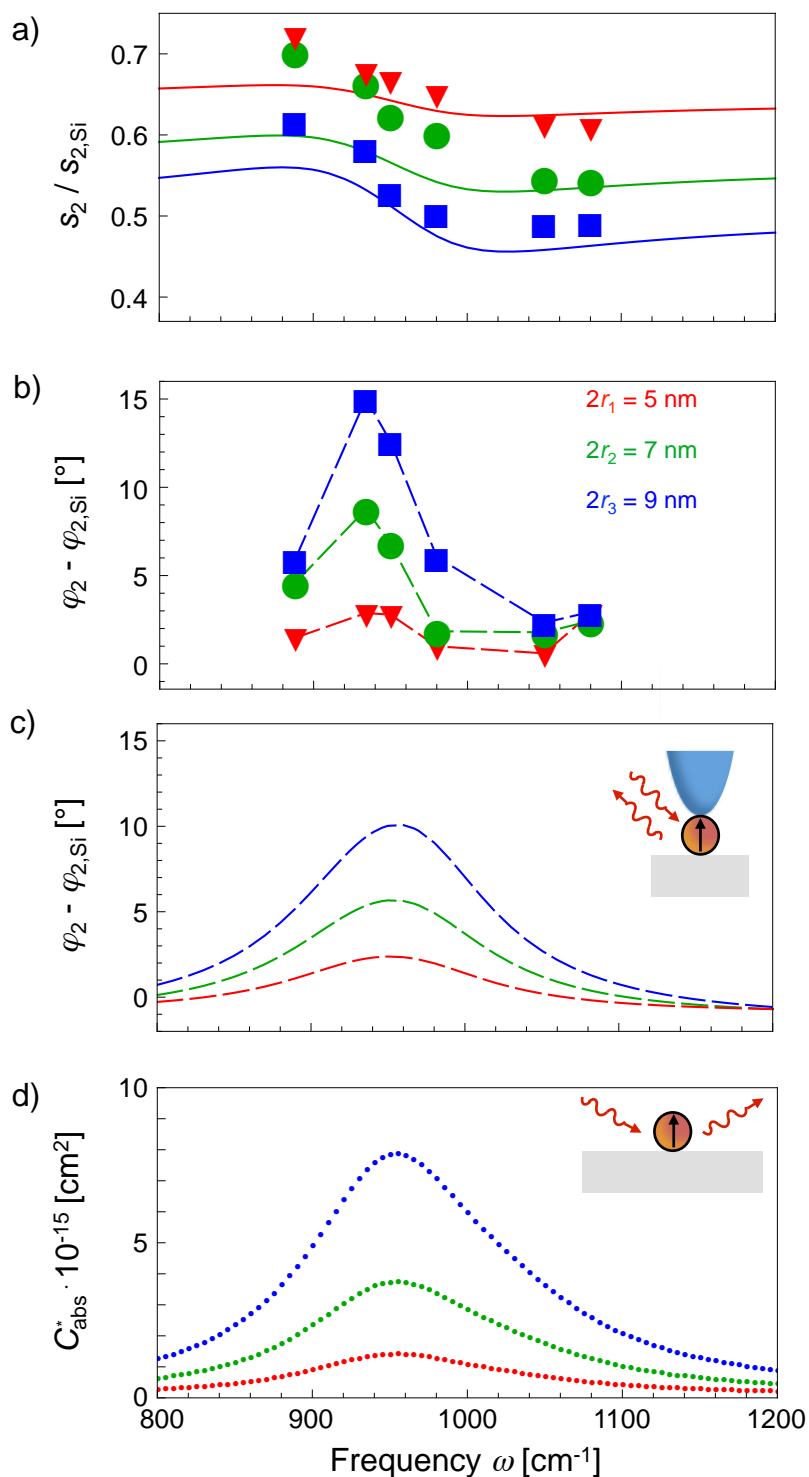


**Figure 5.5: IR spectral characteristics of individual Si<sub>3</sub>N<sub>4</sub> nanoparticles.** (a) Near-field amplitude  $s_2$ . Symbols represent values obtained from particles 1 to 3 in Figure 5.3a. The solid lines display calculations based on the extended finite dipole model (see chapter 2.3) and Si<sub>3</sub>N<sub>4</sub> dielectric data taken from literature.[169] (b) Experimental and (c) calculated near-field phase  $\varphi_2$  of particles 1 to 3. In a) - c), the particles are located on a Si substrate and both the experimental and the calculated data are normalised to the IR near-field amplitude  $s_{2,Si}$ , respectively phase  $\varphi_{2,Si}$ , of the flat Si surface. (d) Calculated absorption cross-section of single Si<sub>3</sub>N<sub>4</sub> nanoparticles.

yielding an absorption cross-section [170]

$$C_{\text{abs}}^* = k\text{Im}[\alpha_{\text{sphere}}^*].$$

In Figure 5.5d, we show  $C_{\text{abs}}^*$  for 5 nm, 7 nm and 9 nm  $\text{Si}_3\text{N}_4$  particles. Comparing the near-field phase signals  $\varphi_2$  and the far-field absorption cross-section  $C_{\text{abs}}^*$  we find that both exhibit the same qualitative spectral behaviour. This clearly shows that the phase of the tip-scattered light reveals the absorption characteristic of small particles, despite the complex near-field interaction between tip, particle and substrate.

We can understand the relation between the far-field absorption cross-section  $C_{\text{abs}}^*$  of the particles and the near-field phase  $\varphi_2$  by considering that the scattering coefficient  $\sigma = se^{i\varphi}$  is given by  $\sigma = \sigma_{\text{t-s}} + \sigma_{\text{p,eff}}$ , where  $\sigma_{\text{t-s}}$  is the scattering coefficient of the tip-substrate configuration without a sample (particle) and  $\sigma_{\text{p,eff}}$  the additional contribution when a sample (particle) is located between tip and substrate. Assuming that  $s_{\text{t-s}} \gg s_{\text{p,eff}}$ , we obtain  $\varphi = \arg[\sigma] \approx \text{Im}[\sigma_{\text{p,eff}}]/s_{\text{t-s}}$ . With  $\sigma_{\text{p,eff}} = k^2 \cdot \alpha_{\text{p,eff}}$  ( $\alpha_{\text{p,eff}}$  being the effective polarisability of the particle when located between tip and substrate) and the general relation  $C_{\text{abs}} = k \cdot \text{Im}[\alpha]$  for small scatterers, we find that the phase of the scattered light is proportional to the effective absorption cross-section of the particle in the tip-substrate system,  $\varphi \propto \text{Im}[\alpha_{\text{p,eff}}] \propto C_{\text{abs,eff}}$ . Comparing now the Figures 5.5c and 5.5d we find that the phase spectra  $\varphi_2$  exhibit a good agreement with  $C_{\text{abs}}^*$ , the latter being the absorption cross-section of the particle on the substrate alone, *i.e.* in the absence of the tip. We thus conclude that the presence of the tip does not significantly modify the spectral signature of the particles.

## 5.4 Spectral Near-field Amplitude and Phase Contrast for Small Particles

To explore the sensitivity of s-SNOM, we study the spectral IR amplitude and phase contrasts (Figure 5.4) as a function of the particle height. To this end, we show in Figure 5.6a the measured  $\text{Si}_3\text{N}_4$  amplitude signals  $s_2^{\text{max}}$  (filled symbols) and  $s_2^{\text{min}}$  (open symbols) as a function of the particle height  $2r$ . For comparison, we also show the measured amplitude signal  $s_{2,\text{Si}}$  above the Si as a function of the tip-substrate distance  $d$  (grey diamonds). Two important observations are made:

- (i) For a given particle height  $2r$ , the amplitude  $s_2^{\text{max}}$  is larger than the signal  $s_{2,\text{Si}}$  measured for a tip-substrate separation  $d = 2r$ . This is because the presence of

the  $\text{Si}_3\text{N}_4$  particle enhances the near-field interaction between tip and substrate. [28]

- (ii) For any tip sample separation  $d$ , the amplitude signals  $s_2^{\text{max}}(d)$  on top of the  $\text{Si}_3\text{N}_4$  particles are smaller than the amplitude signal  $s_{2,\text{Si}}(d = 0)$  measured directly at the Si surface. This explains why in the amplitude images in Figure 5.3b the particles appear darker than the substrate (note that the oscillating AFM tip is following the sample surface).

In Figure 5.6b we observe that the measured phase contrast  $\Delta\varphi_2$  (filled symbols) increases with an increasing particle height, while the measured phase signal  $\varphi_{2,\text{Si}}(d)$  on the Si substrate (grey diamonds) is constant, *i.e.* independent of the tip-substrate distance  $d$ . This explains why the particles in the phase images at  $950\text{ cm}^{-1}$  (Figure 5.3b) appear brighter than the substrate. Calculations using the extended finite-dipole model (solid lines for the amplitude respectively dashed black lines for the phase) clearly reproduce the experimental data in Figures 5.6a and b. We note that the increasing contrast is only valid for particles smaller than the apex radius  $R$ , which is the approximation underlying the model. The calculations also show that for particles with  $2r < 5\text{ nm}$  the amplitude as well as the phase contrast vanish, thus challenging their experimental detection. The reason for the decreasing contrast of both is the decreasing particle polarisability when the particle becomes smaller. We note that the particle size where  $\Delta s_2$  and  $\Delta\varphi_2$  vanish is determined by the size and the optical properties of the probing tip. Thus, using sharper tips with radii below  $10\text{ nm}$  and with optimised antenna properties [171, 172] of the tip-substrate configuration, the detection limit could be pushed even further towards smaller particles.

In Figure 5.6c we compare the calculated spectral near-field amplitude and phase contrasts,  $\Delta s_2$  and  $\Delta\varphi_2$ , with the far-field absorption  $C_{\text{abs}}^*$ . We observe that both the amplitude and phase contrast, show a nearly linear increase with the particle diameter  $2r$  between  $5\text{ nm}$  and  $20\text{ nm}$ , while the absorption cross-section  $C_{\text{abs}}^*$  scales cubically. This beneficial scaling law for IR near-field spectroscopy can be attributed to the increased near-field coupling between tip and substrate when the particle size (*i.e.* the gap width  $d = 2r$ ) is decreased. The enhanced near-field coupling provides higher fields for polarising the reduced amount of particle matter. Thus, it partially compensates the decreasing particle polarisability [33].

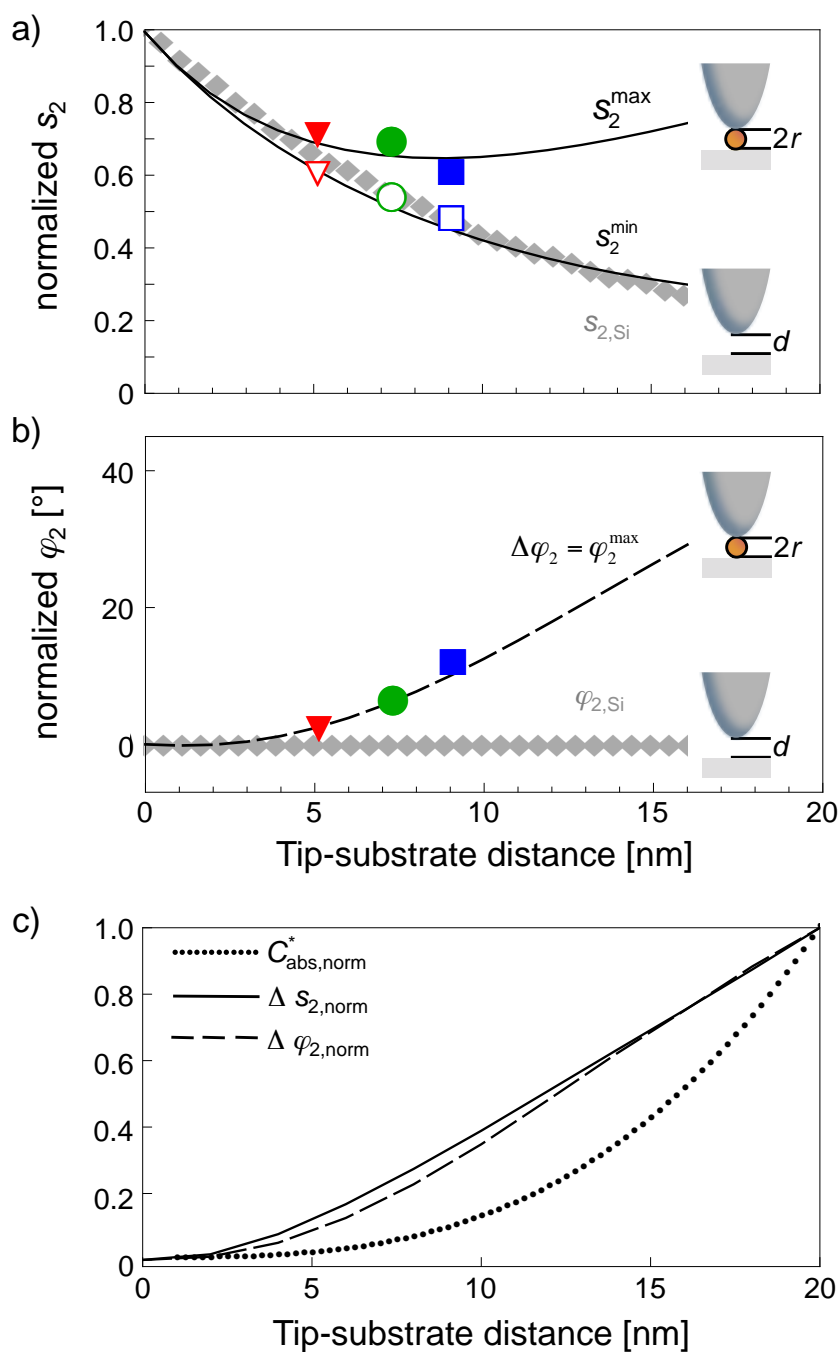


**Figure 5.6:** IR signals of single  $\text{Si}_3\text{N}_4$  nanoparticles as function of the particle diameter  $d$ . (a, b) Experimental (grey diamonds) near-field amplitude  $s_2$  and phase  $\varphi_2$  at  $950\text{ cm}^{-1}$  as a function of distance  $d$  between tip and Si substrate. Filled (respectively open symbols) in (b) represent experimentally obtained  $s_2^{\max}$  (respectively  $s_2^{\min}$ ) values for particles 1 to 3 in Figure 5.3a, whereas solid black lines show the theoretical  $s_2^{\max}$  respectively  $s_2^{\min}$  values for an increasing particle diameter  $2r$ . Filled symbols in (c) represent  $\varphi_2^{\max}$  values for particles 1 to 3 in Figure 5.3a and the black dashed line represents the theoretical  $\varphi_2^{\max}$  curve. All values have been normalised to the value taken on the Si substrate at  $d = 0$ . (c) Calculated absorption cross-section (dotted line), near-field amplitude contrast (solid line) and near-field phase contrast (dashed line), all normalised to the corresponding value of a 20 nm  $\text{Si}_3\text{N}_4$  particle.

## 5.5 Conclusions

We have demonstrated the near-field detection of the IR spectrum of nanoislands with heights below 10 nm by using an interferometric s-SNOM. The results show that near-field IR phase spectra of small particles exhibit a significant correlation to the far-field absorption. It can be understood by the fact that the dielectric properties of a material are complex-valued numbers [170], where the real part describes the refractive and the imaginary part the absorptive properties. The latter gives rise to a phase shift of the scattered light with respect to the incident light, which can be easily recorded by interferometric detection in s-SNOM. Consequently, interferometric s-SNOM has the capability to map the IR absorption of materials with nanoscale spatial resolution. By engineering the antenna function of metal probe tips and by reducing the tip apex below 10 nm [173] we envision s-SNOM to become a valuable tool for IR absorption spectroscopy of even single macromolecules.

# List of Publications

## Publications covered by this thesis

**J.M. Stiegler**, R. Tena-Zaera, O. Idigoras, A. Chuvilin, R. Hillenbrand

*Correlative infrared-electron nanoscopy in material science - revealing the local structure-conductivity relationship in semiconductor nanowires*

Nature Communications **3**, 1131 (2012)

### Chapter 4

**J.M. Stiegler**, J. Abate, A. Cvitkovic, Y. Romanyuk, A. Huber, S. Leone, and R. Hillenbrand

*Nanoscale infrared absorption spectroscopy of individual nanoparticles enabled by scattering-type near-field microscopy*

ACS Nano **5**, 6494 (2011)

### Chapter 5

**J.M. Stiegler**, A.J. Huber, S.L. Diedenhofen, J. Gomez Rivas, R.E. Algra, E.P.A.M. Bakkers, and R. Hillenbrand

*Nanoscale free-carrier profiling of individual semiconductor nanowires by infrared near-field nanoscopy*

Nano Letters **10**, 1387 (2010)

### Chapter 3

## Other publications

R. Krutokhvostov, A. A. Govyadinov, **J.M. Stiegler**, F. Huth, A. Chuvilin, P. S. Carney, and R. Hillenbrand

*Enhanced resolution in subsurface near-field optical microscopy*

Optics Express **20**, 599 (2012)



# Acknowledgments

I want to express my special thanks to my thesis advisor Dr. Rainer Hillenbrand, who gave me the opportunity to work in the exciting field of nano-optics. Rainer, I would like to thank you a lot for your guidance throughout my PhD thesis, for all the stimulating discussions, and for helping me to become a better researcher. You showed me the tweaks of using the near-field microscope and sharpened my view on interpreting my measurements, and you taught me how to write scientific papers. And I'm grateful for the possibility of travelling to international conferences, where I had the chance to meet other scientists, present and discuss my own research.

I would like to thank Prof. Txema Pitarke for the opportunity to work and carry out my experiments at CIC nanoGUNE. I want to thank the administration of CIC nanoGUNE for all their assistance. I also would like to thank Prof. Wolfgang Baumeister for the opportunity to conduct my work during the first year of my thesis in the Molecular Structural Biology department at the Max-Planck-Institute of Biochemistry in Martinsried.

I would like to express my gratitude to Prof. Jaime Gomez-Rivas, Dr. Erik Bakkers, Dr. Silke Diedenhofen, and Dr. Rienk Algra for the inspiring and rewarding collaboration on the InP nanowires.

I am thankful to Dr. Andrey Chuvilin at CIC nanoGUNE for working together on the FIB preparation and TEM imaging of my nanowire samples, for the many stimulating discussions and for patiently answering all my questions. Thank you also, Dr. Ramon Tena Zaera at IK4-Cidetec for a great collaboration and all the fruitful discussions during our common work on the ZnO nanowire project. Thanks to Olatz Idigoras (CIC nanoGUNE) who coated the ZnO with Al<sub>2</sub>O<sub>3</sub> and MgO. Dr. Christopher Tollan (CIC nanoGUNE) who taught me how to prepare mechanical polished cross-sections.

I would like to thank Dr. Yohannes Abate, Dr. Yaroslav Romanyuk, and Prof. Stephen Leone for the interesting discussions and the fruitful collaboration in the Si<sub>3</sub>N<sub>4</sub> nanoparticle project.

Prof. Scott Carney for his contribution to my work on the  $\text{Si}_3\text{N}_4$  nanoparticles, but also for the many scientific as well as non scientific discussions.

Dr. Javier Aizpurua (DIPC, for the stimulating discussions and for his help with the calculations of the layered InP systems.

I also want to thank my colleagues Dr. Andreas Huber and Dr. Antonija Cvitkovic at the SPM group in Martinsried for fruitful discussions and for patiently answering all my questions. Dr. Fritz Keilmann for sharing his experience and knowledge about optics in general, and s-SNOM in particular. Dr. Reinhard Guckenberger for his expertise in AFM and electronics.

I am thankful to all the present and past colleagues in the nanooptics group at CIC nanoGUNE including Dr. Pablo Albella, Dr. Pablo Alonso, Dr. Jianing Chen, Dr. Alexander Govyadinov, Dr. Dimitry Melnikau, Dr. Martin Schnell, Florian Huth, Paulo Sarriugarte, Iban Amenabar, Roman Krutohvostovs, Carlos Crespo, and Eneko San Sebastian. I would like to thank all of you for creating such a nice and inspiring work atmosphere, but also for the occasional distractions from science when needed.

Dr. Jürgen Plitzko (MPIB, Martinsried) helped me with TEM imaging of the InP nanowires.

Dr. Alexander Rigort (MPIB, Martinsried) did a FIB preparation of the InP nanowire samples.

Patricia, ohne Dich hätte ich nie zu dieser Doktorarbeit gefunden. Vielen Dank dafür, dass du mich den größten Teil dieser Strecke unterstützt und begleitest hast.

Vanaja, thank you for all your support in the last months of the thesis, for all your patience, and for not pushing me!

Mama, Papa und Simon, vielen Dank für eure Hilfe, eure Unterstützung und den Rückhalt in all den Jahren meines Studiums und meiner Promotion. Danke!

# Bibliography

- [1] Richard P. Feynman. There's plenty of room at the bottom. *Caltech Engineering and Science*, pages 22–36, 1960.
- [2] N. Taniguchi. On the basic concept of 'nano-technology'. *Proc. Intl. Conf. Prod. Eng. Tokyo, Part II, Japan Society of Precision Engineering*, 1974.
- [3] K. Eric Drexler. *Engines of Creation: The Coming Era of Nanotechnology*. Doubleday, 1986.
- [4] M. H. Huang, S. Mao, H. Feick, H. Q. Yan, Y. Y. Wu, H. Kind, E. Weber, R. Russo, and P. D. Yang. Room-temperature ultraviolet nanowire nanolasers. *Science*, 292(5523):1897–1899, June 2001.
- [5] X. F. Duan, Y. Huang, R. Agarwal, and C. M. Lieber. Single-nanowire electrically driven lasers. *Nature*, 421(6920):241–245, January 2003.
- [6] C. Thelander, H. A. Nilsson, L. E. Jensen, and L. Samuelson. Nanowire single-electron memory. *Nano Letters*, 5(4):635–638, April 2005.
- [7] A. P. Goodey, S. M. Eichfeld, K.-K. Lew, J. M. Redwing, and T. E. Mallouk. Silicon nanowire array photoelectrochemical cells. *Journal of the American Chemical Society*, 129(41):12344–+, October 2007.
- [8] E. D. Minot, F. Kelkensberg, M. van Kouwen, J. A. van Dam, L. P. Kouwenhoven, V. Zwiller, M. T. Borgstrom, O. Wunnicke, M. A. Verheijen, and E. P. A. M. Bakkers. Single quantum dot nanowire leds. *Nano Letters*, 7(2):367–371, February 2007.
- [9] A. Colli, A. Fasoli, C. Ronning, S. Pisana, S. Piscanec, and A. C. Ferrari. Ion beam doping of silicon nanowires. *Nano Letters*, 8(8):2188–2193, August 2008.
- [10] D. E. Perea, E. R. Hemesath, E. J. Schwalbach, J. L. Lensch-Falk, P. W. Voorhees, and L. J. Lauhon. Direct measurement of dopant distribution in an individual vapour-liquid-solid nanowire. *Nature Nanotechnology*, 4(5):315–319, May 2009.

- [11] E. Meyer, H. J. Hug, and R. Bennewitz. *Scanning Probe Microscopy: The Lab on a Tip*. Springer, 2003.
- [12] M. Nonnenmacher, M. P. Oboyle, and H. K. Wickramasinghe. Kelvin probe force microscopy. *Applied Physics Letters*, 58(25):2921–2923, June 1991.
- [13] P. et al. Eyben. *Scanning Probe Microscopy*, volume 1. Springer (Berlin), 2007.
- [14] J. R. Matey and J. Blanc. Scanning capacitance microscopy. *Journal of Applied Physics*, 57(5):1437–1444, 1985.
- [15] A. Born, A. Olbrich, M. Maywald, and R. Wiesendanger. Analysis of electrical breakdown failures by means of sfm-based methods. *Applied Physics A: Materials Science & Processing*, 66:1063–1065, 1998. 10.1007/s003390051298.
- [16] Y. Inouye and S. Kawata. Near-field scanning optical microscope with a metallic probe tip. *Optics Letters*, 19(3):159–161, February 1994.
- [17] Renaud Bachelot, Philippe Gleyzes, and Albert Claude Boccara. Near field optical microscopy by local perturbation of a diffraction spot. *Microsc. Microanal. Microstruct.*, 5(4-6):389–397, 1994.
- [18] F. Zenhausern, Y. Martin, and H. K. Wickramasinghe. Scanning interferometric apertureless microscopy - optical imaging at 10 angstrom resolution. *Science*, 269(5227):1083–1085, August 1995.
- [19] F. Keilmann and R. Hillenbrand. Near-field microscopy by elastic light scattering from a tip. *Philosophical Transactions of the Royal Society of London Series A-mathematical Physical and Engineering Sciences*, 362(1817):787–805, April 2004.
- [20] B. Knoll and F. Keilmann. Near-field probing of vibrational absorption for chemical microscopy. *Nature*, 399(6732):134–137, May 1999.
- [21] R. Hillenbrand, T. Taubner, and F. Keilmann. Phonon-enhanced light-matter interaction at the nanometre scale. *Nature*, 418(6894):159–162, July 2002.
- [22] T. Taubner, R. Hillenbrand, and F. Keilmann. Nanoscale polymer recognition by spectral signature in scattering infrared near-field microscopy. *Applied Physics Letters*, 85(21):5064–5066, November 2004.
- [23] M. B. Raschke, L. Molina, T. Elsaesser, D. H. Kim, W. Knoll, and K. Hinrichs. Apertureless near-field vibrational imaging of block-copolymer nanostructures with ultrahigh spatial resolution. *Chemphyschem*, 6(10):2197–2203, October 2005.

- [24] Florian Huth, Alexander Govyadinov, Sergiu Amarie, Wiwat Nuansing, Fritz Keilmann, and Rainer Hillenbrand. Nano-ftir absorption spectroscopy of molecular fingerprints at 20 Ånm spatial resolution. *Nano Lett.*, 12(8):3973–3978, June 2012.
- [25] A. Lahrech, R. Bachelot, P. Gleyzes, and A. C. Boccara. Infrared near-field imaging of implanted semiconductors: Evidence of a pure dielectric contrast. *Applied Physics Letters*, 71(5):575–577, 1997.
- [26] B. Knoll and F. Keilmann. Infrared conductivity mapping for nanoelectronics. *Applied Physics Letters*, 77(24):PII [S0003–6951(00)00850–0], December 2000.
- [27] B. Knoll and F. Keilmann. Enhanced dielectric contrast in scattering-type scanning near-field optical microscopy. *Optics Communications*, 182(4-6):321–328, August 2000.
- [28] J. S. Samson, G. Wollny, E. Brundermann, A. Bergner, A. Hecker, G. Schwaab, A. D. Wieck, and M. Havenith. Setup of a scanning near field infrared microscope (snim): Imaging of sub-surface nano-structures in gallium-doped silicon. *Physical Chemistry Chemical Physics*, 8(6):753–758, February 2006.
- [29] M. M. Qazilbash, M. Brehm, Byung-Gyu Chae, P. . C. Ho, G. O. Andreev, Bong-Jun Kim, Sun Jin Yun, A. V. Balatsky, M. B. Maple, F. Keilmann, Hyun-Tak Kim, and D. N. Basov. Mott transition in vo2 revealed by infrared spectroscopy and nano-imaging. *Science*, 318(5857):1750–1753, December 2007.
- [30] A. J. Huber, D. Kazantsev, F. Keilmann, J. Wittborn, and R. Hillenbrand. Simultaneous ir material recognition and conductivity mapping by nanoscale near-field microscopy. *Advanced Materials*, 19(17):2209–+, September 2007.
- [31] A. J. Huber, F. Keilmann, J. Wittborn, J. Aizpurua, and R. Hillenbrand. Terahertz near-field nanoscopy of mobile carriers in single semiconductor nanodevices. *Nano Letters*, 8(11):3766–3770, November 2008.
- [32] E. J. Sanchez, L. Novotny, and X. S. Xie. Near-field fluorescence microscopy based on two-photon excitation with metal tips. *Physical Review Letters*, 82(20):4014–4017, May 1999.
- [33] A. Cvitkovic, N. Ocelic, J. Aizpurua, R. Guckenberger, and R. Hillenbrand. Infrared imaging of single nanoparticles via strong field enhancement in a scanning nanogap. *Physical Review Letters*, 97(6):060801, August 2006.
- [34] M. Born and Wolf E. *Principles of Optics*. Cambridge University Press, 2002.

- [35] E. Hecht. *Optics*. Addison Wesley, 2002.
- [36] P.W. Hawkes and J.C.H. Spence. *Science of Microscopy*. Spri, 2007.
- [37] Stefan W. Hell. Far-field optical nanoscopy. *Science*, 316(5828):1153–1158, 2007.
- [38] S. W. Hell. Toward fluorescence nanoscopy. *Nature Biotechnology*, 21(11):1347–1355, November 2003.
- [39] S. W. Hell, S. Lindek, C. Cremer, and E. H. K. Stelzer. Measurement of the 4pi-confocal point spread function proves 75 nm axial resolution. *Applied Physics Letters*, 64(11):1335–1337, 1994.
- [40] Birka Hein, Katrin I. Willig, and Stefan W. Hell. Stimulated emission depletion (sted) nanoscopy of a fluorescent protein-labeled organelle inside a living cell. *Proceedings of the National Academy of Sciences*, 105(38):14271–14276, 2008.
- [41] Christian Eggeling, Christian Ringemann, Rebecca Medda, Gunter Schwarzmann, Konrad Sandhoff, Svetlana Polyakova, Vladimir N. Belov, Birka Hein, Claas von Middendorff, Andreas Schonle, and Stefan W. Hell. Direct observation of the nanoscale dynamics of membrane lipids in a living cell. *Nature*, 457(7233):1159–1162, February 2009.
- [42] Eric Betzig, George H. Patterson, Rachid Sougrat, O. Wolf Lindwasser, Scott Olenych, Juan S. Bonifacino, Michael W. Davidson, Jennifer Lippincott-Schwartz, and Harald F. Hess. Imaging intracellular fluorescent proteins at nanometer resolution. *Science*, 313(5793):1642–1645, September 2006.
- [43] Michael J. Rust, Mark Bates, and Xiaowei Zhuang. Sub-diffraction-limit imaging by stochastic optical reconstruction microscopy (storm). *Nature Methods*, 3(10):793–795, October 2006.
- [44] R. Peters, J. Peters, K. H. Tews, and W. Bahr. Microfluorimetric study of translational diffusion in erythrocyte-membranes. *Biochimica Et Biophysica Acta*, 367(3):282–294, 1974.
- [45] E. B. Brown, E. S. Wu, W. Zipfel, and W. W. Webb. Measurement of molecular diffusion in solution by multiphoton fluorescence photobleaching recovery. *Biophysical Journal*, 77(5):2837–2849, November 1999.
- [46] P. R. Selvin. The renaissance of fluorescence resonance energy transfer. *Nature Structural Biology*, 7(9):730–734, September 2000.
- [47] J. Lakowicz. *Principles of Fluorescence Spe*. Springer, 2006.

- [48] D. B. Williams and C. B. Carter. *Transmission Electron Microscopy: A Textbook for Materials Science*. Springer, 2nd edition, 2009.
- [49] H. J. Penkalla. *Modern Methods of TEM Specimen Preparation in Material Science*. Springer Berlin Heidelberg, 2008.
- [50] Manfred Knoll. AuSSadepotential und sekundLremission elektronenbestrahlter k rper. *Zeitschrift f r Technische Physik*, 16:467–475, 1935.
- [51] Manfred von Ardenne. The scanning electron microscope. *Zeitschrift Fur Physik*, 109(9-10):553–572, September 1938.
- [52] Ludwig Reimer. *Scanning Electron Microscopy*, volume 45 of *Springer Series in Optical Sciences*. Springer, 2nd edition, 1998.
- [53] G. Binnig, H. Rohrer, C. Gerber, and E. Weibel. Tunneling through a controllable vacuum gap. *Applied Physics Letters*, 40(2):178–180, 1982.
- [54] G. Binnig, H. Rohrer, Ch. Gerber, and E. Weibel. Surface studies by scanning tunneling microscopy. *Phys. Rev. Lett.*, 49(1):57–61, jul 1982.
- [55] G. Binnig and H. Rohrer. Scanning tunneling microscopy. *Surface Science*, 126(1-3):236–244, 1983.
- [56] G. Binnig, C. F. Quate, and C. Gerber. Atomic force microscope. *Physical Review Letters*, 56(9):930–933, March 1986.
- [57] E.H. Synge. Xxxviii. a suggested method for extending microscopic resolution into the ultra-microscopic region. *Philosophical Magazine Series 7*, 6(35):356–362, 1928.
- [58] E. A. Ash and G. Nicholls. Super-resolution aperture scanning microscope. *Nature*, 237(5357):510–&, 1972.
- [59] D. W. Pohl, W. Denk, and M. Lanz. Optical stethoscopy - image recording with resolution  $\lambda/20$ . *Applied Physics Letters*, 44(7):651–653, 1984.
- [60] A. Lewis, M. Isaacson, A. Harootunian, and A. Muray. Development of a 500- $\mu\text{m}$  spatial-resolution light-microscope .1. light is efficiently transmitted through gamma-16 diameter apertures. *Ultramicroscopy*, 13(3):227–231, 1984.
- [61] E. BETZIG, J. K. TRAUTMAN, T. D. HARRIS, J. S. WEINER, and R. L. KOSTELAK. Breaking the diffraction barrier: Optical microscopy on a nanometric scale. *Science*, 251(5000):1468–1470, 1991.

- [62] D. V. Palanker, D. M. Simanovskii, P. Huie, and T. I. Smith. On contrast parameters and topographic artifacts in near-field infrared microscopy. *Journal of Applied Physics*, 88(11):6808–6814, 2000.
- [63] J. Wessel. Surface-enhanced optical microscopy. *Journal of the Optical Society of America B-optical Physics*, 2(9):1538–1541, 1985.
- [64] H.K. Wickramasinghe and C.C. Williams. Apertureless near-field optical microscope, 1990.
- [65] F. Zenhausern, M. P. Oboyle, and H. K. Wickramasinghe. Apertureless near-field optical microscope. *Applied Physics Letters*, 65(13):1623–1625, September 1994.
- [66] M. Brehm, A. Schliesser, F. Cajko, I. Tsukerman, and F. Keilmann. Antenna-mediated back-scattering efficiency in infrared near-field microscopy. *Optics Express*, 16(15):11203–11215, July 2008.
- [67] R. Hillenbrand, B. Knoll, and F. Keilmann. Pure optical contrast in scattering-type scanning near-field microscopy. *Journal of Microscopy-oxford*, 202:77–83, April 2001.
- [68] M. Labardi, S. Patane, and M. Allegrini. Artifact-free near-field optical imaging by apertureless microscopy. *Applied Physics Letters*, 77(5):621–623, July 2000.
- [69] N. Ocelic, A. Huber, and R. Hillenbrand. Pseudoheterodyne detection for background-free near-field spectroscopy. *Applied Physics Letters*, 89(10):101124, September 2006.
- [70] L. Novotny and B. Hecht. *Principles of Nano Optics*. Cambridge University Press, 2006.
- [71] T. Taubner, R. Hillenbrand, and F. Keilmann. Performance of visible and mid-infrared scattering-type near-field optical microscopes. *Journal of Microscopy-oxford*, 210:311–314, June 2003.
- [72] Johannes M. Stiegler, Yohannes Abate, Antonija Cvitkovic, Yaroslav E. Romanuk, Andreas J. Huber, Stephen R. Leone, and Rainer Hillenbrand. Nanoscale infrared absorption spectroscopy of individual nanoparticles enabled by scattering-type near-field microscopy. *ACS Nano*, 5(8):6494–6499, 2011.
- [73] J. M. Stiegler, A. J. Huber, S. L. Diedenhofen, J. Gomez Rivas, R. E. Algra, E. P. A. M. Bakkers, and R. Hillenbrand. Nanoscale free-carrier profiling of individual semiconductor nanowires by infrared near-field nanoscopy. *Nano Letters*, 10(4):1387–1392, April 2010.

- [74] J.M. Stiegler, R. Tena-Zaera, O. Idigoras, A. Chuvilin, and R. Hillenbrand. Correlative infrared-electron nanoscopy reveals the local structure-conductivity relationship in zinc oxide nanowires. *Nat Commun*, 3:1131–, October 2012.
- [75] S. C. Kehr, M. Cebula, O. Mieth, T. Haertling, J. Seidel, S. Grafstroem, L. M. Eng, S. Winnerl, D. Stehr, and M. Helm. Anisotropy contrast in phonon-enhanced apertureless near-field microscopy using a free-electron laser. *Physical Review Letters*, 100(25):256403, June 2008.
- [76] A. J. Huber, A. Ziegler, T. Koeck, and R. Hillenbrand. Infrared nanoscopy of strained semiconductors. *Nature Nanotechnology*, 4(3):153–157, March 2009.
- [77] B. B. Akhremitchev, Y. J. Sun, L. Stebounova, and G. C. Walker. Monolayer-sensitive infrared imaging of dna stripes using apertureless near-field microscopy. *Langmuir*, 18(14):UNSP LA025700R, July 2002.
- [78] A. Cvitkovic, N. Ocelic, and R. Hillenbrand. Material-specific infrared recognition of single sub-10 nm particles by substrate-enhanced scattering-type near-field microscopy. *Nano Letters*, 7(10):3177–3181, October 2007.
- [79] G. Wollny, E. Bruendermann, Z. Arsov, L. Quaroni, and M. Havenith. Nanoscale depth resolution in scanning near-field infrared microscopy. *Optics Express*, 16(10):7453–7459, May 2008.
- [80] Y. Ogawa, F. Minami, Y. Abate, and S. R. Leone. Nanometer-scale dielectric constant of ge quantum dots using apertureless near-field scanning optical microscopy. *Applied Physics Letters*, 96(6):063107, February 2010.
- [81] Nenad Ocelic. *Quantitative near-field phonon-polariton spectroscopy*. PhD thesis, Technische Universität München, 2007.
- [82] Andreas Huber. *Nanoscale surface-polariton spectroscopy by mid- and far-infrared near-field microscopy*. PhD thesis, Technische Universität München, 2010.
- [83] R. M. Stockle, Y. D. Suh, V. Deckert, and R. Zenobi. Nanoscale chemical analysis by tip-enhanced raman spectroscopy. *Chemical Physics Letters*, 318(1-3):131–136, February 2000.
- [84] M. S. Anderson. Locally enhanced raman spectroscopy with an atomic force microscope. *Applied Physics Letters*, 76(21):PII [S0003–6951(00)00721–X], May 2000.
- [85] N. Hayazawa, Y. Inouye, Z. Sekkat, and S. Kawata. Near-field raman scattering enhanced by a metallized tip. *Chemical Physics Letters*, 335(5-6):369–374, March 2001.

- [86] A. Hartschuh, E. J. Sanchez, X. S. Xie, and L. Novotny. High-resolution near-field raman microscopy of single-walled carbon nanotubes. *Physical Review Letters*, 90(9):095503, March 2003.
- [87] Rainer Hillenbrand. *Nahfeldoptische Amplituden- und Phasenkontrastmikroskopie zur optischen Abbildung von Materialkontrast und optisch resonanten Partikeln*. PhD thesis, Technische Universität München, 2001.
- [88] A. Cvitkovic. *Substrate-enhanced scattering-type scanning near-field infrared microscopy of nanoparticles*. PhD thesis, Technische Universität München, 2009.
- [89] R. Hillenbrand and F. Keilmann. Complex optical constants on a subwavelength scale. *Physical Review Letters*, 85(14):3029–3032, October 2000.
- [90] J. D. Jackson. *Classical Electrodynamics Third Edition*. Wiley, New York, 3rd edition, 1999.
- [91] A. Huber, N. Ocelic, T. Taubner, and R. Hillenbrand. Nanoscale resolved infrared probing of crystal structure and of plasmon-phonon coupling. *Nano Letters*, 6(4):774–778, April 2006.
- [92] A. Cvitkovic, N. Ocelic, and R. Hillenbrand. Analytical model for quantitative prediction of material contrasts in scattering-type near-field optical microscopy. *Optics Express*, 15(14):8550–8565, July 2007.
- [93] S. Amarie and F. Keilmann. Broadband-infrared assessment of phonon resonance in scattering-type near-field microscopy. *Phys. Rev. B*, 83:045404, Jan 2011.
- [94] M. T. Bjork, B. J. Ohlsson, T. Sass, A. I. Persson, C. Thelander, M. H. Magnusson, K. Deppert, L. R. Wallenberg, and L. Samuelson. One-dimensional steeplechase for electrons realized. *Nano Letters*, 2(2):87–89, February 2002.
- [95] M. H. M. van Weert, A. Helman, W. van den Einden, R. E. Algra, M. A. Verheijen, M. T. Borgstrom, G. Immink, J. J. Kelly, L. P. Kouwenhoven, and E. P. A. M. Bakkers. Zinc incorporation via the vapor-liquid-solid mechanism into inp nanowires. *Journal of the American Chemical Society*, 131(13):4578–+, April 2009.
- [96] J. A. Van Dam, Y. V. Nazarov, E. P. A. M. Bakkers, S. De Franceschi, and L. P. Kouwenhoven. Supercurrent reversal in quantum dots. *Nature*, 442(7103):667–670, August 2006.

- [97] S. J. Pearton, D. P. Norton, and F. Ren. The promise and perils of wide-bandgap semiconductor nanowires for sensing, electronic, and photonic applications. *Small*, 3(7):1144–1150, July 2007.
- [98] E. C. Garnett, Y.-C. Tseng, D. R. Khanal, J. Wu, J. Bokor, and P. Yang. Dopant profiling and surface analysis of silicon nanowires using capacitance-voltage measurements. *Nature Nanotechnology*, 4(5):311–314, May 2009.
- [99] M. Fox, editor. *Optical Properties of Solids*. Oxford University Press, 2005.
- [100] M. Grundmann, editor. *The Physics of Semiconductors*. Springer, 2006.
- [101] K. Kopitzki. *Einführung in die Festkörperphysik*. Teubner Studienbücher, 1993.
- [102] H. Kuzmany. *Solid-State Spectroscopy*. Springer, 1998.
- [103] C. Klingshirn. *Semiconductor Optics*. Springer, 2005.
- [104] M. Sotoodeh, A. H. Khalid, and A. A. Rezazadeh. Empirical low-field mobility model for iii-v compounds applicable in device simulation codes. *Journal of Applied Physics*, 87(6):2890–2900, March 2000.
- [105] J. Ibanez, R. Cusco, and L. Artus. Raman scattering determination of free charge density using a modified hydrodynamical model. *Physica Status Solidi B-basic Research*, 223(3):715–722, 2001.
- [106] P.Y. Yu and M. Cardona. *Fundamentals of Semiconductors*. Springer, 2003.
- [107] Xiangfeng Duan, Yu Huang, Yi Cui, Jianfang Wang, and Charles M. Lieber. Indium phosphide nanowires as building blocks for nanoscale electronic and optoelectronic devices. *Nature*, 409(6816):66–69, January 2001.
- [108] R. S. Wagner and W. C. Ellis. Vapor-liquid-solid mechanism of single crystal growth ( new method growth catalysis from impurity whisker epitaxial + large crystals si e ). *Applied Physics Letters*, 4(5):89–91, 1964.
- [109] X. F. Duan and C. M. Lieber. General synthesis of compound semiconductor nanowires. *Advanced Materials*, 12(4):298–302, 2000.
- [110] J. B. Hannon, S. Kodambaka, F. M. Ross, and R. M. Tromp. The influence of the surface migration of gold on the growth of silicon nanowires. *Nature*, 440(7080):69–71, March 2006.
- [111] E. I. Givargizov. Fundamental aspects of vls growth. *Journal of Crystal Growth*, 31(DEC):20–30, 1975.

- [112] R. E. Algra, M. A. Verheijen, M. T. Borgstrom, L.-F. Feiner, G. Immink, W. J. P. van Enckevort, E. Vlieg, and E. P. A. M. Bakkers. Twinning superlattices in indium phosphide nanowires. *Nature*, 456(7220):369–372, November 2008.
- [113] J. Johansson, L. S. Karlsson, C. P. T. Svensson, T. Martensson, B. A. Wacaser, K. Deppert, L. Samuelson, and W. Seifert. Structural properties of (111)b-oriented iii-v nanowires. *Nature Materials*, 5(7):574–580, July 2006.
- [114] M. T. Borgstrom, G. Immink, B. Ketelaars, R. Algra, and E. P. A. M. Bakkers. Synergetic nanowire growth. *Nature Nanotechnology*, 2(9):541–544, September 2007.
- [115] K. Hiruma, M. Yazawa, T. Katsuyama, K. Ogawa, K. Haraguchi, M. Koguchi, and H. Kakibayashi. Growth and optical properties of nanometer-scale gaas and inas whiskers. *Journal of Applied Physics*, 77(2):447–462, 1995.
- [116] Frank Glas, Jean-Christophe Harmand, and Gilles Patriarche. Why does wurtzite form in nanowires of iii-v zinc blende semiconductors? *Physical Review Letters*, 99(14):146101, October 2007.
- [117] X. F. Duan and C. M. Lieber. Laser-assisted catalytic growth of single crystal gan nanowires. *Journal of the American Chemical Society*, 122(1):188–189, January 2000.
- [118] Anna Cavallini, Laura Polenta, Marco Rossi, Thomas Richter, Michel Marso, Ralph Meijers, Raffaella Calarco, and Hans Lueth. Defect distribution along single gan nanowhiskers. *Nano Letters*, 6(7):1548–1551, July 2006.
- [119] Lambert K. van Vugt, Sven Ruhle, and Daniel Vanmaekelbergh. Phase-correlated nondirectional laser emission from the end facets of a zno nanowire. *Nano Letters*, 6(12):2707–2711, December 2006.
- [120] S. L. Diedenhofen. *Propagation of Light in Ensembles of Semiconductor Nanowires*. PhD thesis, Technische Universiteit Eindhoven, 2010.
- [121] L. J. Lauhon, M. S. Gudiksen, C. L. Wang, and C. M. Lieber. Epitaxial core-shell and core-multishell nanowire heterostructures. *Nature*, 420(6911):57–61, November 2002.
- [122] N. Skold, L. S. Karlsson, M. W. Larsson, M. E. Pistol, W. Seifert, J. Tragardh, and L. Samuelson. Growth and optical properties of strained gaas-gaxin<sub>1-xp</sub> core-shell nanowires. *Nano Letters*, 5(10):1943–1947, October 2005.
- [123] H. . Y. Li, O. Wunnicke, M. T. Borgstrom, W. G. G. Immink, M. H. M. van Weert, M. A. Verheijen, and E. P. A. M. Bakkers. Remote p-doping of inas nanowires. *Nano Letters*, 7(5):1144–1148, May 2007.

- [124] M. A. Verheijen, G. Immink, T. de Smet, M. T. Borgstrom, and E. P. A. M. Bakkers. Growth kinetics of heterostructured gap-gaas nanowires. *Journal of the American Chemical Society*, 128(4):1353–1359, February 2006.
- [125] T. I. Jeon and D. Grischkowsky. Nature of conduction in doped silicon. *Physical Review Letters*, 78(6):1106–1109, February 1997.
- [126] P. S. Carney and J. C. Schotland. Inverse scattering for near-field microscopy. *Applied Physics Letters*, 77(18):2798–2800, October 2000.
- [127] J. Sun, J. C. Schotland, R. Hillenbrand, and P. S. Carney. Nanoscale optical tomography using volume-scanning near-field microscopy. *Applied Physics Letters*, 95(12):121108, September 2009.
- [128] J. Aizpurua, T. Taubner, F. J. Garcia de Abajo, M. Brehm, and R. Hillenbrand. Substrate-enhanced infrared near-field spectroscopy. *Optics Express*, 16(3):1529–1545, February 2008.
- [129] P. Caroff, K. A. Dick, J. Johansson, M. E. Messing, K. Deppert, and L. Samuelson. Controlled polytypic and twin-plane superlattices in iii-v nanowires. *Nature Nanotechnology*, 4(1):50–55, January 2009.
- [130] S. Amarie, T. Ganz, and F. Keilmann. Mid-infrared near-field spectroscopy. *Optics Express*, 17(24):21794–21801, November 2009.
- [131] T. Taubner, F. Keilmann, and R. Hillenbrand. Nanoscale-resolved subsurface imaging by scattering-type near-field optical microscopy. *Optics Express*, 13(22):8893–8899, October 2005.
- [132] D. Spirkoska, J. Arbiol, A. Gustafsson, S. Conesa-Boj, F. Glas, I. Zardo, M. Heigoldt, M. H. Gass, A. L. Bleloch, S. Estrade, M. Kaniber, J. Rossler, F. Peiro, J. R. Morante, G. Abstreiter, L. Samuelson, and A. Fontcuberta i Morral. Structural and optical properties of high quality zinc-blende/wurtzite gaas nanowire heterostructures. *Physical Review B*, 80(24):245325, December 2009.
- [133] F. J. Lopez, E. R. Hemesath, and L. J. Lauhon. Ordered stacking fault arrays in silicon nanowires. *Nano Letters*, 9(7):2774–2779, July 2009.
- [134] J. Todorovic, A. F. Moses, T. Karlberg, P. Olk, D. L. Dheeraj, B. O. Fimland, H. Weman, and A. T. J. van Helvoort. Correlated micro-photoluminescence and electron microscopy studies of the same individual heterostructured semiconductor nanowires. *Nanotechnology*, 22(32):325707, August 2011.

- [135] S. K. Lim, M. Brewster, F. Qian, Y. Li, C. M. Lieber, and S. Gradecak. Direct correlation between structural and optical properties of iii-v nitride nanowire heterostructures with nanoscale resolution. *Nano Letters*, 9(11):3940–3944, November 2009.
- [136] Martin Heiss, Sonia Conesa-Boj, Jun Ren, Hsiang-Han Tseng, Adam Gali, Andreas Rudolph, Emanuele Uccelli, Francesca Peiro, Joan Ramon Morante, Dieter Schuh, Elisabeth Reiger, Efthimios Kaxiras, Jordi Arbiol, and Anna Fontcuberta i Morral. Direct correlation of crystal structure and optical properties in wurtzite/zinc-blende gaas nanowire heterostructures. *Physical Review B*, 83(4):045303, January 2011.
- [137] M. D. Schroer and J. R. Petta. Correlating the nanostructure and electronic properties of inas nanowires. *Nano Letters*, 10(5):1618–1622, May 2010.
- [138] Claes Thelander, Philippe Caroff, Sebastien Plissard, Anil W. Dey, and Kimberly A. Dick. Effects of crystal phase mixing on the electrical properties of inas nanowires. *Nano Letters*, 11(6):2424–2429, June 2011.
- [139] A. Sartori, R. Gatz, F. Beck, A. Rigort, W. Baumeister, and J. M. Plitzko. Correlative microscopy: Bridging the gap between fluorescence light microscopy and cryo-electron tomography. *Journal of Structural Biology*, 160(2):135–145, November 2007.
- [140] R. S. Polishchuk, E. V. Polishchuk, P. Marra, S. Alberti, R. Buccione, A. Luini, and A. A. Mironov. Correlative light-electron microscopy reveals the tabular-saccular ultrastructure of carriers operating between golgi apparatus and plasma membrane. *Journal of Cell Biology*, 148(1):45–58, January 2000.
- [141] R. Konenkamp, R. C. Word, and M. Godinez. Ultraviolet electroluminescence from zno/polymer heterojunction light-emitting diodes. *Nano Letters*, 5(10):2005–2008, October 2005.
- [142] S. Xu, Y. Qin, C. Xu, Y. Wei, R. Yang, and Z. L. Wang. Self-powered nanowire devices. *Nature Nanotechnology*, 5(5):366–373, May 2010.
- [143] J. Xu, X. Yang, H. Wang, X. Chen, C. Luan, Z. Xu, Z. Lu, V. A. L. Roy, W. Zhang, and C.-S. Lee. Arrays of zno/zn(x)cd(1-x)se nanocables: Band gap engineering and photovoltaic applications. *Nano Letters*, 11(10):4138–4143, October 2011.
- [144] L. Vayssieres. Growth of arrayed nanorods and nanowires of zno from aqueous solutions. *Advanced Materials*, 15(5):464–466, March 2003.

- [145] J. Joo, B. Y. Chow, M. Prakash, E. S. Boyden, and J. M. Jacobson. Face-selective electrostatic control of hydrothermal zinc oxide nanowire synthesis. *Nature Materials*, 10(8):596–601, August 2011.
- [146] S. Peulon and D. Lincot. Cathodic electrodeposition from aqueous solution of dense or open-structured zinc oxide films. *Advanced Materials*, 8(2):166–170, February 1996.
- [147] R. Tena-Zaera, J. Elias, G. Wang, and C. Levy-Clement. Role of chloride ions on electrochemical deposition of zno nanowire arrays from o-2 reduction. *Journal of Physical Chemistry C*, 111(45):16706–16711, November 2007.
- [148] J. Elias, R. Tena-Zaera, and C. LÃ’vy-ClÃ’ment. Electrochemical deposition of zno nanowire arrays with tailored dimensions. *Journal of Electroanalytical Chemistry*, 621(2):171 – 177, 2008. <ce:title>Special Issue in Honor of Professor Israel Rubinstein</ce:title>.
- [149] R. Tena-Zaera, J. Elias, C. Levy-Clement, I. Mora-Sero, Y. Luo, and J. Bisquert. Electrodeposition and impedance spectroscopy characterization of zno nanowire arrays. *Physica Status Solidi A-applications and Materials Science*, 205(10):European Mat Res Soc, October 2008.
- [150] S. Peulon and D. Lincot. Mechanistic study of cathodic electrodeposition of zinc oxide and zinc hydroxychloride films from oxygenated aqueous zinc chloride solutions. *Journal of the Electrochemical Society*, 145(3):864–874, March 1998.
- [151] Q. Zhang, H. Guo, Z. Feng, L. Lin, J. Zhou, and Z. Lin. n-zno nanorods/p-cuscn heterojunction light-emitting diodes fabricated by electrochemical method. *Electrochimica Acta*, 55(17):4889–4894, July 2010.
- [152] Brian O’Regan, Frank Lenzmann, Ruud Muis, and Jeannette Wienke. A solid-state dye-sensitized solar cell fabricated with pressure-treated p25-tio<sub>2</sub> and cuscn: Analysis of pore filling and iv characteristics. *Chemistry of Materials*, 14(12):5023–5029, 2002.
- [153] M. Brehm, T. Taubner, R. Hillenbrand, and F. Keilmann. Infrared spectroscopic mapping of single nanoparticles and viruses at nanoscale resolution. *Nano Letters*, 6(7):1307–1310, July 2006.
- [154] T. Itoh, K. Matsuyama, K. Shimakawa, J. Orava, T. Wagner, and M. Frumar. Optical properties of conductive zno films near infrared frequency. *Physica Status Solidi C: Current Topics In Solid State Physics, Vol 6, Suppl 1*, 6:S110–S113, 2009.

- [155] R. Tena-Zaera, J. Elias, C. Levy-Clement, C. Bekeny, T. Voss, I. Mora-Sero, and J. Bisquert. Influence of the potassium chloride concentration on the physical properties of electrodeposited zno nanowire arrays. *Journal of Physical Chemistry C*, 112(42):16318–16323, October 2008.
- [156] J. J. Richardson, G. K. L. Goh, H. Q. Le, L.-L. Liew, F. F. Lange, and S. P. Den-Baars. Thermally induced pore formation in epitaxial zno films grown from low temperature aqueous solution. *Crystal Growth & Design*, 11(8):3558–3563, August 2011.
- [157] L. Vayssieres, K. Keis, A. Hagfeldt, and S. E. Lindquist. Three-dimensional array of highly oriented crystalline zno microtubes. *Chemistry of Materials*, 13(12):4395–4398, December 2001.
- [158] J. Elias, R. Tena-Zaera, G.-Y. Wang, and C. Levy-Clement. Conversion of zno nanowires into nanotubes with tailored dimensions. *Chemistry of Materials*, 20(21):6633–6637, November 2008.
- [159] G.-W. She, X.-H. Zhang, W.-S. Shi, X. Fan, J. C. Chang, C.-S. Lee, S.-T. Lee, and C.-H. Liu. Controlled synthesis of oriented single-crystal zno nanotube arrays on transparent conductive substrates. *Applied Physics Letters*, 92(5):053111, February 2008.
- [160] Ivan Mora-Sero, Francisco Fabregat-Santiago, Benjamin Denier, Juan Bisquert, Ramon Tena-Zaera, Jamil Elias, and Claude Levy-Clement. Determination of carrier density of zno nanowires by electrochemical techniques. *Applied Physics Letters*, 89(20):203117, November 2006.
- [161] Roman Krutokhvostov, Alexander A. Govyadinov, Johannes M. Stiegler, Florian Huth, Andrey Chuvilin, P. Scott Carney, and Rainer Hillenbrand. Enhanced resolution in subsurface near-field optical microscopy. *Optics Express*, 20(1):593–600, January 2012.
- [162] C. C. Neacsu, J. Dreyer, N. Behr, and M. B. Raschke. Scanning-probe raman spectroscopy with single-molecule sensitivity. *Physical Review B*, 73(19):193406, May 2006.
- [163] B. Pettinger, B. Ren, G. Picardi, R. Schuster, and G. Ertl. Nanoscale probing of adsorbed species by tip-enhanced raman spectroscopy. *Physical Review Letters*, 92(9):096101, March 2004.

- [164] T. Deckert-Gaudig, E. Bailo, and V. Deckert. Tip-enhanced raman scattering (TERS) of oxidised glutathione on an ultraflat gold nanoplate. *Physical Chemistry Chemical Physics*, 11(34):7360–7362, 2009.
- [165] M. Paulite, Z. Fakhraai, I. T. S. Li, N. Gunari, A. E. Tanur, and G. C. Walker. Imaging secondary structure of individual amyloid fibrils of a beta(2)-microglobulin fragment using near-field infrared spectroscopy. *Journal of the American Chemical Society*, 133(19):7376–7383, May 2011.
- [166] G. N. Parsons, J. H. Souk, and J. Batey. Low hydrogen content stoichiometric silicon-nitride films deposited by plasma-enhanced chemical vapor-deposition. *Journal of Applied Physics*, 70(3):1553–1560, August 1991.
- [167] V. Palermo and D. Jones. Self-organised growth of silicon structures on silicon during oxide desorption. *Materials Science and Engineering B-solid State Materials For Advanced Technology*, 88(2-3):European Mat Res Soc, January 2002.
- [168] Z. H. Kim, S.-H. Ahn, B. Liu, and S. R. Leone. Nanometer-scale dielectric imaging of semiconductor nanoparticles: Size-dependent dipolar coupling and contrast reversal. *Nano Letters*, 7(8):2258–2262, August 2007.
- [169] R. Brendel and D. Bormann. An infrared dielectric function model for amorphous solids. *Journal of Applied Physics*, 71(1):1–6, January 1992.
- [170] C. F. Bohren and D. R. Huffman. *Absorption and Scattering of Light by Small Particles*. Wiley-VCH, 1998.
- [171] A. Weber-Bargioni, A. Schwartzberg, M. Cornaglia, A. Ismach, J. J. Urban, Y. J. Pang, R. Gordon, J. Bokor, M. B. Salmeron, D. F. Ogletree, P. Ashby, S. Cabrini, and P. J. Schuck. Hyperspectral nanoscale imaging on dielectric substrates with coaxial optical antenna scan probes. *Nano Letters*, 11(3):1201–1207, March 2011.
- [172] Y. Zou, P. Steinvurzel, T. Yang, and K. B. Crozier. Surface plasmon resonances of optical antenna atomic force microscope tips. *Applied Physics Letters*, 94(17):171107, April 2009.
- [173] F. De Angelis, G. Das, P. Candeloro, M. Patrini, M. Galli, A. Bek, M. Lazzarino, I. Maksymov, C. Liberale, L. C. Andreani, and E. Di Fabrizio. Nanoscale chemical mapping using three-dimensional adiabatic compression of surface plasmon polaritons. *Nature Nanotechnology*, 5(1):67–72, January 2010.